

Structure-Activity-Stability and In-Situ Raman Spectroscopic Studies of Oxygen Evolution Catalysts in Acidic Environment

vorgelegt von
Diplom-Ingenieur Tobias Reier
geb. in Berlin

von der Fakultät II - Mathematik und Naturwissenschaften
der Technischen Universität Berlin
zur Erlangung des akademischen Grades

Doktor der Ingenieurwissenschaften
Dr.-Ing.

genehmigte Dissertation

Promotionsausschuss:

Vorsitzender: Prof. Dr. Michael Gradzielski (TU Berlin)
Gutachter: Prof. Dr. Peter Strasser (TU Berlin)
Gutachterin: Prof. Dr. Christina Roth (FU Berlin)

Tag der wissenschaftlichen Aussprache: 05.11.2015

Berlin 2016

Danksagung

An dieser Stelle möchte ich all jenen danken, die durch ihr Handeln die Entstehung der vorliegenden Arbeit ermöglicht haben. Für ihre Geduld und ihre Unterstützung innerhalb und außerhalb der wissenschaftlichen Arbeit sowie für das Korrekturlesen dieser Dissertation möchte ich mich bei Hong Nhan Nong (*Su tu ngot*) ganz herzlich bedanken.

Mein besonderer Dank gilt Herrn Professor Peter Strasser für die Bereitstellung des interessanten Themas, die stets vorhandene Unterstützung in allen wissenschaftlichen Fragen und die Betreuung dieser Arbeit. Die eingeräumten Freiheiten in der täglichen wissenschaftlichen Arbeit und die lebhaften wissenschaftlichen Diskussionen haben wesentlich zur Entstehung dieser Arbeit beigetragen.

Frau Professor Christina Roth danke ich für die Bereitschaft als zweite Gutachterin dieser Arbeit zu fungieren und Herrn Professor Michael Gradzielski möchte für die Übernahme des Vorsitzes des Promotionsausschusses danken.

Frau Professor Inez Weidinger und Herrn Professor Peter Hildebrandt möchte ich für die umfassende Kooperation auf dem Gebiet der Ramanspektroskopie danken. Neben der Bereitstellung von Messzeit an ihren Ramanspektrometern führte die wissenschaftliche Diskussion mit ihnen immer wieder zu neuen Denkanstößen. Herrn Dr. Uwe Kuhlmann möchte ich in diesem Zusammenhang für die Einstellung und Kalibrierung des Ramanspektrometers danken.

Mein besonderer Dank gilt Frau Zarina Pawolek und Herrn Camillo Spöri, die im Rahmen ihrer Bachelorarbeiten und Praktika einen Teil zum Fortschritt meiner wissenschaftlichen Arbeit beigetragen haben und zusammen mit mir wissenschaftliche Fragestellungen mit viel Fleiß, Ausdauer und Sachverstand bearbeitet haben. Herrn Camillo Spöri danke ich außerdem für das Korrekturlesen dieser Arbeit.

Herrn Dr. Detre Teschner und Herrn Dr. Michael Bruns danke ich für die Kooperation auf dem Gebiet der Röntgenphotoelektronenspektroskopie. Herrn Arno Bergmann möchte ich für zahlreiche wissenschaftliche Diskussionen und seine immer vorhandene Hilfsbereitschaft danken. Für die Durchführung von TEM/STEM Messungen und die dazugehörige Probenpräparation danke ich Herrn Dr. Thomas Lunkenbein, Herrn Sören Selve sowie Herrn Jan Simke. Bei Frau Beatrice Kranzusch möchte ich mich für die Präparation der Titanschichten auf Si-Wafern bedanken. Herrn Dr. Serhiy Cherevko und Herrn Professor Karl Mayrhofer gilt mein Dank für die enge Kooperation auf dem Gebiet der Korrosionsmessungen mittels ICP-MS und den fundierten wissenschaftlichen Diskussionen. Herrn Dr. Ralph Krähnert möchte ich für den Zugang zu seinem SEM danken. Bei Herrn Benjamin Paul bedanke ich mich für die vielseitige Unterstützung in technischen Fragen. Herrn Dr. Benjamin Beck danke ich für die Durchführung der TG-MS Messungen. Bei Astrid Müller-Klauke möchte ich mich für die Durchführung der ICP-OES Messungen bedanken.

Darüber hinaus möchte ich mich bei allen anderen Mitgliedern des Arbeitskreises von Professor Peter Strasser sowie den Mitarbeitern der Werkstatt und dem Glasbläser für ihre Unterstützung bedanken.

Abstract

Water electrolysis emerges as key technology for the long-term storage of electricity from renewable sources which is essential to overcome their intermittent availability. In this context, proton exchange membrane (PEM) electrolyzers constitute the most promising technology. Considering PEM electrolyzers, the main catalytic efficiency losses (overpotentials) and stability problems are related to the noble metal based anode catalyst, where the oxygen evolution reaction (OER) proceeds.

This work aims to establish a more profound understanding of the electrocatalytic OER and the related catalysts under acidic conditions to facilitate the knowledge based improvement of the catalyst's activity and stability and, additionally, to lower its noble metal content. Initially, an appropriate model catalyst for the fundamental investigation of PEM-OER catalysts was contrived, which allows for microkinetic studies and the investigation of catalyst-substrate interactions. In this context, thermally prepared thin homogenous oxide films were found to constitute an adequate model system. Based on this model system, first Ir oxide was studied. Thereby, two chemically distinct Ir oxides with distinctly different catalytic properties were identified as a function of calcination temperature. The amorphous low temperature Ir oxide provided a considerably higher OER activity but, unfortunately, a lower Ir stability than the crystalline Ir oxide formed at higher calcination temperatures. Catalyst-substrate interactions between the Ir oxide layer and the Ti substrate were solely identified at the highest investigated calcination temperature of 550°C and decreased the OER activity of the catalyst. Although indications for the OER activity and stability determining material properties were obtained in the study of pure Ir oxides, a more detailed investigation of this aspect was performed based on Ir-Ni mixed oxides. Considering Ir-Ni mixed oxides, the OER activity and the Ir stability can be varied continuously, which allows the identification of the material properties relevant for the OER activity and stability as well as their optimization. Based on Ir-Ni mixed oxides the Ir mass based OER activity could be increased by a factor of ~20 compared to a similarly prepared pure Ir oxide reference sample. Furthermore, this study revealed that the oxide surface termination critically determines the OER activity of Ir-Ni oxides. Hereby, the fraction of surface hydroxyl groups was found to be correlated to the surface specific OER activity of the oxide.

The surface processes occurring during the OER were studied by in-situ surface enhanced Raman spectroscopy (SERS) on a Ru oxide catalyst. In order to provide the required surface enhancement a recent approach called shell-isolated nanoparticle-enhanced Raman spectroscopy was adapted to PEM-OER catalysts and its applicability for SERS studies of OER catalysts was demonstrated. In this study an OH_x species was identified which appeared exclusively during the OER.

Zusammenfassung

Die Wasserelektrolyse stellt eine Schlüsseltechnologie für die Speicherung von überschüssiger Elektrizität aus erneuerbaren Quellen dar. Protonen Austausch Membran (engl.: proton exchange membrane - PEM) Elektrolyseure sind die vielversprechendste Technologie in diesem Zusammenhang. Im Bereich der PEM Elektrolyseure sind die größten katalytischen Effizienzeinbußen und Stabilitätsprobleme mit dem edelmetallbasierten Anodenkatalysator verbunden, an dem die elektrokatalytische Sauerstoffevolutionsreaktion (engl.: oxygen evolution reaction - OER) abläuft.

Ziel dieser Arbeit ist ein tiefer gehendes Verständnis der elektrokatalytischen OER und des dafür eingesetzten Katalysators im stark sauren Milieu zu entwickeln, um die Aktivität und Stabilität des Katalysators gezielt zu steigern und den Edelmetallgehalt zu senken. Als Modellkatalysator für diese Untersuchung wurden dünne thermisch synthetisierte Oxidfilme ausgewählt, die sich hervorragend für mikrokinetische Studien und die Untersuchung von Katalysator-Substrat-Wechselwirkungen eignen. Auf Grundlage dieses Modellsystems wurde zunächst reines Iridiumoxid untersucht. Dabei wurden zwei chemisch unterschiedliche Iridiumoxide in Abhängigkeit von der Kalzinierungstemperatur nachgewiesen. Das bei niedrigen Kalzinierungstemperaturen entstandene amorphe Iridiumoxid zeigte eine größere Aktivität aber eine geringere Stabilität in der OER als das kristalline Iridiumoxid, das bei höheren Kalzinierungstemperaturen entstand. Katalysator-Substrat-Wechselwirkungen zwischen Iridiumoxid und Titansubstrat konnten ausschließlich bei der höchsten Kalzinierungstemperatur von 550°C festgestellt werden und verringerten die OER-Aktivität des Katalysators. Obschon die Untersuchung von reinem Iridiumoxid Hinweise auf die aktivitäts- und stabilitätsbestimmenden Materialeigenschaften lieferte, wurden diese auf Basis von Iridium-Nickel-Mischoxiden genauer untersucht. Iridium-Nickel-Mischoxide erlauben eine kontinuierliche Variation der OER-Aktivität und Iridium-Stabilität, und somit deren Optimierung, durch Änderung des Ir:Ni Verhältnisses. Durch gleichzeitige umfassende Charakterisierung der Materialeigenschaften des Mischoxids konnten die für die OER-Aktivität und Iridium-Stabilität maßgeblichen Materialeigenschaften identifiziert werden. Die OER-Aktivität wurde dabei maßgeblich von der Oberflächenterminierung des Oxids bestimmt. Durch Optimierung des Ir:Ni Verhältnisses konnte die auf die Iridium Masse normierte OER-Aktivität um den Faktor 20 gesteigert werden.

Die Oberflächenprozesse während der OER wurden in-situ mittels oberflächenverstärkter Ramanspektroskopie auf einem Rutheniumoxidkatalysator untersucht. Um die benötigte Oberflächenverstärkung bereitzustellen wurde eine neue Technik namens shell-isolated nanoparticle-enhanced Raman spectroscopy angewendet und deren Einsetzbarkeit für OER-Untersuchungen demonstriert. Im Rahmen der ramanspektroskopischen Untersuchung wurde eine OH_x Spezies identifiziert, die ausschließlich während der OER zu beobachten war.

Table of Contents

1	Introduction	1
1.1	Proton exchange membrane (PEM) based water electrolysis- the technology of choice for storage of renewable electricity	1
1.2	PEM OER catalysts - brief review and current status	4
1.3	Basic considerations about water splitting with emphasis on the oxygen evolution reaction (OER)	8
1.4	Mechanism of the OER	10
1.5	Origin of catalytic overpotentials in the OER	12
1.6	Motivation	17
2	Experimental part	19
2.1	Preparation of thin oxide films	19
2.2	Preparation of silica coated gold nanoparticles and their deposition on the Ru oxide model film	23
2.3	Physicochemical characterization	25
2.4	Electrochemistry and related in-situ methods	28
3	Choice of model catalyst and catalyst synthesis development	33
3.1	Choice of the model catalyst	33
3.2	Substrate	35
3.3	Choice of the precursor	37
3.4	Deposition of thin-films	38
3.5	Conclusion	45
4	Impact of IrO_x species and catalyst-substrate interactions on the OER activity and stability	46
4.1	Physico-chemical material characterization	48
4.2	Temperature programmed reduction: Ir oxide and its interaction with the Ti substrate	59
4.3	Electrocatalytic OER activity	61
4.4	Potential-resolved dissolution measurements of Ir and Ti	64
4.5	Conclusions	69
5	Molecular insight in structure and activity of highly efficient Ir-Ni oxide catalysts for electrochemical water splitting (OER)	71
5.1	Electrocatalytic OER activity and Ir dissolution	72
5.2	Electrochemical Ni dissolution, compositional, and morphological stability	75
5.3	Atomic structure of Ir-Ni mixed oxides	79
5.4	Electronic band structure and surface chemical state of Ir-Ni mixed oxides	80
5.5	The surface electrochemistry of Ir-Ni mixed oxide catalysts	84
5.6	Structure-reactivity correlations and catalytic performance descriptors	85
5.7	Conclusions	88

6 OER performance comparison: Ir-Ni mixed oxides versus pure Ir oxide films calcined at different temperatures.....	89
6.1 Conclusion.....	94
7 In-situ detection of surface species during the OER using shell isolated nanoparticle enhanced Raman spectroscopy	95
7.1 Introduction.....	95
7.2 Characterization of the RuO ₂ thin-film catalyst.....	97
7.3 Characterization of silica coated gold nanoparticles	99
7.4 Design of electrochemical in-situ SHINERS cell	102
7.5 In-situ SHINERS measurements.....	104
7.6 Conclusion.....	109
8 Conclusion and Perspective	110
8.1 Pure Ir oxides and their interaction with the Ti substrate.....	110
8.2 Ir-Ni mixed metal oxides	111
8.3 Comparison: IrNi mixed oxide vs. pure Ir oxides calcined at different temperatures	112
8.4 In-situ Raman spectroscopic investigation of RuO ₂	113
8.5 Perspective.....	114
9 Appendix	115
10 References	123
11 List of Figures	127
12 List of Tables.....	132
13 List of Publications	133
14 List of Abbreviations	135

1 Introduction

1.1 Proton exchange membrane (PEM) based water electrolysis- the technology of choice for storage of renewable electricity

Fossil energy carriers and nuclear power are still used to satisfy a substantial part of the electricity demand in Germany (about 70%, see Figure 1). However, the finite nature of the corresponding fuels prospectively leads to supply problems and, thus, to a limited reliability. Moreover, combustion of fossil fuels causes air pollution and nuclear power plants constitute safety risks related to the release of radioactive substances as well as problems related to the storage of radioactive waste. All these disadvantages can be overcome using renewable electricity generation for example by solar or wind power. In 2014 only ~30 % of the electricity generated in Germany was generated by the renewables wind, solar, hydro and biomass together but brown coal still provided the largest single contribution with close to 27 % (140.7 TWh) (see Figure 1).¹

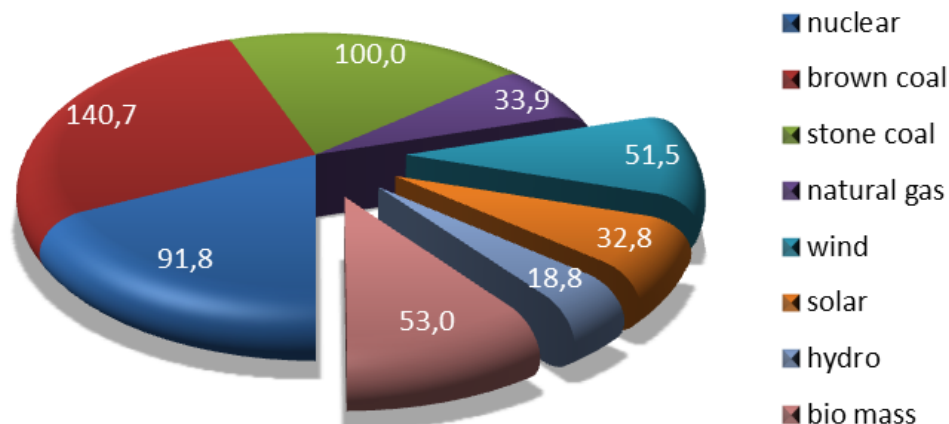


Figure 1: *Electricity generation in Germany in 2014 itemized by energy carriers (unit: TWh). Data obtained from ¹.*

On the way to an energy infrastructure exclusively based on renewables several problems have to be solved, one of which is their intermittent availability, as can be seen from Figure 2. Therein, photovoltaic and wind based electricity generation are shown to strongly fluctuate as function of time. Photovoltaics show a rather periodic electricity generation during the course of a day, with albeit varying maximum around noon, whereas wind power based electricity generation appears to be unpredictable at all.

According to their random character, wind and solar based electricity generation are not expected to coincide commonly with the system load. Thus, large scale energy storage solutions are indispensable to store excess electricity and release it upon request.

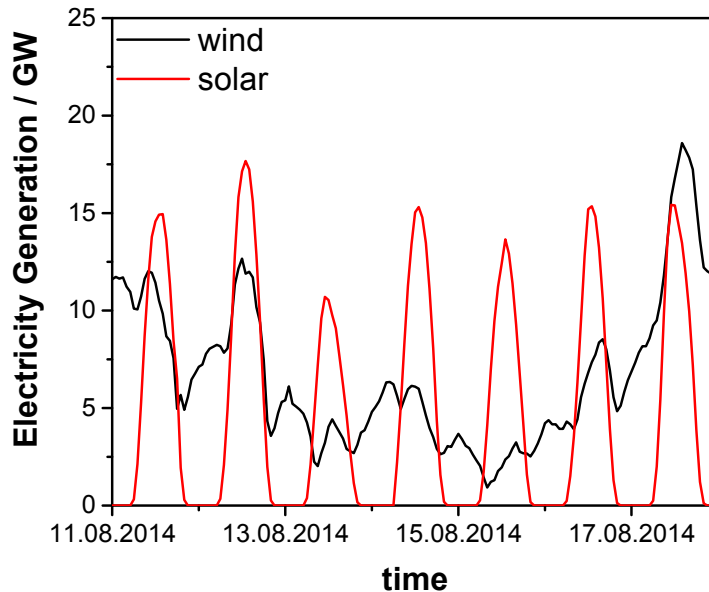


Figure 2: *Time dependent electricity generation from wind and solar power in Germany during one week in August 2014. Data obtained from ¹.*

Several different energy storage solutions are available for different time scales like flywheels, double layer capacitors, batteries, pump-storage plants, compressed air reservoirs and water electrolyzers.² In this context, hydrogen produced by water electrolysis is a very promising candidate, since hydrogen as energy carrier has an outstanding flexibility. Hydrogen can be used for stationary as well as mobile applications, it can be efficiently stored, efficiently transported over large distances, efficiently produced by water electrolysis and efficiently reconverted into electricity using fuel cells.³ In a transition period hydrogen can additionally be used to run combustion engines. The vision of a Hydrogen economy in which hydrogen is used as universal, clean and efficient energy carrier was already published in 1972 in a pioneering work by Bockris.⁴ Although Bockris suggested hydrogen production driven by nuclear power plants, which has severe drawbacks compared to renewable electricity generation as explained before, most of his visions still appear reasonable and forward-looking.

Unfortunately, more than 40 years after Bockris has published his vision, it has still not become reality. The hydrogen economy requires technologies for hydrogen production, storage, distribution and reconversion into electricity.⁵ Each of these technologies has to be reliable, safe and economically competitive to facilitate the hydrogen economy. However, many aspects of these technologies remain inappropriately solved and scientifically challenging up to date.⁵

Considering the hydrogen production by water electrolysis, three principally different electrolyzer types are available which can be distinguished by the applied electrolyte. In particular, a liquid alkaline solution, a solid ion conducting oxide or a proton exchange membrane (PEM) are used as electrolyte.⁶ In common alkaline water electrolyzers anode and cathode compartment, and thereby the products oxygen and hydrogen, are separated by a diaphragm and a liquid alkaline electrolyte is used.² In contrast to that, PEM electrolyzers make use of a thin proton conducting polymer membrane which acts as electrolyte and also separates hydrogen and oxygen. The third electrolyzer type is based on solid oxide electrolytes which conduct oxygen ions at high operating temperatures (usually 900-950°C),⁷ whereas alkaline and PEM electrolyzers are operated at much lower temperatures⁶.

Important criteria to evaluate the suitability of the different electrolyzer types for the storage of renewable energies are their dynamic and partial load behavior. The former describes how fast the electrolyzer can be switched between different loads. The partial load behavior describes in which load ranges the electrolyzer can be operated. High temperature electrolysis is the least suitable technology with respect to the dynamic behavior.² The high operating temperature has to be maintained to keep the device operable and to allow for a quick response on load changes. Heating and cooling are comparably time consuming for high temperature electrolysis and cause thermal stress in the material giving rise to material damages.² In contrast, alkaline and PEM electrolyzers are operated at much lower temperatures allowing a quicker response to varying loads.² Hereby, the PEM electrolyzer can react even faster than the alkaline electrolyzer due its compact design and low electrolyte volume which result in a comparably low heat capacity.² Thus, from a dynamic point of view the PEM electrolyzer is the most appropriate choice for the storage of renewable electricity.

Considering the partial load behavior, PEM electrolyzers offer additional advantages as they can be operated in a larger partial load range than alkaline electrolyzers due to a comparably small gas cross over between cathode and anode compartment, achieved by the PEM.^{3,6} Therefore, sufficient gas purities can be obtained over a wide load range without safety issues occurring from explosive hydrogen-oxygen-mixtures. Thus, with regard to the partial load behavior, the PEM electrolyzer is the most suitable electrolyzer type. Moreover, PEM electrolyzers offer low ohmic losses and can be operated at high current densities.⁶ The sum of these advantages identifies the PEM electrolyzer as optimal electrolyzer type for wind and solar power driven water electrolysis.

Unfortunately, PEM electrolyzers have one inherent drawback. Due to the acidic conditions rare noble metal catalysts are required for stability reasons.⁶ Thus, improved catalysts with maximized activity at minimized noble metal content are required to facilitate the economically competitive large scale application of PEM based water electrolysis. In PEM electrolyzers, the anodic half-cell reaction, the oxidation of water to oxygen (oxygen evolution reaction (OER)), accounts for a major part of the catalytic overpotential due to a complex four electron mechanism (see section 1.4).⁸ Hence, PEM anode catalysts will be the main subject of this work.

1.2 PEM OER catalysts - brief review and current status

Before PEM OER catalysts are described the development of catalysts for the chlorine evolution reaction (CIER) is reported briefly, since findings in the area of the CIER formed the basis for the development of PEM OER catalysts.

In the 1950's and 1960's Beer performed his pioneering work on Dimensionally Stable Anodes (DSA[®]) for the CIER, which consisted of Ti supported noble metal oxide electrodes.⁹ DSAs[®] substituted graphite as anode material in the chlor-alkali electrolysis. Under the applied reaction conditions, the graphite electrodes were not stable leading to sludge formation. The sludge formation resulted in a rather short lifetime¹⁰ and rendered graphite electrodes inapplicable for membrane cells, since the sludge (graphite particles detached from the anode) would clog the membrane⁹. Considering the development of the DSA[®], Beers initial discovery was that Ti can act as inert anode material in various different electrolytes.⁹ Although Ti is a non-noble metal and therefore thermodynamically

unstable under the high potentials and acidic conditions inherent for the CIER, it is covered efficiently by a thin passivating oxide layer which protects the metal below from oxidation but still ensures a sufficient electric conductivity.^{10,11} Thus, Ti is not only well suited as substrate material for CIER anodes but also for OER catalysts, due to the rather similar reaction conditions. Beside its use as catalyst substrate material, Ti has also shown to be the material of choice for other components in the anode compartment of PEM electrolyzers such as current collectors.⁶

Developing DSAs[®], Beer initially deposited metals from the platinum group on Ti and found that they were not stable enough during the CIER to be economically competitive with graphite anodes.⁹ However, substitution of the noble metals with their respective oxides from the platinum group, especially RuO₂, resulted in the desired stability for the CIER.⁹ To obtain the DSA[®] RuO₂ was mixed with TiO₂ and/or other valve metal oxides to disperse the active component RuO₂ and further improve the stability for the CIER.⁹

In contrast to the CIER, RuO₂ based DSAs[®] showed an insufficient long-term stability for the OER.¹² As substitute, several different platinum group metal oxides were investigated with respect to their OER activity in acidic media and compared with Ru leading to the following activity trend: Os>Ru>Ir>Pt>Au.¹³ However, Os oxide showed an even lower stability during the OER than Ru.¹³ Since the OER stability of Ru oxide was already rendered insufficient,¹² Os is inappropriate as OER catalysts for stability reasons. Compared to Ru oxide, Ir oxide has a slightly lower OER activity but a considerably higher stability,^{12,14,15} rendering it one of the most appropriate PEM OER catalyst materials.

Ir oxide can be synthesized through various routes like electrochemical oxidation of metallic Ir¹⁶⁻¹⁸, physical vapor deposition techniques¹⁹ or thermal decomposition of a suitable precursor²⁰⁻²³. Considering the electrochemical oxidation of Ir, a hydrous Ir oxide can be grown on metallic Ir by potential cycling whereby the oxide thickness can be controlled by the number of applied cycles.¹⁶⁻¹⁸ The Ir oxide formation rate depends on various parameters like scan rate, potential boundaries, temperature and electrolyte concentration.²⁴ However, at potentials higher than 1.65 V_{RHE} electrochemically grown Ir oxide films are removed from the electrode indicating stability problems.¹⁸ In contrast to

the anodically grown Ir oxide films, sputtered Ir oxide films show a higher stability during the OER, as demonstrated at 1.85 V_{RHE} in 0.5M sulphuric acid.¹⁹ Furthermore, an exceptional stability was found for thermally prepared Ir oxide films, which show considerably lower Ir dissolution rates than electrochemically formed Ir oxides.²⁵

The highly stable, thermally prepared Ir oxides are commonly prepared, similarly to DSA[®] type electrodes, by thermal decomposition of an Ir chloride precursor on a Ti substrate.²⁰⁻²³ Therefore, an Ir chloride solution is mechanically spread, commonly brushed, on a Ti substrate, then dried and subsequently calcined in air.^{26,27} This methodology generally results in films with a morphology resembling to cracked-mud due to the thermal shock during calcination.²² Thus, the several micro meter thick oxide films²² show position dependent deviations in morphology with the tendency of an uneven film-thickness. Oliveira-Sousa et al. demonstrated that the morphology and electrocatalytic properties including the OER activity of these thermally prepared Ir oxides depend critically on the chemical nature of the precursor solution.²⁶

Ouattara et al. compared Ir oxides prepared by electrochemical oxidation of Ir with those prepared by thermal decomposition of a chloride-based Ir precursor. Although the kinetics of Ir oxidation and reduction were much faster for electrochemically prepared Ir oxide, both oxides provided a similar surface specific OER activity and Tafel slope.²⁸ However, the stability was lower for the electrochemically prepared Ir oxide.²⁸ The hydrous electrochemical Ir oxide can be converted by heat treatment into an Ir oxide showing similar electrochemical properties as an Ir oxide prepared by thermal precursor decomposition.²⁹ Furthermore, the properties of the electrochemical oxide can be restored from the thermally treated oxide by low-potential excursion or square wave pulses (-0.25 V_{SCE} to 1.25 V_{SCE}, 2 Hz, 0.5 M H₂SO₄).²⁹ A comparison between Ir oxides prepared by thermal oxidation of Ir metal or, respectively, thermal decomposition of an Ir chloride precursor yielded similar CVs and OER activities in both cases,³⁰ indicating that rather similar Ir oxides were synthesized. Although Fierro and Ouattara found comparable OER activities for Ir oxides prepared by electrochemically and thermally oxidation of metallic Ir as well as thermal precursor decomposition,^{28,30} Danilovic et al. reported that thermally oxidized Ir results in a lower OER activity than electrochemically oxidized Ir, whereas the stability behaves inverse.¹³ The deviating results indicate that

the OER activity and the stability are highly sensitive towards the actual synthesis parameters. In summary, Ir oxides and hereby especially those prepared by thermal precursor decomposition, appear to be the most appropriate choice as PEM OER catalysts.

Unfortunately, Ir is one of the scarcest non-radioactive metals²⁴ on earth with a ten times smaller abundance than Pt⁶. Thus, the Ir content in OER catalysts has to be reduced to a minimum while conserving the beneficial material properties of Ir oxide to allow for a large scale economically competitive application. In order to minimize the Ir amount required, first the chemical and structural reasons for the observed OER activity and stability of pure Ir oxide have to be understood. On this basis strategies for low Ir content catalysts can be developed purposefully.

So far different approaches have been pursued for the reduction of the Ir amount required in OER catalysts. A common approach is to mix Ir oxide with one or more other components, which in most cases leads to a better dispersion of Ir. A well-studied system in this respect is Ru-Ir mixed oxide in which both components are highly active for the OER. The electrocatalytic properties of this mixture are suited in between that of pure Ir and Ru oxide, whereby Ru oxide is more active for the OER but less stable than Ir oxide.³¹⁻³³ This mixed oxide can be optimized by Ir surface segregation which increases the stability during the OER without affecting the OER activity.³⁴ However, Ru is, similar to Ir, a scarce metal of the platinum group and thus the substitution of Ir by Ru does not satisfactorily solve the supply and cost issues.

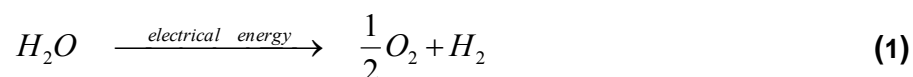
Beside mixtures with a second active component such as Ru oxide, Ir oxide is commonly mixed with an inert oxidic component to dilute the active Ir oxide. For example mixtures of Ir oxide with oxides of Ti³⁵, Mn³⁶, Ta³⁵, Nb³⁷, Sb³⁸, Sn^{39,40} or Si^{41,42} have been prepared. Based on these mixtures the Ir utilization compared to pure Ir oxide could be improved by a factor of 3.5⁴¹, 9³⁹ or 11³⁶ for mixtures with Si, Sn, or Mn oxide, respectively. However, morphology, film-thickness and absolute Ir loading were not reported in each case adding an uncertainty to the absolute value of the Ir utilization. Beside mixing Ir oxide with other components it can also be highly dispersed using a high surface area conductive corrosion resistant supports e.g. based on doped tin

oxides, as reported from Oh et al⁴³. However, dispersing alone is most likely enough to achieve the required reduction of the Ir amount; a further reduction of the Ir amount can be obtained if the intrinsic OER activity and stability of Ir oxide are tuned to a maximum. Unfortunately, the material properties determining the OER activity and stability of Ir oxide remain uncertain up to now impeding a purposeful optimization. For this reason, identifying the material properties relevant for the OER performance of Ir oxide is of utmost importance for an efficient knowledge based optimization of Ir oxide based PEM OER catalysts. Therefore, a system is required in which the OER performance can be continuously tuned. By tuning the OER activity and stability and assessing the consequent changes in the materials properties, one can uncover the governing structure-activity-stability correlations.

Considering Ru oxide, the addition of Ni yielded an improved tunable intrinsic OER-activity depending on the Ni content,⁴⁴ which was explained by Ni-rich defects in the Ru oxide lattice acting as preferential sites for the OER⁴⁵. Unfortunately, Ru oxide suffers from severe corrosion under PEM-OER conditions, rendering it less appropriate than Ir oxide, although it is slightly more active.^{14,46-48} Nong et al. demonstrated that Ir utilization and intrinsic Ir activity for the OER can be improved using metallic Ir-Ni alloy catalysts which were electrochemically dealloyed and oxidized,^{49,50} indicating the potential of this approach for a continuous variation of Ir oxide material properties. However, this approach has to be extended to thermally prepared oxides, since thermally prepared oxides provide the superior stability²⁵ required for PEM electrolyzers.

1.3 Basic considerations about water splitting with emphasis on the oxygen evolution reaction (OER)

The electrocatalytic splitting of water can be described by the following chemical equation (equation (1)).



Under standard conditions (standard temperature and pressure - STP) this reaction has a Gibbs free energy $\Delta_R G^0$ of +237.1 kJ mol⁻¹ and a reaction enthalpy $\Delta_R H^0$ of +285.8 kJ

mol⁻¹ (for liquid water, higher heating value).⁵¹ Thus, this reaction is endergonic and endothermic, hence energy is required to drive the reaction in the shown direction.

The minimum electrical energy required to run the water splitting reaction (equation (1)) under reversible equilibrium conditions equals $\Delta_R G^0$ of this reaction.⁸ Thus, the equilibrium potential under standard conditions can be calculated according to equation (2), wherein n denotes the number of electrons transferred, F is the faraday constant and $E_{eq,0}$ the equilibrium potential.⁸

$$\Delta_R G^0 = n F E_{eq,0} \quad (2)$$

Since two electrons are transferred per water molecule, equation (2) yields a value of 1.23 V for $E_{eq,0}$ for the water splitting reaction under STP.

The overall water splitting reaction shown in equation (1) can be divided into a cathodic (equation (3)) and an anodic (equation (4)) half-cell reaction.



Equation (3) reflects the reaction of the standard hydrogen electrode (SHE). Under STP (with $p(H_2)=1$ bar) and $pH=0$ the $E_{eq,0}$ of the SHE equals a value of 0 V. Thus, $E_{eq,0}$ of the anodic half-cell reaction, referred to as oxygen evolution reaction (OER), equals a value of 1.23 V if quoted against the SHE, similar to the overall water splitting reaction. Similarly, 1.23 V are the $E_{eq,0}$ of the OER versus a reversible hydrogen electrode (RHE) in the same electrolyte independent of the pH value of the electrolyte.

The difference between the RHE and SHE scale is that the pH value for the RHE scale is determined by the applied electrolyte and, thus, it is not fixed whereas the pH value is, by definition, zero in case of the SHE. The correlation between RHE and SHE is shown in equation (5).⁵² Fortunately, the RHE and the OER half-cell reaction show an identical pH dependence of their equilibrium potentials (compare equation (5) and (6), wherein $E_{0,OER}$ denotes the standard equilibrium potential of the OER). This is because both processes involve concerted proton electron transfers. Thus, if measured against a

RHE, the thermodynamic potential of the OER equals 1.23 V independent of the electrolyte pH value.

$$E_{RHE} = E_{0,SHE} - 2.303 \cdot \frac{RT}{F} \cdot pH \quad (5)$$

$$E_{OER} = E_{0,OER} - 2.303 \cdot \frac{RT}{F} \cdot pH \quad (6)$$

The difference between the potential required to practically run a reaction and the thermodynamic equilibrium potential is referred to as overpotential. Thus, the overpotential describes efficiency losses and should, therefore, be minimized. These efficiency losses can relate inter alia to mass transport phenomena, ohmic resistances and the catalytic reaction process.⁵³ This work will focus on overpotentials related to the catalytic process and, hence, other losses will be excluded from the investigation as far as possible by an appropriate choice of the experimental conditions and subsequent corrections. Possible reasons for the overpotentials of the catalytic process will be provided in the following.

1.4 Mechanism of the OER

Although the OER, as anodic part of the water splitting reaction, was discovered already in 1789,⁵⁴ the atomistic details of the OER mechanism on heterogeneous electrocatalysts still remain uncertain. Propositions for the OER mechanism have been made mainly based on the kinetic analysis^{8,55,56} of catalytic data and DFT calculations^{57,58}. Bockris demonstrated that each conceivable elementary reaction in an OER mechanism, on a stable catalyst surface, is related to a characteristic Tafel slope, if the considered elementary reaction constitutes the rate determining step.⁵⁶ Thus, an experimentally observed Tafel slope provides evidence for the actual rate determining step. However, even if the correct rate determining step is identified, this does not necessarily identify the complete reaction mechanism, since some conceivable mechanisms share certain elementary reactions.⁵⁶ Furthermore, the Tafel slope is somewhat unspecific as criterion for the identification of the rate determining step, as, for instance, chemical transformations on the catalyst surface, mass transport effects, or

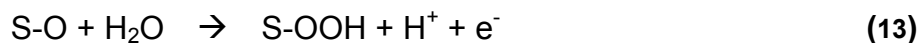
the presence of a semiconducting interlayer between catalyst and substrate may change the apparent Tafel slope, as demonstrated by Scheuermann et al..⁵⁹

Kinetic analysis based on RuO₂ catalysts in acidic media have resulted in the following mechanistic hypothesis of elementary reactions for the OER, wherein S denotes an active surface site on the catalyst:⁸



The reaction sequence (7), (8) and (10) on the one hand and the sequence (7), (9) and (10) on the other hand constitute possible pathways for the OER.

In contrast to that earlier mechanism, more recent work proposed the following mechanism for the OER:^{57,58}



Within this mechanistic proposal the direct recombination of two oxygen atoms adsorbed on the catalysts surface was not included, since this reaction step is thought to show a too high activation barrier.⁵⁷ The absence of any purely chemical elementary step also made the analysis of the process in terms of potential dependent free energy diagram easier.

However, in-situ spectroscopic insights identifying which of the proposed mechanisms actually takes place have virtually remained elusive. Indications for an S-OOH intermediate were found recently by ambient pressure XPS on an Ir oxide catalyst.⁶⁰ Moreover, an OOH species was identified in-situ during the OER by surface enhanced Raman spectroscopy (SERS) on roughened gold electrodes.^{54,55} However, this Au-OOH species was already observed at potentials of ~ 1.4 V_{RHE} although the OER commences at around 2.0 V_{RHE} on Au electrodes under the applied conditions.⁵⁴ This observation was explained by an oxide decomposition mechanism in which the Au-OOH species formed at ~ 1.4 V is decomposed at ~ 2.0 V into O₂ and other products, whereby the O₂ is exclusively stemming from the Au oxide, as was shown by mass spectroscopy in isotopic exchange experiments.⁵⁴ Unfortunately, Ru and Ir oxide both do not follow the oxide decomposition mechanism observed on Au, as was additionally shown by mass spectroscopy.^{47,54,61,62} Thus, the Raman spectroscopic insights obtained on gold might not be transferable to benchmark catalysts like Ru and Ir oxide.

1.5 Origin of catalytic overpotentials in the OER

1.5.1 Thermodynamic considerations

This section is mainly based on⁵⁷.

The DFT based mechanistic proposal shown in equations (11)-(14) includes four consecutive elementary reactions for which the corresponding $\Delta_R G^0$ values are shown in equations (15)-(18). From a thermodynamic point of view each single step has to have a $\Delta_R G^0$ smaller than zero in order to allow the respective reaction to proceed in the forward direction. Hence, only if each single step becomes downhill in $\Delta_R G^0$ the whole reaction sequence is thermodynamically allowed to proceed from water to oxygen. Since one electron is transferred in each step, $\Delta_R G^0$ of each step is similarly changed by the electrode potential E (see equations (15)-(18)). Thus, the step with the most positive $\Delta_R G^0$ (at a similar reference potential, e. g. 0 V) requires the most positive electrode potential E in order to obtain a negative value for $\Delta_R G^0$. The electrode potential at which the last elementary step has turned exergonic is the potential at which the whole reaction sequence from water to oxygen becomes thermodynamically feasible. This step will be referred to as potential-determining step. The difference between the potential

required to make the potential-determining step exergonic and the thermodynamic equilibrium potential of the overall reaction from water to oxygen describes a thermodynamic overpotential. This is exceptional since overpotentials are usually caused by kinetic limitations. Note that the before mentioned model does not take into consideration any kinetic barriers which may affect the observed overpotential as well (see section 1.5.2).

$$\Delta_R G_1^0 = \Delta G_{S-OH}^0 - \Delta G_{H_2O}^0 - eE + kT \ln(a_{H^+}) \quad (15)$$

$$\Delta_R G_2^0 = \Delta G_{S-O}^0 - \Delta G_{S-OH}^0 - eE + kT \ln(a_{H^+}) \quad (16)$$

$$\Delta_R G_3^0 = \Delta G_{S-OOH}^0 - \Delta G_{S-O}^0 - eE + kT \ln(a_{H^+}) \quad (17)$$

$$\Delta_R G_4^0 = \Delta G_{O_2}^0 - \Delta G_{S-OOH}^0 - eE + kT \ln(a_{H^+}) \quad (18)$$

As described in section (1.3), $\Delta_R G^0$ of the overall reaction from water to oxygen has a fixed value ($\Delta_R G^0 = +237 \text{ kJ mol}^{-1}$ at STP). According to Hess's law the sum of $\Delta_R G_1^0$, $\Delta_R G_2^0$, $\Delta_R G_3^0$ and $\Delta_R G_4^0$ has to equal $\Delta_R G^0$ of the overall reaction. Under this boundary condition, $\Delta_R G^0$ of each elementary reaction can be changed. Since the reaction with the highest $\Delta_R G^0$ in the sequence determines the potential at which the sequence can proceed from water to oxygen, the lowest possible potential for the overall reaction can be achieved, if $\Delta_R G^0$ of each step is identical and, thus, equals a quarter of $\Delta_R G^0$ of the overall reaction. In this case the whole reaction sequence would be thermodynamically allowed in the forward direction just above 1.23 V.

Theoretically, $\Delta_R G^0$ of each individual elementary reaction could be tuned to make the overall reaction thermodynamically feasible just above 1.23 V changing the Gibbs free adsorption energy of the involved surface intermediates (ΔG_{S-OH}^0 , ΔG_{S-O}^0 , ΔG_{S-OOH}^0) and, thus, the adsorbate binding energies. This would require an independent optimization for each of the three adsorbates. Unfortunately, this is impossible under practical conditions, because their binding energies are correlated (on (110) rutile type oxide surfaces).⁵⁷ This correlation is referred to as “scaling relation” in the sense that the binding energies scale with each other. In other words, if the binding strength of one

intermediate is increased the binding strength of the other intermediates will be increased proportionally. Despite this limitation the adsorbate binding energies can still be optimized to the top of a so called activity volcano plot. But due to the scaling relation, it is not possible to lower the over potential to 0 V for the overall reaction.

Since the adsorbate binding energies are correlated, one of these binding energies can serve as descriptor to characterize all adsorbate binding energies, which is the binding energy of O (ΔE_O). Values for $\Delta_R G^0$ of each elementary step are plotted as function of ΔE_O (see Figure 3). Since only the elementary reaction with the highest $\Delta_R G_{max}$ is decisive, the respective values are shown as thick lines in Figure 3, whereas the other $\Delta_R G^0$ are shown as dashed lines. The optimal ΔE_O under the given conditions is located at ~ 2.4 eV, since $\Delta_R G_{max}$ showed a minimum at this ΔE_O value. Calculations demonstrated that RuO₂ offers a ΔE_O close to this value⁵⁷ in accordance with the high OER activity observed experimentally for RuO₂ (see chapter 1.2).

The spectroscopic observation of an S-OOH surface species described in section 1.4 appears on the first glance to support the OER reaction mechanism described by equations (11)-(14). However, the spectroscopic observation of a certain surface species appears only to be probable in case this species has a high surface coverage. For obvious reasons a high surface coverage of the respective intermediate is only expected, if it constitutes a reactant of the rate or, respectively, potential-determining step. Unfortunately, the last step of the reaction sequence (equation (14)) becomes only potential determining for very strong adsorbate binding, which is not expected on a noble metal like gold. Thus, the spectroscopy observation of an S-OOH surface intermediate does not directly support the mechanism described by the reaction sequence shown in equations (11)-(14).

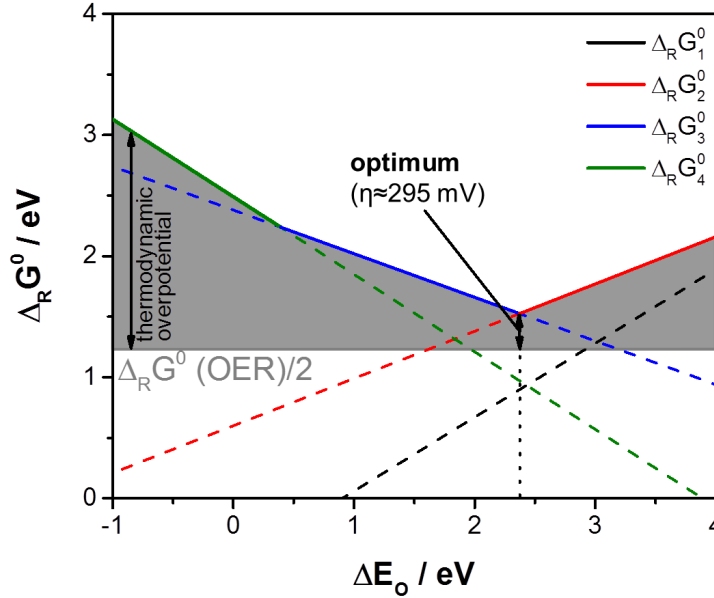


Figure 3: Gibbs free energy of each elementary reaction ($\Delta_R G_1^0$, $\Delta_R G_2^0$, $\Delta_R G_3^0$, $\Delta_R G_4^0$) plotted as function of ΔE_O for $E=0$ V and $a_{H^+}=1$ according to ⁵⁷. The Gibbs free energy of the overall reaction (OER) is provided for comparison (divided by the number of electrons transferred per water molecule, $n=2$).

1.5.2 Overpotentials related to the catalytic process - Butler-Volmer Kinetics

An electrochemical single step reaction at its thermodynamic equilibrium potential can be accelerated in the anodic or cathodic direction applying a positive or negative overpotential according to the Butler-Volmer equation (equation (19)).⁶³

$$j = j_0 \left[\exp\left(\frac{(1-\beta)nF}{RT}\eta\right) - \exp\left(-\frac{\beta nF}{RT}\eta\right) \right] \quad (19)$$

Herein, j describes the current density, β the asymmetry parameter, n is the number of transferred electrons, F the Faraday constant, R the universal gas constant, η the overpotential and j_0 the exchange current density.

In case of a sufficiently large overpotential in either direction, the second exponential term in the Butler-Volmer equation can be neglected. In case of positive overpotentials this leads to the so called Tafel equation (equation (20)).⁶³

$$\lg(j) = \lg(j_0) + \frac{(1-\beta)nF}{2.3RT} \eta \quad (20)$$

However, the Butler-Volmer equation (equation (19)) was derived for a single electron transfer reaction without consecutive steps.⁶³ Although every proposal for the OER mechanism presented in section 1.4 includes in maximum a transfer of 1 electron per elementary step, the complete four 4 electron mechanisms always include several consecutive steps. Thus, a more sophisticated kinetic modelling is required to describe the OER kinetics, for which, unfortunately, detailed knowledge of the actually proceeding OER mechanism is mandatory. Although different mechanistic proposals were made for the OER, spectroscopic insights are rare, especially on benchmark PEM OER catalysts like Ru oxide, rendering the actually present mechanism uncertain. Moreover, as long as the mechanism remains uncertain, the reasons for the kinetic overpotential cannot be uncovered. This underlines the need for in-situ spectroscopic insights under reaction conditions.

1.6 Motivation

As pointed out in the last sections, Ir oxide is one of the most suitable PEM OER catalysts with regard to its material properties, but, unfortunately, Ir is an extremely rare element of cosmic meteoritic origin⁶⁴ with a ten times lower abundance than Pt⁶. Hence, the Ir amount required in PEM OER catalysts has to be reduced to a minimum in order to allow the economically competitive large scale application of PEM electrolyzers. Therefore, the intrinsic OER activity of Ir oxide has to be tuned to a maximum since dispersing alone appears not to be sufficient with regard to the rareness of Ir. Unfortunately, the material properties determining the OER performance of Ir oxide are uncertain, impeding the purposeful optimization of the intrinsic OER activity.

While maximizing the OER activity of the catalyst, the stability must not be neglected, since a high catalyst stability is critical for PEM electrolyzers to facilitate long service life times. The dissolution of the active noble metal component of the catalyst is of utmost importance in this context. However, the stability against dissolution is a combination of intrinsic properties of the catalyst and the operating conditions, hence, it is challenging to optimize. To date, it also has remained elusive whether there is a universal relation between activity and stability trends of OER catalysts; that is, can the OER activity be enhanced without sacrificing the catalyst stability.

In the context of the OER, substrate and support-related effects on the OER activity have so far been mostly overlooked, although they have a potentially strong influence on the OER activity. Considering the common substrate Ti, several different catalyst-substrate interactions appear plausible. For instance, the catalyst can be chemically influenced by the substrate or an interlayer of a new compound can be formed at the junction between catalyst and substrate. Thus, knowledge about the catalyst-substrate is required to avoid any diminution of the OER performance.

In order to solve the problems described before and obtain improved PEM-OER catalysts, the following issues are of utmost importance and need to be clarified:

- The nature of catalyst-substrate interactions
 - Are catalysts-substrate interactions present for PEM OER catalysts on Ti substrates?
 - What are the properties of the catalyst-substrate interface?
 - If catalyst-substrate interactions are present how do they affect the OER performance and how can they be avoided?
- Determinants of OER activity and stability of Ir oxide
 - Which material properties of Ir oxide determine its OER activity and Ir stability against dissolution?
 - How can these material properties be modified to optimize the OER performance of Ir oxide?
- The detailed OER mechanism and intermediates
 - Which technique is appropriately applicable to investigate the OER mechanism in-situ on benchmark catalysts?
 - What is the rate determining step of the OER on benchmark catalysts?

This work addresses the issues above and aims to provide answers to the mentioned problems and open questions. The overall goal is a deeper fundamental insight in the OER catalysis which will enable knowledge-based catalyst design and demonstrate possible synthesis pathways towards improved PEM-OER catalysts.

2 Experimental part

2.1 Preparation of thin oxide films

2.1.1 Substrates

Si wafers, Ti coated Si wafers (TS) and Ti cylinders were used as substrates for the deposition of thin oxide films. The substrates were selected according to their suitability to determine the desired information by appropriate analytical techniques (for further details see section 3.2 and 4).

2.1.1.1 *Si wafers*

Si wafers (<100>, B doped, Siegert Wafer) were broken into rectangular pieces prior to the thin-film deposition via spin-coating.

2.1.1.2 *Ti coated Si wafers (TS)*

A ~90 nm thick Ti film was deposited on Si wafers (<100>, B doped, Siegert Wafer) by electron beam physical vapor deposition. Prior to the Ti deposition the Si wafers were cleaned in an oxygen plasma and then in an argon plasma. For their use as spin coating substrates, the TS were broken into rectangular pieces similar to the Si wafers.

2.1.1.3 *Ti cylinders*

Ti cylinders were manufactured by cutting 4 mm thick pieces from Ti rods of 10 mm diameter (Gemmel, grade 1 or, respectively, Chempur, 99.6%). Thereafter, the obtained cylinders were fixed in a custom made central force sample holder (see Figure 4a and c) for grinding and polishing, in which the Ti cylinders are screw tightened within the drop-shaped holes.

With an additional height adjustment tool (see Figure 4b and c) the cylinders were adjusted to stick out of the holder all with the same height. To adjust this height the sample holder is laid on the higher supporting surface of the adjustment tool and screw tightened in this position. In this configuration (shown in Figure 4c) the Ti cylinders are put into the holes so that they lay on the lower supporting surface. Then, the cylinders are screw-tightened by the grub screws. Using this sample holder the Ti cylinders were grinded and polished consecutively to a mirror-like surface finish in a half automatic

polishing machine (AutoMet 250, Buehler). First, all cylinders were ground with SiC grinding paper (P320, Buehler, force for 8 cylinders: 40 N, complimentary rotation, base: 200 rpm, head: 60 rpm) to remove all machining marks from the cutting process. Hereafter, diamond suspension (MetaDi Supreme, 9 μm , Buehler, force for 8 cylinders: 50 N, contra rotation, base: 150 rpm, head: 30 rpm, 10 min) and silica suspension (MasterMet 2, 0.02 μm , Buehler, force for 8 cylinders: 40 N, contra rotation, base: 150 rpm, head: 30 rpm, 10 min, this step was repeated until the desired surface finish was obtained) were used consecutively in combination with an UltraPad or, respectively, a MicroCloth polishing cloth to polish the Ti cylinders to a mirror like surface finish. Afterwards, the cylinders were sonicated in distilled water to remove polishing residues. Further surface impurities stemming from the Ti rods, mostly iron, were removed by treating the polished cylinders in hot ($\sim 150^\circ\text{C}$, 2 h) nitric acid (23%, prepared by dilution of 69% HNO_3 , AnalaR Normapur). Thereafter, the cylinders were consecutively sonicated in water, acetone and again in water.

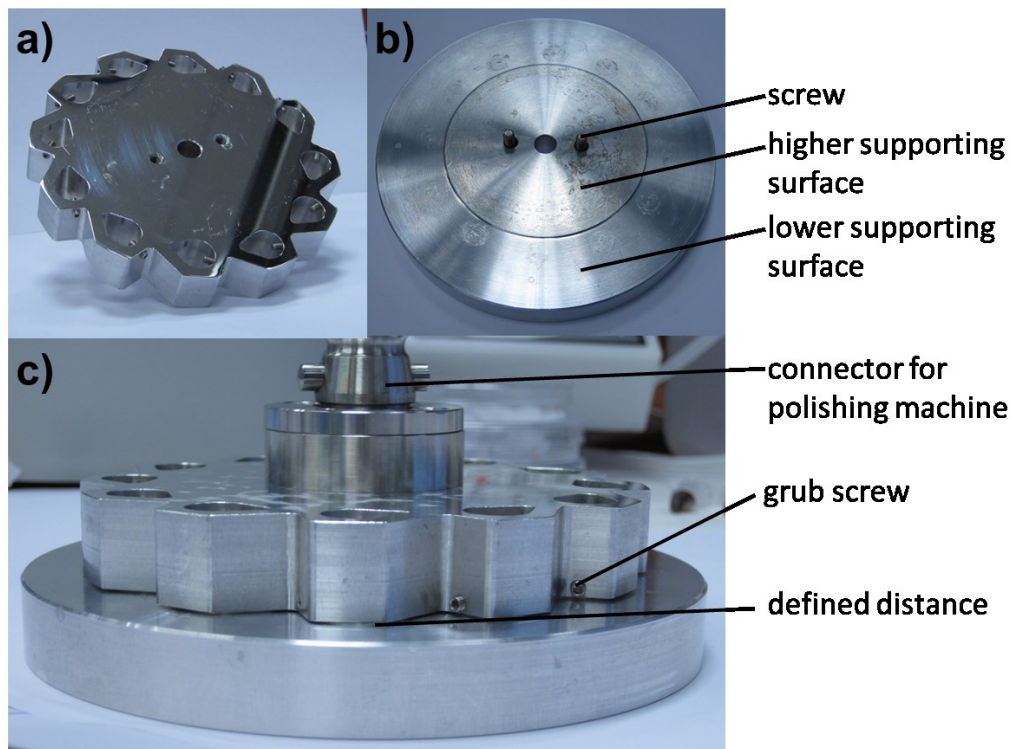


Figure 4: *a: Custom made central force sample holder for grinding and polishing of Ti cylinders. b: Sample height adjustment tool for the polishing sample holder. c: Polishing sample holder mounted onto the height adjustment tool.*

2.1.2 Deposition of thin precursor films via spin-coating

Thin precursor films were applied onto the substrates by spin coating (WS-650MZ-23NPP, Laurell). During the spin-coating process the samples need to be mounted firmly due to the occurring large acceleration and the high rotational velocities. Commonly, a sample holder is used on which the sample is placed on top and then adhered from the back by applying vacuum (see Figure 5a).

For the coating of Ti cylinders a custom made sample holder was used, which was manufactured from polyoxymethylene (POM) (see Figure 5b and c). Considering this sample holder, the Ti cylinder was first inserted into a tapered ring (2 in Figure 5b and c) and then pressed together with this ring flush into the spin coating holder (3 in Figure 5b and c) in order to ensure a firm fit. Design principles and further details concerning the spin coating holder are provided in chapter 3.4. The spin coating holder (3 in Figure 5b and c) was sealed from the back so that it can be fastened in the spin coater by applying vacuum. After the spin coating process the coated Ti cylinder can be pressed out of the holder applying force to the back of the Ti cylinder.

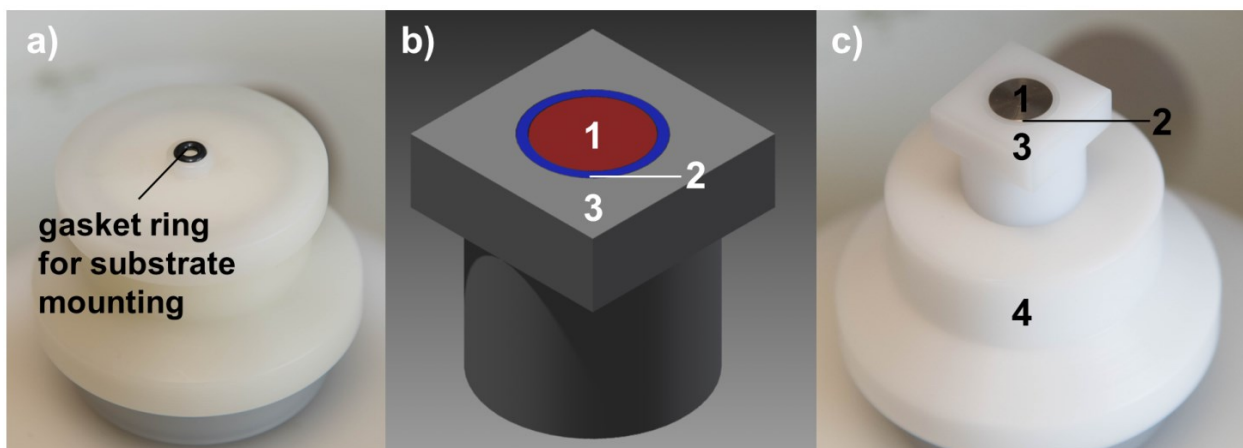


Figure 5: *Spin-coating sample holders. a): Standard spin coating sample holder on which the substrate is placed on top and adhered by applying vacuum from the back. b) and c): Drawing and photograph of the custom-made spin coating sample holder with 1: Ti cylinder, 2: tapered ring, 3: spin coating sample holder, 4: adapter to mount the spin-coating sample holder in the spin coater.*

2.1.2.1 Spin coating protocol

For the common spin coating process, the coating-solution was applied onto the rotating substrate at 200 revolutions per minute (rpm) with an amount sufficient to ensure full coverage of the substrate (commonly $\sim 40 \mu\text{l}$). Thereafter, the rotational velocity was increased to 2000 rpm with 200 revolutions s^{-2} and dwelled at this velocity for 45 s to finish the spin-coating process.

2.1.2.2 Preparation of Ir oxide films

For the synthesis of Ir oxide films an Ir acetate coating solution was prepared dissolving Ir acetate (80 g l^{-1} , $\sim 0.2 \text{ mol}_{\text{Ir}} \text{ l}^{-1}$, Chempur, 99.95%) in ethanol (abs., AnalaR Normapur) by ultrasonication. Subsequently, this solution was filtrated through a syringe filter (Nylon, $0.2 \mu\text{m}$) to remove possible undissolved traces. After the Ir acetate precursors films had been deposited onto the substrate by spin coating (see 2.1.2.1), the coated substrates were calcined in a pre-heated Muffel furnace (Carbolite) at 450°C for 15 min in air. To determine the loading, the Ir acetate films were dissolved in water after the spin-coating process was finished. The amount of dissolved Ir was determined by inductively coupled plasma atomic emission spectroscopy (ICP-OES).

2.1.2.3 Preparation of Ir-Ni mixed oxide films

For the synthesis of Ir-Ni mixed oxide films an Ir acetate and a Ni acetate coating solution were prepared dissolving Ir acetate (80 g l^{-1} , $\sim 0.2 \text{ mol}_{\text{Ir}} \text{ l}^{-1}$, Chempur, 99.95%) or, respectively, Ni acetate (105 g l^{-1} , $0.42 \text{ mol}_{\text{Ni}} \text{ l}^{-1}$, Sigma-Aldrich, 99.998%) in ethanol (abs., AnalaR Normapur) by ultrasonication. Subsequently, these solutions were filtrated through a syringe filter (Nylon, $0.2 \mu\text{m}$) to remove possible undissolved traces. These solutions were mixed in volumetric ratios such as to obtain coating solution with the desired Ir-Ni molar ratios. Pure oxide reference samples were synthesized from the pure solutions. After the acetate precursor film had been deposited by spin coating according to the described protocol (see section 2.1.2.1) the samples were calcined in a preheated Muffel furnace at 450°C for 15 min in air. To determine the Ir and Ni loading, the acetate films were dissolved in water after the spin-coating process was finished. The amount of dissolved Ni and Ir was determined by ICP-OES. The Ir to Ni ratio was determined by ICP-OES analysis of the coating solution to obtain a higher accuracy, achieved by

higher measured concentrations. Ir-Ni mixed oxide catalysts will be referred to as x%Ni-MO (MO for Ir-Ni mixed oxide). Thereby, x specifies the Ni content (at%) ($x=c(\text{Ni})/(c(\text{Ni})+c(\text{Ir}))$) in the as-prepared mixed oxide. To point out whether as prepared or OER tested samples were actually measured, as prepared samples will be referred to as x%Ni-MO-ap whereas the OER tested samples will be referred to as x%Ni-MO-OER. Similarly, all Ni contents used to specify a certain mixed oxide sample are provided in at% and refer to the as-prepared state.

2.1.2.4 Preparation of Ru oxide films

For the synthesis of Ru oxide films Ru acetate (Chempur) was initially dissolved in ethanol (abs., AnalaR Normapur) by ultrasonication, separated from insoluble residues by syringe filtering (Nylon, 0.2 μm) and then freeze dried. The resulting black powder was again dissolved in ethanol (abs., AnalaR Normapur) to yield a concentration of 50 g l^{-1} and then filtrated through a syringe filter (Nylon, 0.2 μm) to remove insoluble traces. After the substrates were coated with this solution according to the described spin-coating protocol (see chapter 2.1.2.1), the coated substrates were calcined under synthetic air in a slide-able tube furnace (MTI cooperation), which was preheated to 250°C at an empty part of the tube and then moved to the sample position to achieve a fast heating. After 4 hours of calcination the furnace was cooled and the samples were subsequently tempered under argon (heating rate: 5 K min^{-1} , 400°C, dwell time: 12 h).

2.2 Preparation of silica coated gold nanoparticles and their deposition on the Ru oxide model film

2.2.1 Preparation of silica coated gold nanoparticles ($\text{Au}@\text{SiO}_x$)

Silica coated gold nanoparticles were synthesized according to a previously described procedure,⁶⁵ which was slightly modified and optimized. In short, gold nanoparticles were obtained adding 1.750 ml of a 1 wt% trisodium citrate solution (ACS grade, Sigma-Aldrich) to 250 ml of a boiling 0.3 mM solution of tetrachloroauric acid (ACS grade, Sigma-Aldrich) in ultrapure water (18 M Ω cm at room temperature). After the addition of sodium citrate the reaction mixture was boiled under reflux for 40 min to finish the reaction.

To obtain the silica coating, 30 ml of the prepared gold nanoparticle suspension (cooled to room temperature) were transferred to a round-bottom flask and the pH value was adjusted to 4.5-5.0 with 0.1 M potassium hydroxide solution. Subsequently, 900 μl of a 1 mM (3-Aminopropyl)trimethoxysilane solution in water (reagent grade, Sigma-Aldrich) were added slowly under vigorous stirring at room temperature. After the stirring was continued for 15 min, 3.20 ml of a 0.8% sodium silicate solution were added. During this process the pH of the solution rises sharply. Then the pH value was adjusted to 10 using 0.1 M sulphuric acid. Accordingly, the reaction mixture was heated to 90°C for 30 min and then rapidly cooled to room temperature. The particles were separated from the reaction mixture by centrifugation (5500 rpm), redispersed in water and again separated by centrifugation to obtain a concentrated particle suspension.

2.2.2 Deposition of Au@SiO_x on Ru oxide films

For the deposition of silica-coated gold particles a Teflon ring, manufactured according to ⁶⁶ and depicted in Figure 6a, was pressed onto the Ru oxide film (as shown in Figure 6b). In this configuration the Teflon coating ring creates a volume element in which the walls have a 45° angle to the surface normal of the Ru oxide film. Then, 7 μl of the concentrated Au@SiO_x suspension were pipetted into the Teflon ring onto the Ru oxide film. Subsequently, the water is evaporated in oil pump vacuum to yield a particle film on top of the Ru oxide film. Thereafter the Teflon coating ring was removed.

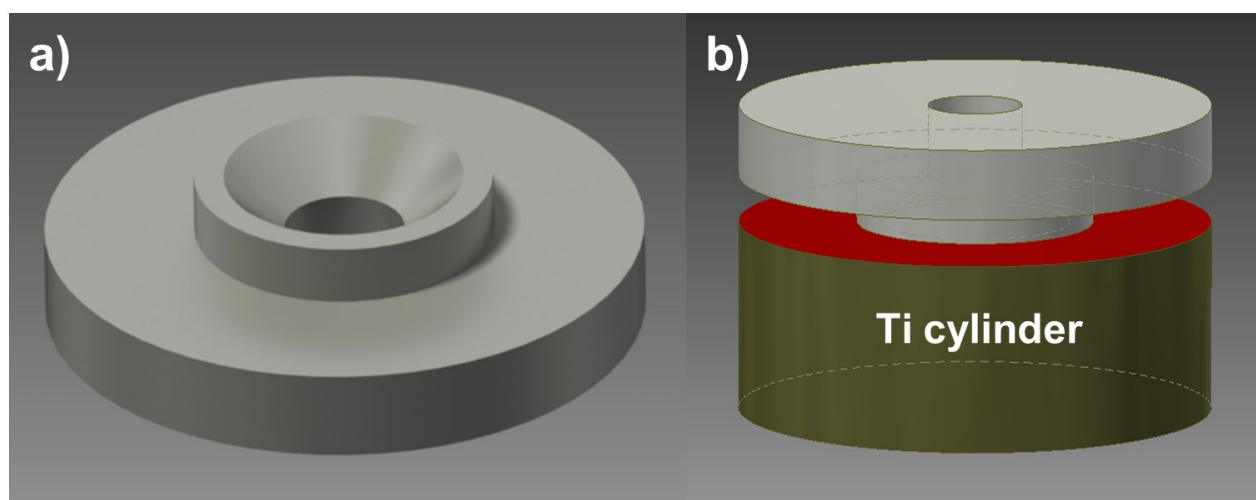


Figure 6: *a: Teflon coating ring used for the deposition of Au@SiO_x on Ru oxide films. b: Teflon coating ring positioned on the Ru oxide film coated surface of a Ti cylinder.*

2.3 Physicochemical characterization

2.3.1 Inductively coupled plasma atomic emission spectroscopy (ICP-OES)

ICP-OES was measured with a Varian 715-ES ICP.

2.3.2 Scanning electron microscopy (SEM)

SEM images were acquired in secondary electron mode with a Jeol 7401F field emission scanning electron microscope operated at 10 kV (if not stated differently). If necessary, the images were filtered to remove periodic distortions caused by oscillations of the microscope. Therefore, the concerned images were Fourier transformed, the corresponding frequency range was deleted and the images were transformed back using the software ImageJ. Additionally, the noise filters implemented in ImageJ were used.

2.3.3 Raman spectroscopy

Raman spectra (ex-situ) were measured in back scattering geometry using a confocal spectrometer (LabRam, Horiba) as described in section 2.4.3.1. Here the 647-nm line of a Kr⁺ ion laser (1 mW) was focused onto the sample. The accumulation time of the spectra was 10 times 60s.

2.3.4 Thermo-gravimetry coupled with mass spectroscopy (TG-MS)

TG-MS was measured with a heating rate of 5 K min⁻¹ in a synthetic air flux using a corundum crucible in a thermo-balance (TG 209 F3, Netzsch). Gaseous products were detected by a quadrupol mass spectrometer (Pfeiffer).

2.3.5 Energy dispersive X-ray spectroscopy (EDX)

EDX (including line scans) was measured using the Jeol 7401F described before, which is equipped with an EDX detector (Quantax 400, Bruker). The actual acceleration voltage was adjusted according to the elements present and will be provided together with the measurements.

2.3.6 Transmission electron microscopy (TEM) and selected area electron diffraction (SAED)

TEM and SAED were measured with 200 kV in a FEI TECNAI G² 20 S-TWIN equipped with LaB₆ cathode and GATAN MS794 P CCD camera. The samples were transferred to carbon coated copper grids for the measurements. Therefore, oxide films were scraped off the substrate with a scalpel. Considering SAED measurements, the samples were carefully checked for beam sensitivity. The SAED images were integrated using the software Fit2D and transferred into the 2 θ scale (Cu K- α). The background was fitted with a double exponential decay function and then subtracted.

2.3.7 Ir oxide cross-section by Scanning transmission electron microscopy (STEM) and TEM

S/TEM cross-section investigations were performed with a Cs corrected FEI Titan 80-300 equipped with an EDX detector (EDAX) and high angle annular dark field (HAADF) detector. The sample was prepared in cross section along the <110> zone axis of the Si wafer. Therefore, two stripes were cut out of the wafer by a diamond wire saw. These two pieces were glued layer against layer and embedded by epoxy inside a Ti-grid. After the sample was ground to a certain thickness, a dimple was polished to each side of the sample. As a final step the sample was ion-milled in a Fischione Ionmill Model 1010 under low incident angles and decreasing acceleration voltages, starting at 5 kV and 10° until finally 1 kV and 8°. Prior to measurements the sample was treated with Ar plasma for 30 s to remove severe contaminations.

2.3.8 X-ray diffraction (XRD)

XRD profiles were measured in grazing incidence at 1° with Goebel mirror, Cu K α source, a 0.23° secondary soller and scintillation counter as detector in a Bruker D8 Advance diffractometer (Bruker AXS). Data were collected with an increment of 0.05° and a measuring time of 40 s per step.

Qualitative phase analysis was performed comparing the measured diffractograms with reference patterns. In case different phases with overlapping diffraction patterns were present in a sample, a Rietveld refinement was used to identify the actually present phases. Rietveld refinement was performed using the software TOPAS (Bruker AXS),

which was designed for powder samples. Thus, in case of films, where the different phases are possibly located in different layers at different depth, the evaluated concentrations of the different phases might not be exact, as the top layers are expected to lower the intensity of the incident beam that can interact with the lower layers. Moreover, the scattered radiation of the lower layers has to pass through the upper layers prior to detection whereby a loss of intensity is expected. Hence, the results from the quantification of the different phases appear not to be reliable and are not provided here for this reason.

2.3.9 X-ray absorption spectroscopy (XAS)

O K edge absorption spectra recorded in the total electron yield mode were collected at the ISSS beamline of the synchrotron radiation facility BESSY of the Helmholtz-Zentrum Berlin (HZB).

2.3.10 X-ray photoelectron spectroscopy (XPS)

2.3.10.1 *Ir-Ni mixed oxides*

XPS measurements were performed using a K-Alpha XPS spectrometer (ThermoFisher Scientific, East Grinstead, UK). All samples were analyzed using a microfocused, monochromated Al K α X-ray source (30-400 μ m spot size). The K-Alpha charge compensation system was employed during analysis, using electrons of 8 eV energy and low-energy argon ions to prevent any localized charge build-up. The analyzer transmission function, Scofield sensitivity factors,⁶⁷ and effective attenuation lengths (EALs) for photoelectrons were applied for quantification. EALs were calculated using the standard TPP-2M formalism.⁶⁸ The spectrometer was calibrated using the well-known photoelectron peaks of metallic Cu, Ag, and Au. Since no charging is expected for Ir-Ni mixed oxides no correction of the binding energy was applied.

2.3.10.2 *All other samples*

X-ray photoelectron spectroscopy was measured at the ISSS beamline of the synchrotron facility BESSY II of the Helmholtz-Zentrum Berlin. A detailed description of the setup can be found elsewhere.⁶⁹ Samples were mounted onto a sapphire sample

holder and introduced into the spectrometer. XPS experiments were carried out at room temperature in ultra-high vacuum (UHV).

2.3.11 Temperature programmed reduction (TPR)

TPR was measured in a TPDRO 1100 (Thermo Fisher Scientific) from 30 to 600°C with a heating rate of 10 K min⁻¹ under 20 ml min⁻¹ H₂/Ar (4.05% H₂ in Ar, Air Liquide, purity 5N). Prior to TPR, the samples were dried in the same reactor at 125°C for 1 h under 20 ml min⁻¹ Ar (Air Liquide, purity 5N). The temperature inside the reactor at the sample position was measured by a type-K thermocouple sealed in a quartz capillary.

2.4 Electrochemistry and related in-situ methods

2.4.1 Electrochemical measurements (OER protocol): OER activity and surface characterization via cyclic voltammetry

The electrochemical measurements were performed at room temperature in a rotating disk electrode (RDE) setup equipped with a three compartment electrochemical glass cell including a Luggin capillary, rotator (Pine research instrumentation) and a SP-200 potentiostat (BioLogic, France). A saturated mercury/mercury sulfate electrode was used as reference electrode. The reference electrode was calibrated against a reversible hydrogen electrode in the same electrolyte. All potentials provided in this work were converted and referred to the reversible hydrogen electrode if not stated differently. The electrolyte, 0.1 M HClO₄, was prepared by dilution of 70% perchloric acid (Sigma-Aldrich, 99.999%) with ultrapure water (18 MΩ cm at room temperature).

Electrochemical measurements were performed with coated Ti cylinders. Prior to the measurement, the back of the Ti cylinders was grinded to remove Ti oxide layers possibly formed during calcination and, hence, ensure a proper electrical contact. Afterwards, the Ti cylinders were mounted into a custom-made RDE sample holder as depicted in Figure 7. To mount the Ti cylinder, it was first pressed into the tapered Teflon ring (3). Accordingly, this assembly was inserted into the RDE sample holder (2) manufactured from polyether ether ketone (PEEK). Then, the Teflon ring was pressed further into the RDE sample holder (2) by tightening the screw nut (1) to ensure a firm fit. The screw nut exerts force exclusively on the Teflon ring so that no force has to be exerted on the sample. Subsequently, a contact pin (4) was screwed into the back of the

RDE sample holder to provide the electrical contact. The complete sample holder was then connected to a standard RDE shaft (Pine research instrumentation) and assembled into the RDE setup (Pine research instrumentation).

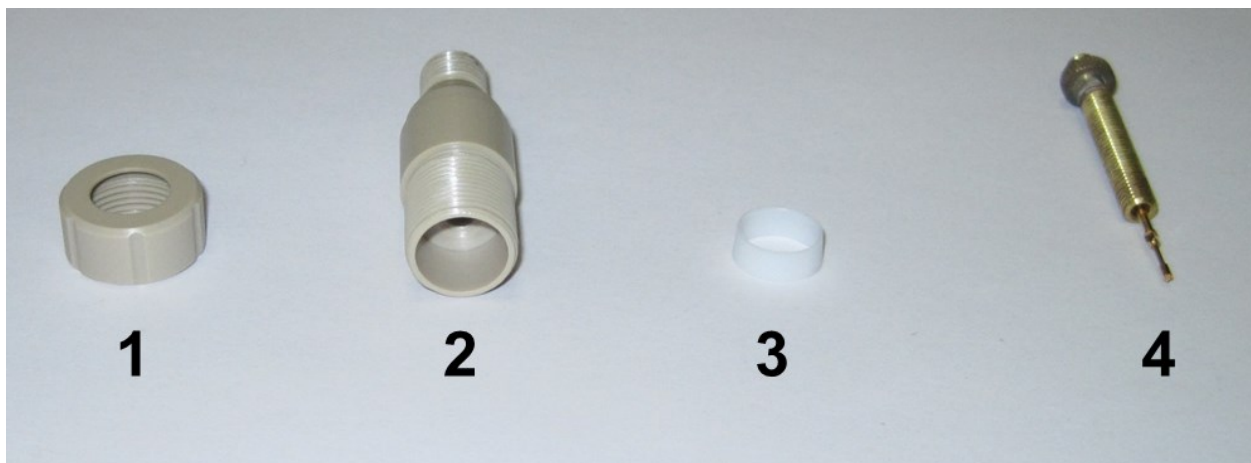


Figure 7: *Custom-made RDE sample holder and accessories. 1: screw nut, 2: RDE sample holder, 3: tapered Teflon ring, 4: contact pin*

The sequence of the electrochemical measurements is visualized in Figure 8 and is described in the following. The samples (mounted in the described RDE sample holder) were immersed at $1.200 V_{\text{RHE}}$ into the nitrogen-degassed (15 min.) electrolyte, followed by three polarization curves into the OER potential region. The first and third polarization curves were performed with 6 mV s^{-1} between $1.200 V_{\text{RHE}}$ and an upper potential limit E_{lim} . Here, E_{lim} represents the potential required to reach a geometric current density of 15 mA cm^{-2} in the respective scan and is thus a function of the catalyst applied. In contrast to that, the second scan was measured quasi-stationary with 8 steps, a potential step size of 20 mV and a dwelling time of 5 minutes at every applied potential. The potential of the first step was determined by an anodic potential scan with 6 mV s^{-1} which was performed from $1.200 V_{\text{RHE}}$ up to a potential where a current density of 0.3 mA cm^{-2} was reached. The potential at which 0.3 mA cm^{-2} was reached was then used for the first potential step. After every potential step, the ohmic drop was determined by impedance spectroscopy, since the ohmic drop might be altered by conductivity changes of the electrode or by O_2 bubble formation. This quasi stationary OER scan will be referred to as OER Scan I. Subsequently, after a second degassing, cyclic voltammetry was measured between 0.400 and $1.400 V_{\text{RHE}}$ consecutively with the following scan rates: 500, 200, 100, 50 and 20 mV s^{-1} . Thereby, 100 cycles were

performed at 500 mV s^{-1} to ensure a constant voltammogram, followed by 3 cycles at each following scan rate. Then, the investigated voltage range was extended to reach from 0.050 to $1.400 \text{ V}_{\text{RHE}}$ applying the same procedure as before. Thereafter, again three OER scans were performed similar to the before. Hereby, the quasi stationary scan is referred to as OER scan II. The OER measurements were performed with 1600 rpm RDE rotation speed while cyclic voltammetry was measured with 0 rpm.

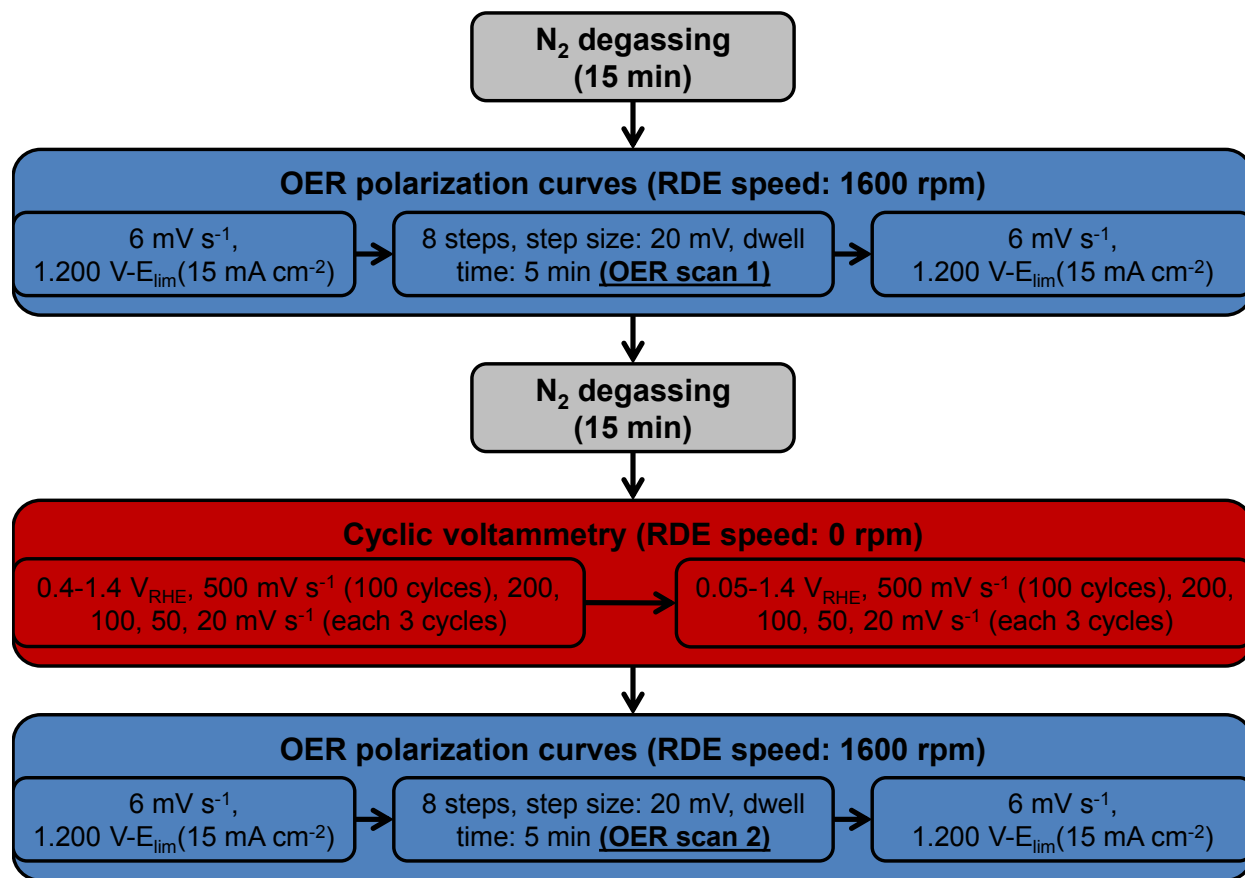


Figure 8: Graphical representation of the sequence of electrochemical measurements performed to address the electrocatalytic OER activity and characterize the surface state of the catalysts. The whole sequence will be referred to as OER protocol in the following.

2.4.2 Potential resolved inductively coupled plasma mass spectrometry (PR-ICP-MS)

Time- and potential-resolved analysis of dissolved metal ions was carried out with a scanning flow cell (SFC) based setup.^{14,25} Ir-Ni mixed oxide films that previously

underwent the OER (referred to as MO-OER) and as prepared pure Ir oxide films (IrOF) served as working electrodes. An Ag/AgCl reference electrode and a graphite rod counter electrode were applied. The potential was controlled by a potentiostat (Reference 600, Gamry). During the measurement the SFC was pressed onto the working electrode and the electrolyte (0.1 M HClO₄) was pumped with a constant flow rate of ca. 180 μL min⁻¹ through the SFC. Downstream of the SFC, the electrolyte was mixed with an internal standard in a Y-connector (mixing ratio 1:1) and then introduced into an ICP-MS (NexION 300X, Perkin Elmer).

2.4.3 In-situ Raman spectroscopy and related electrochemical measurements

2.4.3.1 Raman Spectroscopic measurements

Raman spectra were measured in back scattering geometry using a confocal spectrometer (Jobin Yvon, LabRam 800 HR). The 647-nm line of a Kr⁺ ion laser (1 mW) was focused onto the sample using a Zeiss 40x water immersion objective with high numerical aperture. The accumulation time of the spectra was 3 times 30s. During the measurement the sample was continuously moved 1 mm back and forth on a position-controlled x-y-table, whereby 1 cycle took 30s. The in-situ cell is described in the text. The electrode potential was controlled using a SP-200 potentiostat (BioLogic, France).

2.4.3.2 Electrolytes for in-situ Raman spectroscopic measurements

For the identification of Raman signals the measurements were performed in isotopically labelled electrolytes. 0.1 M HCl¹⁶O₄/H₂¹⁸O was prepared diluting 70% HCl¹⁶O₄ (Sigma-Aldrich, 99.999%) with H₂¹⁸O (Campro Scientific, 97 at% ¹⁸O). 0.1 M DCl¹⁶O₄/D₂¹⁶O was prepared diluting 68% DCl¹⁶O₄ in D₂¹⁶O (Sigma-Aldrich, 97 at% D) with D₂¹⁶O (Sigma-Aldrich, 99.9 at% D). 0.1 M HCl¹⁶O₄/H₂¹⁶O was prepared as described in section 2.4.1.

2.4.3.3 Electrochemical Characterization

Cyclic voltammetry measurements of coated Ti samples were performed in the setup described in section 2.4.1.

The coverage of the silica coating of Au@SiO_x was investigated by cyclic voltammetry (CV) detecting the amount of uncoated gold. Therefore, 5 μl of the Au@SiO_x suspension

(see section 2.2.1) were pipetted onto a screen printed carbon electrode (SPCE) (DropSens, working electrode: carbon (4 mm diameter), counter electrode: carbon, reference electrode field: silver (not used)) and dried in oil pump vacuum. As-prepared uncoated gold nanoparticles (AuNP) were centrifuged to obtain a suspension with a concentration approximately similar to that of the silica-coated gold NP. 5 μl of this suspension were deposited on a SPCE as reference. Cyclic voltammetry was measured with 100 mV s^{-1} from 0.5 to 1.65 V_{RHE} in 0.05 H_2SO_4 in a beaker. A saturated calomel electrode was used as reference whereas the counter electrode field on the SPCE was used as counter electrode. To determine the gold loading on the SPCEs, the particles were dissolved in aqua regia after the CV measurement and the gold concentration in this solution was determined by ICP-OES.

3 Choice of model catalyst and catalyst synthesis development

In the following chapter first the requirements of a model catalyst appropriate for the fundamental investigation of the OER on Ir and Ru based catalysts, as described in section 1.6, are pointed out. Based on these requirements, a model catalyst is selected and, then, the synthesis development of the selected model catalyst is described.

3.1 Choice of the model catalyst

A fundamental study of thermally prepared Ir and Ru oxide based PEM OER catalysts, as described in section 1.6, requires the choice of an adequate model system. According to section 1.6, the following requirements are imposed for a model catalyst. First, the model catalyst should allow for purely microkinetic studies minimizing mass transport effects like reactant depletion or product accumulation at the catalysts surface so that they can be neglected. Thereby, the desired intrinsic chemical-kinetic properties of the catalyst can be studied exclusively. Moreover, the model catalyst should mimic commonly applied OER catalysts, which are described in section 1.2. Furthermore, the model catalyst should allow for a direct meaningful correlation of insights from surface confined analytical techniques like XPS and SERS with the observed catalytic currents. Beside these requirements, the model catalyst should facilitate the study of catalyst substrate interactions, which have not been sufficiently clarified so far.

All mentioned criteria are fulfilled by extended homogenous oxide thin-films with well-defined nanometer sized thickness on Ti substrates as model system, as explained in the following. Surface sensitive analytical methods probe a significant fraction of such a thin-film allowing for a meaningful correlation of the obtained surface sensitive data with the results from the electrocatalytic measurements, to which the whole film contributes. Moreover, the study of catalyst-substrate interactions is straightforward applying the thin-film model system, since the catalyst substrate junction contributes a comparably large fraction to the catalytically active system, maximizing the observable effect.

Thin-films ensure short paths for the comparably slow diffusion based mass transport of reactants and products inside the film to or, respectively, away from the active sites. Thus, short paths allow a fast mass transport minimizing the effects of reactant depletion or product accumulation. Moreover, if fast mass transport is ensured at the liquid catalyst-film interface toward the thin-film catalyst and away from it by the RDE technique, mass transport effects possibly convoluting the catalytic process are reduced to a minimum. Thereby, the RDE ensures a fast convective mass transport keeping the Nernst diffusion layer δ thin.⁷⁰ In the Nernst diffusion layer mass transport can solely be conducted by diffusion.⁷⁰ As a result of the well-defined and well-known flow regime present in a RDE, δ can be calculated according to equation(21).⁷⁰ Herein, ω_a denotes the angular velocity, ν the kinematic viscosity and D the diffusion coefficient.

$$\delta = 1.61 \omega_a^{-\frac{1}{2}} \nu^{\frac{1}{6}} D^{\frac{1}{3}} \quad (21)$$

Based on δ , the concentration at the electrodes surface can be calculated according to equation (22) which includes the assumption that the concentration gradient from the electrodes surface to the electrolyte bulk is constant.⁷⁰ Herein, c represents the bulk concentration and c_0 the concentration at the electrodes surface.

$$j = n F D \frac{c - c_0}{\delta} = n F D \frac{\Delta c}{\delta} \quad (22)$$

With the diffusion coefficients listed in Table 1, values for δ were calculated for a RDE rotational velocity of 1600 rpm (applied for all RDE OER measurements in the present work) and provided in Table 1. Due to the rather large values obtained for δ relative to the catalyst film thickness, diffusion processes inside the electrolyte filled porous thin catalyst films (thickness ~ 50 nm) appear to be negligible, although the actual diffusion path might be much longer than the film-thickness due to a certain tortuosity. Based on the values obtained for δ , the difference between bulk and surface concentration (Δc) was calculated at a current density of 15 mA cm^{-2} according to equation (22). The calculations were solely performed for the products H^+ and O_2 , since the only reactant water is the main component of the electrolyte which makes transport limitations highly improbable.

Table 1: Diffusion coefficients^{51,71} (D), Nernst Diffusion layer thicknesses (δ , according to equation (21)) and bulk-surface concentration differences (Δc , according to equation (22)) calculated for H^+ and O_2 at 25°C. The calculation was performed for a current density of 15 mA cm⁻² and a RDE rotational velocity of 1600 rpm.

component	$D / \text{m}^2 \text{s}^{-1}$	δ / m	$\Delta c / \text{mol l}^{-1}$
H^+	$9.31 \cdot 10^{-9}$	$2.57 \cdot 10^{-5}$	$4.29 \cdot 10^{-3}$
O_2	$2.42 \cdot 10^{-9}$	$1.64 \cdot 10^{-5}$	$2.63 \cdot 10^{-3}$

The concentration differences provided in Table 1 are small. Thus, mass transport effects appear to be negligible, at least with respect to H^+ . Considering O_2 , the concentration difference is larger than the maximal solubility of $\sim 1.3 \cdot 10^{-3} \text{ mol l}^{-1}$ (at 25°C)⁵¹. Thus, even if no O_2 is assumed to be dissolved in the bulk electrolyte during the measurement (measurement was performed with N_2 stream above the electrolyte) gas bubbles are expected to form at the considered current density of 15 mA cm⁻² and can form under the mentioned assumptions already from $\sim 7 \text{ mA cm}^{-2}$ on. However, gas bubbles are also expected to be efficiently transported away from an RDE due to the present flow regime although the transport cannot be calculated according to the presented equations (21) and (22). Thus, up to the considered current density of 15 mA cm⁻², mass transport effects, interfering with the catalytic process, appear to be negligible.

3.2 Substrate

Studies focusing on Ir and/or Ru oxide containing catalysts mainly apply Ti as substrate^{36,39,72,73} due to its inertness and corrosion resistance under harsh acidic conditions, as described in section 1.2. Although Ti itself is thermodynamically unstable under the PEM OER conditions, it is covered efficiently by a thin closed passivating oxide layer.¹¹ Therefore, Ti is additionally used as material for current collectors in PEM electrolyzer units.⁶ Due to its beneficial material properties and its use in PEM electrolyzers, Ti was used as substrate material for Ir and Ru oxide based thin-films in the present work.

If a homogenous thin-film coating is desired on a Ti substrate, high demands are requested concerning the surface quality of the substrate, especially with regard to the roughness. If the surface roughness becomes too high, the thin-film cannot cover the substrate completely or, alternatively, the film thickness has to vary largely to fill all recesses. Therefore, the surface roughness of the substrate has to be reduced to a minimum. To generate a very low surface roughness the Ti cylinders were ground and polished successively to a mirror like surface finish in a half-automatic polishing machine (see section 2.1.1.3). Therefore, a final suspension with a grain-size of 20 nm was used which is expected to result in a surface roughness ≤ 20 nm. Since the substrate has to be compatible with a RDE setup, Ti was commonly applied in form of cylinders. Alternatively, Ti coated Si Wafers (TS) were applied as model substrate, which show a very low surface roughness and, thus, do not need to be polished. The TS substrates are well suited for cross-section microscopy and gas-phase analytical methods like TPR. Using TS, the interaction of the catalyst film with the Ti substrate can be easily studied in cross-section. After breaking the substrate into two pieces, microscopy can be performed on the breaking edge. Moreover, TSs facilitate the application of comparably large film areas into gas phase reactors used for analytical techniques like TPR which have comparably high detection limits. In case the oxide film had to be studied without the presence of a Ti-catalyst-interface or a coating procedure had to be developed, Si wafer pieces were used as substrates.

3.3 Choice of the precursor

Commonly, noble metal oxide films used as OER catalysts are prepared by thermal decomposition of chloride based precursor salts in air which have previously been coated onto the substrate,^{39,72,74} as described in section 1.2. Considering this approach, significant amounts of chloride residues remain in the oxide,^{23,75} rendering chloride precursors unsuitable for the desired synthesis of high-purity thin-film model oxide catalysts. Moreover, Ru and Ir chloride decompose in air at comparably high temperatures as demonstrated by TG-MS measurements depicted in Figure 9. The first mass loss of both chloride precursors below 300°C is related to the loss of water and not to precursor decomposition, since solely an increase in $m/z=18$ was observable. Chlorine ($m/z=35$) was detectable during the second mass loss indicating that this is related to the decomposition of the chloride precursor. Considering RuCl_3 , the decomposition appeared at about 375°C. IrCl_3 was decomposed at an even higher temperature of ~625°C. These high decomposition temperatures restrict the applicable temperature range accessible for the synthesis.

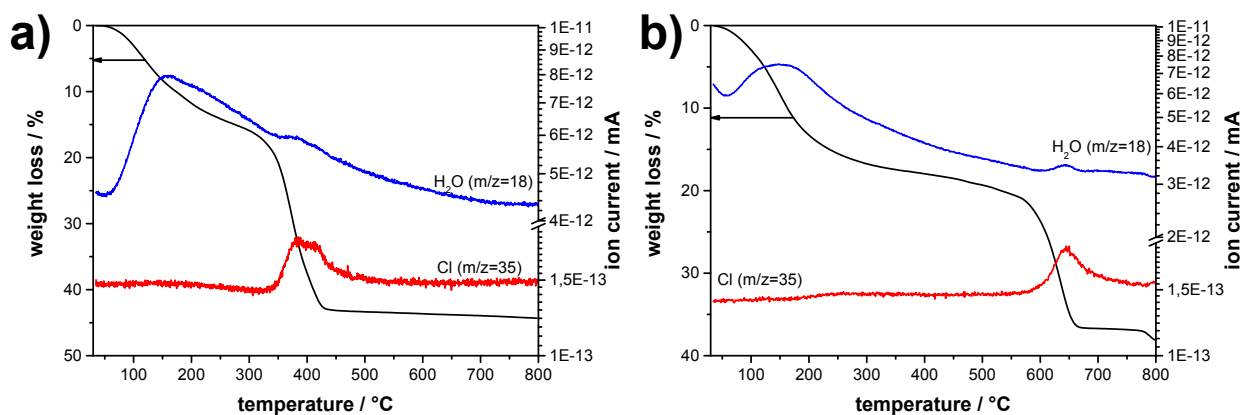


Figure 9: TG-MS measurements of Ru (a) and Ir chloride (b) in synthetic air with a heating rate of 5 K min^{-1} .

In comparison to the chloride based precursors Ru and Ir acetate decompose in air already below 250°C, and thus at much lower temperatures (see Figure 10). Decomposition products of the acetate precursor, mainly CO_2 ($m/z=44$) and H_2O ($m/z=18$) due to acetate combustion, were detectable during the main mass loss located at approx. 250°C. The mass loss visible at lower temperatures is related to a drying process, since only water ($m/z=18$) was detectable. Considering the much lower

decomposition temperature and the absence of chloride, the acetate precursors allow for synthesizing chloride free Ru and Ir oxides over a wide temperature range via the thermal decomposition method. Due to these advantages, acetate precursors are used in the present work for the preparation of Ir and Ru oxide films.

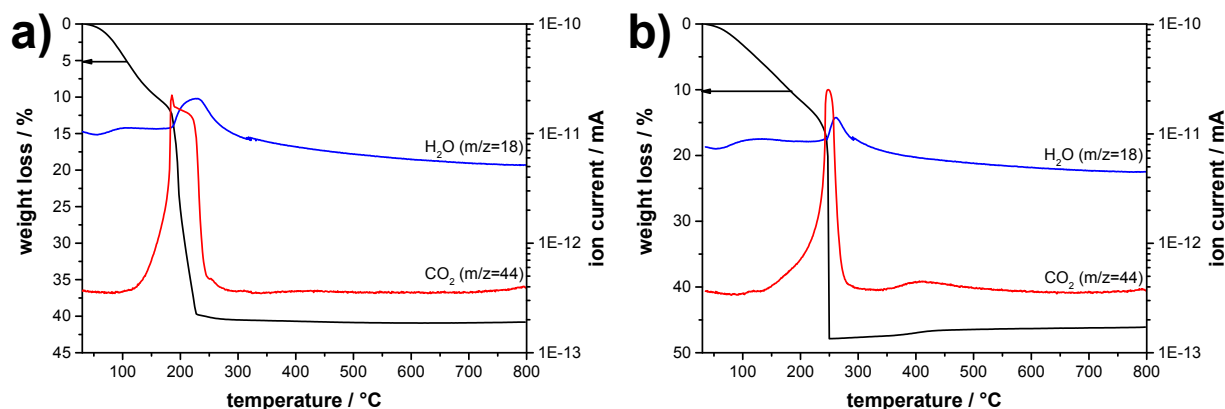


Figure 10: *TG-MS measurements of Ru (a) and Ir acetate (b) in synthetic air with a heating rate of 5 K min⁻¹.*

3.4 Deposition of thin-films

To produce thin-film oxide layers via thermal precursor decomposition, a thin acetate precursor film was first deposited onto the substrate and then thermally converted into the oxide. The thin acetate precursor film was deposited using the spin-coating technique. Here, spin-coating was applied due to its ability to prepare homogenous smooth thin-films with precisely adjustable thickness, as will be shown below.

Considering the spin-coating process, the acetate precursor is initially dissolved in ethanol. This coating solution is then applied onto the spinning substrate at low rotational speed in order to distribute the coating solution on the substrate. Subsequently, the rotational velocity is quickly increased to the desired value causing a radial flow of the coating solution due to the arising centrifugal force. Thereby, the coating solution gets spun off the substrate to a large extent until the centrifugal and shear force become almost similar so that the radial flow becomes slow. The radial flow of the coating solution is superimposed by solvent evaporation. In the beginning of the spin-coating process the radial flow dominates, and solvent evaporation can be neglected.⁷⁶ However, when the liquid film becomes thinner the shear force is increasing

until at a certain liquid film height h_1 shear force and centrifugal are almost similar.⁷⁶ Now the velocity with which the coating solution gets spun off becomes very small so that it can be neglected.⁷⁶ When h_1 is reached, the remaining solvent gets basically completely evaporated and not spun off anymore leaving the previously dissolved precursor salt as thin homogenous film on the substrates surface.⁷⁶ The loading and thereby the film thickness can be determined by equation (23), which is based on the assumptions mentioned before.⁷⁶

$$m_L = c_{0,mass} \cdot h_1 = c_{0,mass} \cdot \sqrt[3]{\frac{3\eta\Phi}{2\rho\omega^2}} \quad (23)$$

In equation (23) $c_{0,mass}$ is the mass concentration of the coating solution, m_L is the mass loading (in $g\ m^{-2}$), η is the dynamic viscosity, ρ is the density of the coating solution, Φ is the evaporation rate and ω is the rotational velocity. Under the assumption that the mass transport from the solution-vapor-interface to the vapor phase is the rate determining step of solvent evaporation, the evaporation rate Φ in a spin-coating device is proportional to $\omega^{0.5}$.⁷⁶ Therefore, the mass loading m_L is supposed to be proportional to the concentration of the precursor solution and to $\omega^{-0.5}$. Since the film thickness is proportional to m_L for a given film density, the film thickness can be adjusted varying the concentration of the coating solution and/or the rotational velocity in the spin-coating process.

However, due to the assumptions and approximations necessary to obtain equation (23) deviations appear possible. Additionally, the evaporation rate of ethanol is unknown under the experimental conditions applied here. Therefore, the film thickness of the resulting oxide film was determined by cross-section microscopy of Ir oxide films for two different Ir precursor solution concentrations as function of the rotational velocity ω (see Figure 11a) to check the validity of equation (23) and determine the optimal parameters for the spin-coating process.

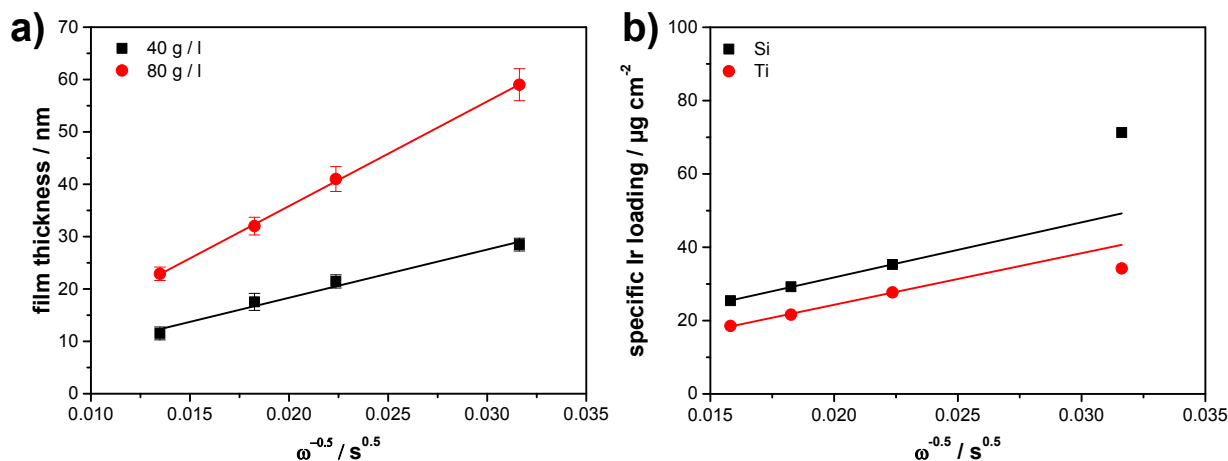


Figure 11: a) Spin-coating film thickness determined by SEM cross-section microscopy as function of $\omega^{-0.5}$ for two Ir acetate concentrations. b) Ir loading in the spin-coating process determined by ICP-OES as function of $\omega^{-0.5}$ for an Ir acetate concentration of 80 g l^{-1} . A Si wafer or a Ti cylinder (with custom made holder) was used as substrate.

As apparent from Figure 11a, the proportionalities of the film thickness to $\omega^{-0.5}$ and $C_{0, \text{mass}}$, which were expected from equation (23), could be confirmed. The proportionality of the film-thickness to $\omega^{-0.5}$ is directly apparent from Figure 11a. The proportionality to $C_{0, \text{mass}}$ can be ascertained comparing the slopes of the linear fits from Figure 11a. According to equation (23), the slope is expected to double if the concentration is doubled, which indeed was observed (slope: $921 \pm 79 \text{ nm s}^{-0.5}$ at 40 g l^{-1} and $1997 \pm 34 \text{ nm s}^{-0.5}$ at 80 g l^{-1}).

Figure 11b depicts the surface normalized Ir loading obtained by spin-coating with different rotational velocities on a Ti cylinder and a Si wafer piece. The Ir mass loading is expected to be directly proportional to the film thickness (shown in Figure 11a), if the density of the films is equal and the thickness is constant over the whole substrate. A linear relationship was obtained between rotational velocity and Ir mass loading at and above a rotational velocity of 2000 rpm. Interestingly, the Ir loading deviated significantly from the linear trend for the lowest ω (1000 rpm) for both the Si and the Ti substrate. However, the Ir oxide film thickness measured in the center region, omitting the substrate boundaries, still remains within the linear trend (see Figure 11a). This observation indicates that in case of $\omega=1000 \text{ rpm}$ the film thickness close to the substrate boundaries deviates significantly from the film thickness in the center region.

Thus, a rotational speed ≥ 2000 rpm should be used in order to avoid this pronounced boundary effect.

Based on the obtained data and the theoretical background, the film thickness can be adjusted to a value within the investigated range. Here, a film thickness of 50 nm appears as optimum for nano-crystalline oxide films because it ensures full substrate coverage even if small imperfections in the substrates surface are present. Moreover, this film thickness facilitates the utilization of differently sized nano-crystals as building block for the film, since the crystallite size has to be much smaller than the film thickness (for isotropic crystals), if an even and continuous film is desired. Furthermore, a film-thickness of ~ 50 nm can be realized at $\omega = 2000$ rpm with a coating solution concentration of 80 g l^{-1} Ir acetate, avoiding pronounced boundary effects apparent at lower ω .

In order to probe the homogeneity of the prepared films, the film thickness was measured for one sample ($\omega = 2000$ rpm, $c_{0, \text{mass}} = 80 \text{ g l}^{-1}$ Ir acetate) at 11 different randomly chosen spots by SEM cross-section microscopy, one of which is shown in Figure 12b. The measured average film thickness was 50.4 nm with a standard deviation of 1.4 nm. The small standard deviation demonstrates the uniformity of the film thickness. Moreover, the film quality with regard to coverage and homogeneity can be traced from the top-view image provided in Figure 12a and the micrographs provided in section 4.1.1.1.

Although a strong boundary effect was only observed for $\omega = 1000$ rpm a certain boundary effect at higher rotational velocities cannot be excluded and, thus, the boundary effect was evaluated in more detail. In order to provide a semi-quantitative measure of the boundary effect, EDX line scans were performed. The EDX line scans ranged from the sample holder over the substrate boundary to the homogenous center part of the substrate and were always performed perpendicular to the substrate boundary (see Figure 13). The boundary of the substrate was set to zero. To detect variations in film thickness an element present in the film (Ir) and an element present in the substrate (Si or Ti) were traced in the EDX line scans. Since only one component was used for spin-coating (Ir acetate) a variation of the Ir signal in the EDX line scan can

only be related to a variation in film thickness but not to a variation in film composition. Although the exact quantification of the film thickness from EDX line scans is not straight forward they provide an adequate semi-quantitative measure. If the Ir acetate film thickness increases the Ir signal increases while the substrate signal (Si or Ti) decreases and vice versa.

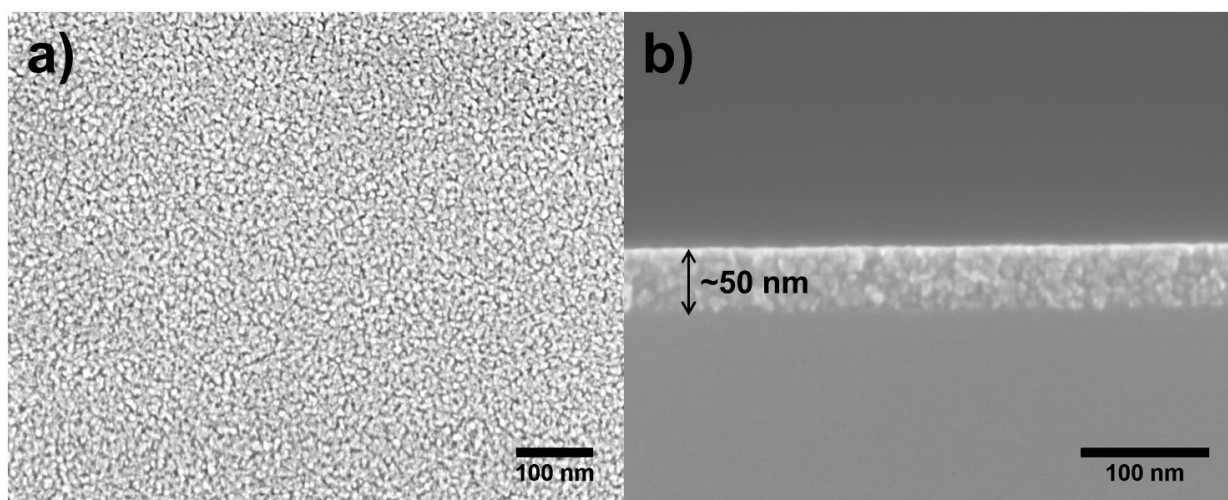


Figure 12: SEM top view (a) and cross-section (b) micrographs of an Ir oxide film deposited on a Si wafer. Spin-coating conditions: $\omega=2000$ rpm, $c_{0,mass}=80$ g l^{-1} Ir acetate.

The EDX line scan for an Ir acetate precursor film on a Si wafer substrate is depicted in Figure 13. Herein, the boundary effect can be seen to range over ~ 1200 μm . In this range the film thickness varies moderately but the film covers the substrate completely. Approximately 1000 μm away from the boundary a film thickness maximum appears, characterized by a maximum in the Ir signal and similarly by a minimum in the Si signal. Proceeding further towards the boundary, the film thickness gradually decreases approaching the value of the center part before it increases again in close vicinity to the substrate boundary. Since Si substrates were commonly applied with a minimum edge length of ~ 10 mm and only moderate variations in film-thickness were observed, the observed boundary effect was neglected for TPR measurements. Considering the film-thickness determination by SEM cross-section microscopy, the boundary effects were omitted, since these measurements were performed in the center region.

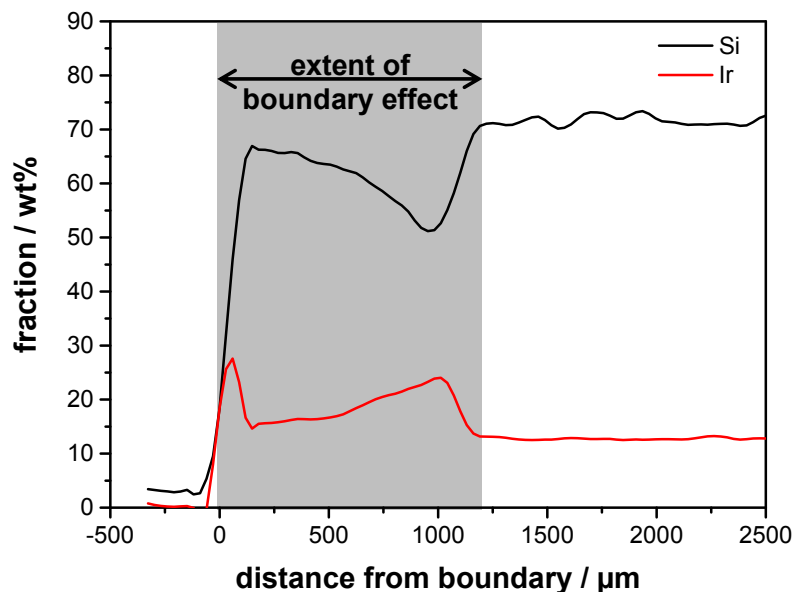


Figure 13: *EDX line scan of an Ir acetate film on a Si wafer. The scan was performed from the sample holder towards the coated substrate whereby the boundary was set to zero (data were smoothed). Film deposition conditions: $\omega=2000$ rpm and $c_{0,mass}=80$ g L⁻¹ Ir acetate.*

Although Si wafers or TS were applied for special applications, Ti cylinders were used as substrate for most measurements including electrochemistry. Figure 14a depicts an EDX line-scan for an Ir acetate film deposited on a Ti cylinder using the standard spin-coating holder (see section 2.1 and Figure 5a). Herein, a pronounced boundary effect was observed extending over ~ 1750 μm . In comparison with the Si wafer (see Figure 13) the variations in Ir and substrate signal are much stronger demonstrating a much stronger variation in film-thickness. Furthermore, the extent of the boundary effect was larger. Similar to the Si wafer the film is thicker in the boundary region, but the film-thickness varies strongly over the whole region whereas in case of the Si wafer the film-thickness was approaching the value of the homogenous center region after a maximum was obtained at ~ 1000 μm . In the boundary region of the Ti cylinder the film thickness shows three maxima at approximately 1500, 750 and 0 μm . In this case, magnitude and extent of the boundary effect appear too big to be neglected if well-defined thin-film model catalysts are desired.

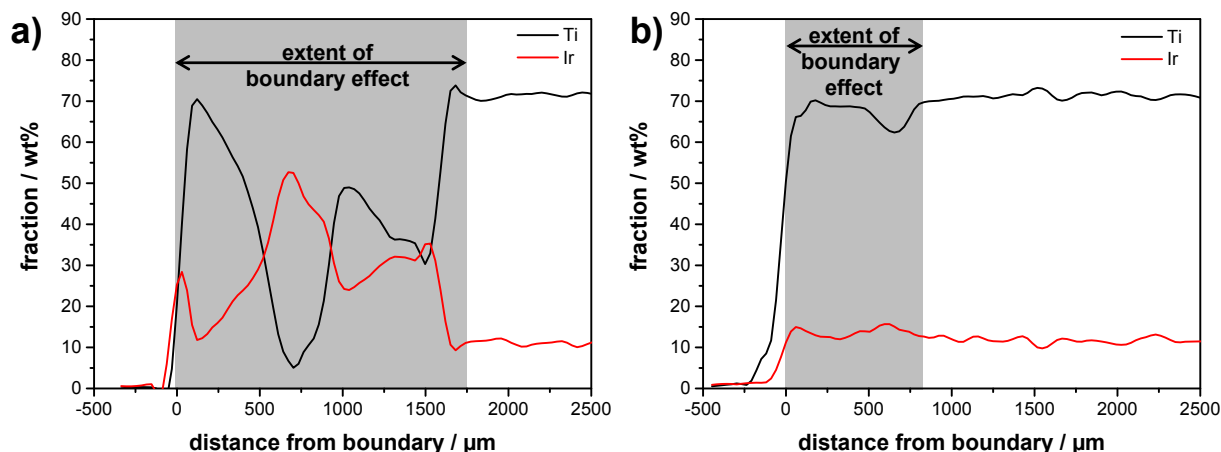


Figure 14: *EDX line scan for Ir acetate films on Ti cylinders. The standard spin-coating holder was used for a) while a custom made holder was used for b). The scans were performed from the sample holder towards the coated substrate whereby the boundary was set to zero (data were smoothed). Spin-coating conditions: $\omega=2000$ rpm and $c_{0,mass}=80$ g L⁻¹ Ir acetate.*

The observation of a much bigger boundary effect on a Ti cylinder compared to a rectangular Si wafer piece indicates that the form of the substrate is important for magnitude and spatial extent of the boundary effect in the spin-coating process. Thus, the corners of rectangular Si wafer pieces appear to be important for the spin-coating process. Speculatively, the corners of the Si wafer act as preferential exit point for the coating solution and canalize it. Based on this assumption a substrate holder was developed embedding the Ti cylinder flush in a larger plane of rectangular shape (see chapter 2.1 and Figure 5b and c). With this specifically designed substrate holder the boundary effect was supposed to shift mostly to the holder where it is minimized by the presence of corners. Indeed, this approach drastically reduced the boundary effect on a Ti cylinder with regard to extent and magnitude as can be seen in Figure 14b. Applying the specifically designed custom made substrate holder the boundary effect on the Ti cylinder almost completely disappeared. A slightly increased thickness was observed ~ 700 μm away from the substrate boundary but the film thickness approached a value similar to the center region beside this maximum. If the specifically designed substrate holder was applied, the boundary effect on the Ti cylinder was smaller than the boundary effect on the Si Wafer. This observation is in accordance with the observed difference in specific Ir loading for Si wafer and Ti cylinder (see Figure 11b). Independent of the rotational velocity during spin-coating the Ir loading on the Ti cylinder

was smaller than on the Si wafer, due to the smaller boundary effect on Ti cylinders coated using the custom made sample holder.

3.5 Conclusion

Thin Ir or, respectively, Ru based oxide films are an excellent model system for fundamental investigations of OER activity and stability, since they allow for microkinetic OER studies in a rather big potential range with negligible mass transport effects, for a meaningful application of surface confined analytical techniques and for the study of catalyst substrate interactions. Variation of the substrate form and material facilitates the application of versatile analytical techniques and allows especially for the study of catalyst substrate interactions. However, Ti was identified as the most suitable substrate. The synthesis following a thermal precursor decomposition route directly on the substrate ensures the comparability of the model catalysts with common Ru and Ir oxide PEM catalysts. In this context, the utilization of an acetate instead of a chloride based precursor facilitates the low temperature synthesis of oxides with high purity. The developed spin-coating approach allows for the precise control of the oxide film thickness and, hence, the oxide loading. Based on this spin-coating process the film thickness can be adjusted to the desired value of 50 nm. Boundary effects leading to a deviating film thickness in the boundary region could be dramatically reduced by the development of a specifically designed spin-coating sample holder. Based on this sample holder very homogenous films could be obtained extending even until the substrate boundary.

4 Impact of IrO_x species and catalyst-substrate interactions on the OER activity and stability

This chapter is predominantly based on the following publications:

- 1.) Reier, T.; Teschner, D.; Lunkenbein, T.; Bergmann, A.; Selve, S.; Kraehnert, R.; Schlögl, R.; Strasser, P. *J. Electrochem. Soc.* **2014**, *161*, F876.**
- 2.) Reier, T.; Weidinger, I.; Hildebrandt, P.; Kraehnert, R.; Strasser, P. *ECS Trans.* **2013**, *58*, 39.**
- 3.) Cherevko, S.*; Reier, T.*; Zeradjanin, A. R.; Pawolek, Z.; Strasser, P.; Mayrhofer, K. *J. J. Electrochem. Commun.* **2014**, *48*, 81.

*equal contribution

**Reproduced by permission of ECS-The Electrochemical Society.

Ir oxide is, according to its material properties, one of the most appropriate OER catalysts in acidic media combining a high OER activity with an outstanding stability, as was shown in section 1.2. Although Ir oxide has been extensively studied during the past decades^{15,23,28,30,39,77,78}, the relationship between catalyst structure and composition on the one hand, and the OER activity and stability on the other hand has remained unclear. However, a more profound understanding of this relationship is required for the knowledge-based optimization of Ir oxide electro-catalysts. Furthermore, an in-depth understanding of pure Ir oxide OER catalysts can act as starting point for advanced catalyst design and, hence, help to pave the way towards novel catalyst materials providing high OER activity and stability at minimized noble metal content.

Although the material properties of Ir oxide itself are of great importance, regarding Ir oxide separate and independent from its environment in the actual catalyst might oversimplify the picture due to possible catalyst-substrate interactions. However, previous works on substrate-supported OER film catalysts, including Ir oxide, have grossly neglected a closer look at interactions of the substrate with the catalytically active coating. This is surprising, as the catalyst substrate junction is of great importance for the overall electrocatalytic activity of the catalyst. Considering the common substrate Ti, several different catalyst-substrate interactions appear plausible. For instance, the

catalyst can be chemically influenced by the substrate or an interlayer of a new compound can be formed at the junction between catalyst and substrate. This interlayer may have distinctly different electrocatalytic activity and/or electric conductivity. If the interlayer displays a poor electric conductivity, this can cause an additional voltage drop, resulting in the need for higher overpotentials, as demonstrated by Scheuermann et al.⁵⁹. However, the characteristics of an interlayer formed during thermal preparation of Ru or Ir oxides on Ti substrates are not known. Although evidence was found by secondary ion mass spectroscopy that Ti is partly oxidized in this case,⁷⁹ the properties of this oxide layer and its impact on the OER remain unclear. Identifying and understanding materials at the catalyst substrate junction, their properties and their interactions are therefore of great importance for rational catalyst design. Hereby, thin-film catalysts represent an adequate system, since the catalyst-substrate junction, including a possible interlayer, constitutes a rather large fraction to the system, facilitating its investigation.

In order to study the influence of Ir oxide material properties as well as catalyst-substrate interactions on the OER activity and stability, Ir oxide thin-film (IrOF) model catalysts were synthesized at various calcination temperatures. This procedure yields in distinctly different Ir oxide species and catalyst-substrate interactions. In the following, first the physico-chemical material characterization of IrOFs and their interaction with the Ti substrate will be presented. Afterwards, results obtained for the OER activity and Ir dissolution stability will be provided. Linking the results from material characterization to the OER activity and Ir dissolution stability, the governing material properties are identified. The IrOFs were coated onto a variety of different substrates (Ti cylinder, Si wafer and Ti coated Si wafer (TS)) depending on the desired information and the analytical technique applied as depicted in Figure 15. Whenever Ti cylinders were not applicable for a certain analytical technique but a Ti substrate was required, TS were used (cross-section microscopy, XPS and TPR). Si wafers were used to examine IrOFs in absence of an Ir oxide-Ti (oxide) interface.

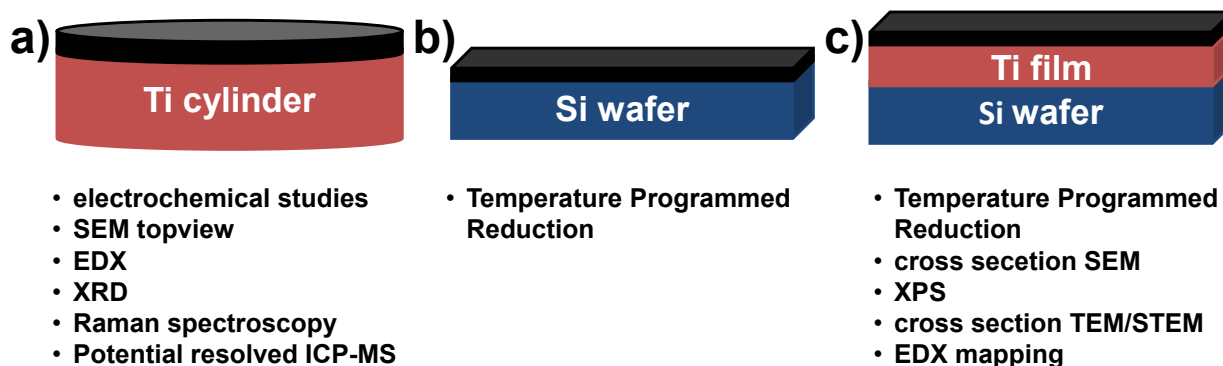


Figure 15: Graphical representation of the different substrates applied for the study of Ir oxide films (IrOF, shown as black layer) (a: Ti cylinder, b: Si wafer, c: Ti coated Si wafer (TS)). The experimental techniques for which the respective substrate was applied are listed below the substrates.

4.1 Physico-chemical material characterization

4.1.1 Morphology of Ir oxide thin-film catalysts

4.1.1.1 SEM

Figure 16 shows SEM images of Ir oxide films (IrOF) calcined at different temperatures. In the upper part of Figure 16 (a-d) top view images of IrOFs on Ti cylinders demonstrate that all films are homogeneous and smooth. The morphology changes as a function of temperature. Starting at 250°C the film appears almost untextured. With increasing temperature the apparent porosity increases moderately. The apparent porosity can additionally be traced in the cross-section micrographs applied on TS (see Figure 16 e-h). The layered structure remains intact at all calcination temperatures but changes in morphology and layer thickness can be observed. The topmost layer is comprised of an approximately 55 nm thick Ir oxide layer. Underneath, between Ir oxide and Si wafer, the Ti layer can be observed with an approximate thickness of 90 nm. Interestingly, the Ti layer thickness is only constant up to 450°C. At 550°C the Ti layer expands significantly to a thickness of about 140 nm and is converted into two distinguishable layers. In both layers the texture is increased compared to the Ti layer obtained at lower calcination temperatures. The upper layer consists of bigger grains. An expansion of the Ti layer under the applied conditions (calcination in air) can be

rationalized by Ti oxide formation. If for instance Ti is oxidized to rutile type TiO₂, the unit cell expands from 35.7 Å³ to 62.5 Å³.⁵¹ This would increase the former 90 nm Ti film to a TiO₂ film with a thickness of approximately 158 nm. Here, we observed only an increase to approximately 140 nm, demonstrating that either not the complete film is oxidized, as indicated by the observation of two differently textured layers, and/or that another Ti oxide species is formed.

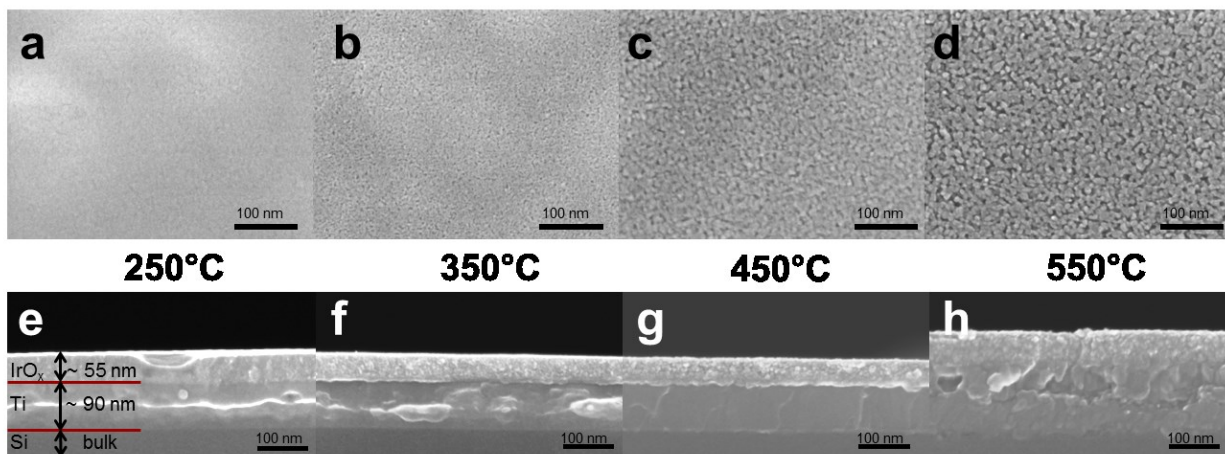


Figure 16: SEM images of Ir oxide films (IrOF) calcined at different temperatures. a-d: Topview images of IrOF coated Ti cylinders calcined at temperatures between 250°C and 550°C. e-h: Cross section images of IrOFs deposited on TS calcined at temperatures between 250°C and 550°C.

4.1.1.2 TEM/STEM

A detailed analysis of the changes appearing at 550°C was performed on a thin electron beam transparent cross-section of the IrOF coated TS by a combined analysis of TEM/HAADF-STEM measurements and EDX elemental mapping (see Figure 17). The TEM and HAADF-STEM images (Figure 17a and b, respectively) demonstrate the existence of 4 different layers on top of the Si wafer, whereas only 3 layers were identified from the SEM image. Especially the layer L1 was not distinguishable in the SEM image (compare Figure 17h). The first approximately 17 nm thick layer (L1) is composed of Ti and Si as shown by the overlap of the corresponding EDX elemental maps (see Figure 17d and e) and can be most likely interpreted as formation of a titanium silicide. Only a small fraction of the Ti layer is mixed with silicon rendering the Ti in contact with Ir oxide uninfluenced by Si. Moreover, silicide formation is retarded at

lower temperatures resulting in even smaller silicide amounts for all other calcination temperatures.⁸⁰

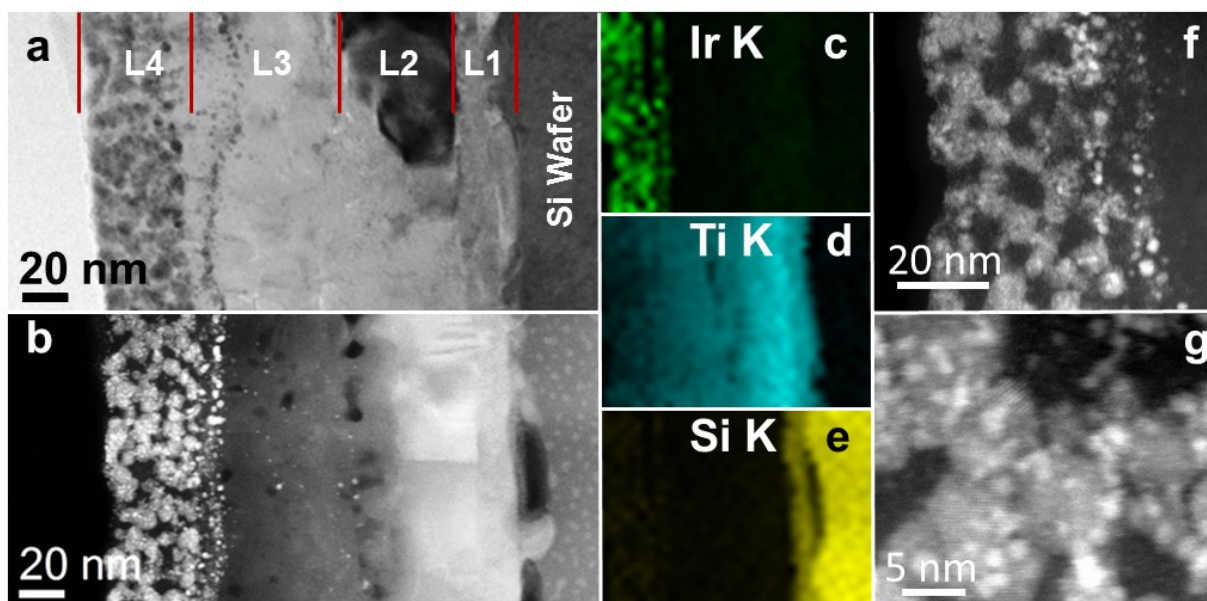


Figure 17: *TEM/STEM cross section investigation of the Ir oxide film on a TS wafer calcined at 550°C. a: TEM image (herein the 4 layers on top of the TS are labeled as L1-L4), b: corresponding STEM image, c-e: EDX elemental mapping over the layered system for Ir, Ti and Si, f: STEM image of the topmost layer (L4) and g: high resolution STEM image of L4.*

The Ti and Si mixed layer L1 is followed by two mainly Ti containing layers L2 and L3. Considering the HAADF-STEM image (Figure 17b), wherein the contrast is due to Rutherford scattering approximately proportional to Z^2 , layer L3 appears darker than layer L2. Under the given reaction conditions (calcination in air) this observation can most likely be explained by Ti oxide formation with an oxidation state gradient of Ti. Closer to the surface (L3) Ti is more oxidized, the oxidation state decreases deeper in the Ti bulk (L2). The top layer L4 constitutes the applied IrO_x layer. An intermixing between L3 and the topmost layer L4 can be observed. The bright spots (see Figure 17b) within the Ti oxide layer L3 indicate penetration of Ir oxide originating from layer L4. This interpretation is supported by EDX elemental mapping (see Figure 17c). Interestingly, Ti can also be found in layer L4 as demonstrated by EDX elemental mapping (see Figure 17d). In agreement with the HAADF-STEM images of layer L4 (Figure 17f and g) the film obtained after calcination at 550 °C consists of at least two different phases. In Figure 17g the bright regions correspond to an Ir rich oxide species

whereas the darker parts are due to a Ti rich species leading to morphology like a supported catalyst.

4.1.1.3 Film composition

EDX spectra measured for IrOFs, including the as-deposited uncalcined acetate precursor film, showed that all samples were exclusively composed of the expected elements Ir, O, C and Ti. Figure 18a depicts a representative EDX spectrum of an IrOF calcined at 550°C (abbreviated in the following as IrOF(calcination temperature)) on a Ti cylinder. Figure 18b shows the EDX results for all applied calcination temperatures. Herein, the uncalcined film is depicted at 25°C. Comparing the uncalcined film with the one calcined at 250°C, the C content decreases sharply, due to decomposition of the acetate precursor in accordance with TG-MS results (see section 3.3). Similarly, the O content decreases comparing the IrOF(250°C) with the uncalcined Ir acetate film, as expected when converting Ir acetate to an Ir oxide. However, at higher calcination temperatures the O content increases again, which can be rationalized either by further oxidation of Ir to higher oxidation states or, more likely, by oxidation of the Ti substrate. In contrast to the C and O content, the Ir content is rather constant, demonstrating a reproducible film thickness.

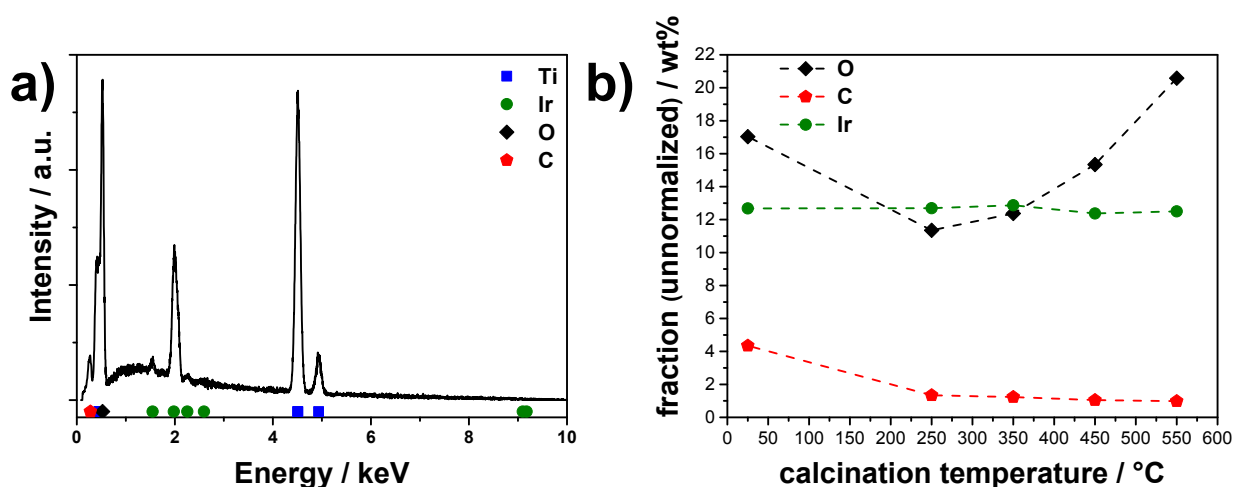


Figure 18: EDX spectrum of IrOF(550°C) on a Ti cylinder (a) and EDX results for all calcination temperatures (measured with 10 kV, substrate: Ti cylinder), including the as deposited uncalcined Ir acetate film (shown at 25°C) (b).

4.1.2 Structural characterization of Ir oxide thin-film catalysts

4.1.2.1 X-ray diffraction

Figure 19 depicts X-ray diffraction patterns of IrOFs on Ti cylinders calcined at different temperatures. The reflections observed for IrOF(250°C) can be assigned exclusively to the hexagonal phase of the Ti substrate (see Figure 19a) demonstrating that this Ir oxide film is X-ray amorphous, although the precursor has been decomposed at 250°C (see sections 3.3 and 4.1.1.3). An additional phase starts to grow at 350°C, identifiable by a small broad reflection at around 28° (see Figure 19b). This reflection grows in integral intensity and narrows with increasing calcination temperature, demonstrating the formation of a more crystalline phase with larger crystallite size. This phase can be identified as a rutile-type oxide based on the additional reflections appearing at 450°C. Nevertheless, at 550°C two rutile-type phases are discernible, as clearly demonstrated by the Rietveld refinement results depicted in Figure 20. Here, for a reasonable refinement quality, an additional hexagonal phase was required (labelled as TiO_x) which can be described as expanded Ti phase (see Table 2 in the appendix). The appearance of this TiO_x phase can be rationalized by the initial insertion of oxygen into the Ti lattice and, thus, by the formation of a Ti oxide different from rutile-type TiO₂. However, this TiO_x phase was not identified at lower calcination temperatures (see Figure 56 and Table 3 in the appendix).

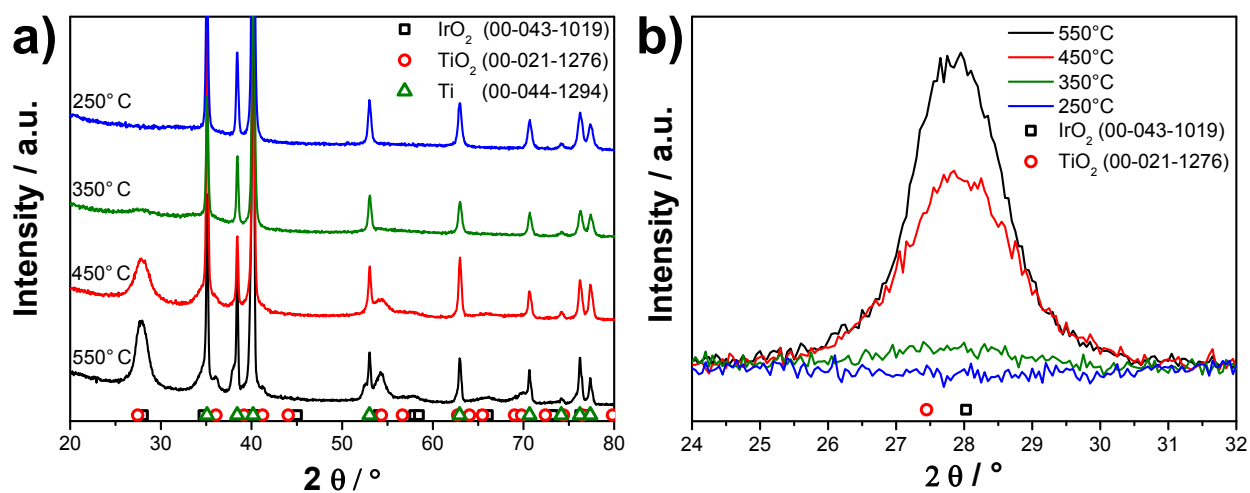


Figure 19: XRD patterns of IrOFs on Ti cylinders (a) and with linear background correction from 24° to 32° 2 Θ (b) to magnify the (110) reflection of the rutile type oxides. Reference patterns from the powder diffraction file (PDF) are provided for comparison (reference number given in parentheses).

Considering the materials applied, one rutile-type phase present in IrOF(550°C) can be assigned to IrO₂, mainly due to the reflections at 34.7° and 40.1° discernible as shoulders of the Ti reflections at 35.1° and 40.2°, where IrO₂ reflections are separated from the TiO₂ rutile phase reflections (see Figure 19 and Figure 20). Rutile-type TiO₂ reflections, separated from IrO₂ reflections, appear at 36.1° and 41.2°, visible as shoulder of the Ti reflections at higher scattering angles. Nevertheless, since most reflections of the rutile-type oxides overlap and only weak reflections are separated, a certain degree of intermixing cannot be excluded. At calcination temperatures of 450°C and 350°C reflections are too weak and too broad to decide if two rather similar or only one rutile phase is present. Considering the IrOF(450°C) a reasonable Rietveld refinement quality was achieved already with one rutile-type phase (beside one hexagonal Ti phase, see Figure 56 and Table 3 in the appendix); a second rutile-type phase improved the refinement quality only slightly (not shown). Hence, in case of IrOF(450°C) it cannot be judged if one or two rutile phases are present.

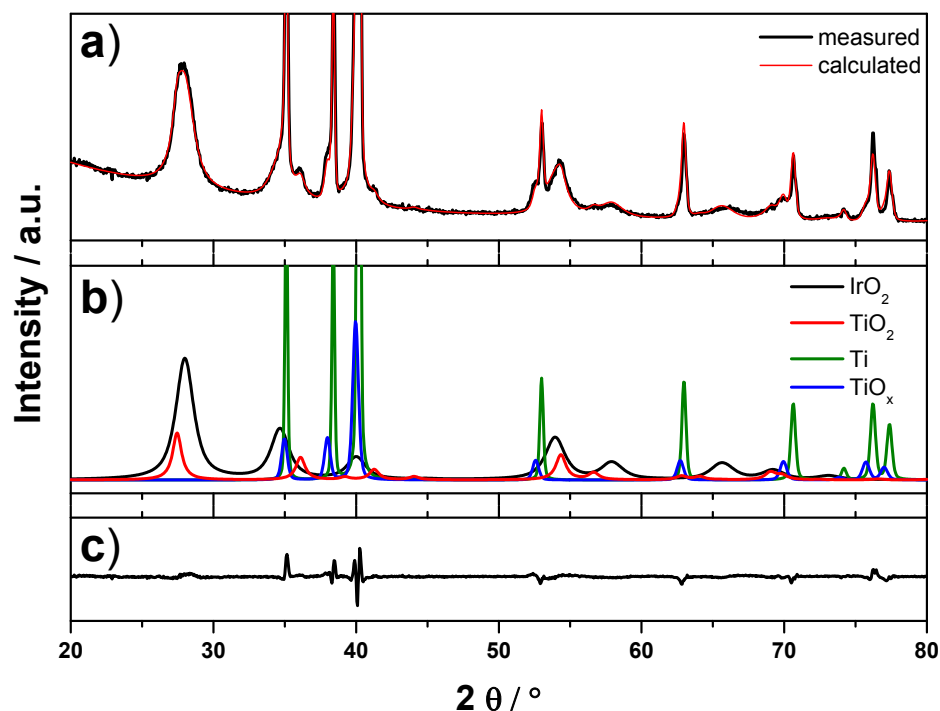


Figure 20 : *Grazing incidence X-ray diffraction measurement of IrOF(550°C) on a Ti cylinder together with results from Rietveld refinement. a) Measured and calculated diffraction pattern, b) contribution of the individual phases used within the refinement and c) difference between measured and calculated diffraction pattern.*

4.1.2.2 Local structure investigated by Raman spectroscopy

To probe the local structure, Raman spectra were recorded (see Figure 21). For all calcination temperatures, two features are observable at about 550 and 750 cm^{-1} , whereby the latter is a convolution of two peaks. A weak peak around 350 cm^{-1} is visible up to 450°C. According to the work of Liao et al., these signals can be attributed to IrO₂.⁸¹ Raman measurements of an IrO₂ single crystal revealed 3 Raman bands at 561 (E_g), 728 (B_{2g}), and 752 cm^{-1} (A_{1g}).⁸¹ Graphical representations of the involved lattice vibrations are depicted in Figure 22. Moreover, on polycrystalline samples an additional, yet not assigned, band at 363 cm^{-1} was observed.⁸¹

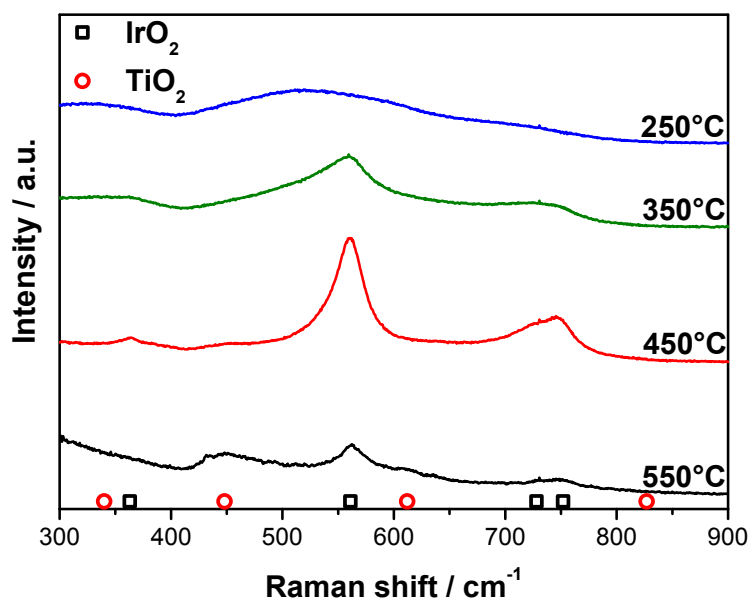


Figure 21: Raman spectra of IrOFs on Ti cylinders calcined at different temperatures together with reference Raman shifts for IrO₂⁸¹ and TiO₂⁸².

Interestingly, a blueshift is discernible for the IrO₂ related bands between 250 and 350°C, although the peaks at 250°C are very broad. However, the position of the peak maxima is rather constant at and above a calcination temperature of 350°C. A change in the Raman shift can be induced by a change in the lattice displacement properties, possibly caused by a slight structural change or a deviating binding energy. Moreover, the half-width of the IrO₂ bands decreases with increasing calcination temperature. This

decreasing half-width can be attributed to crystallization and structural ordering of amorphous films, as pointed out by Liao et al.⁸¹ Thereby, the crystalline order of IrOFs is demonstrated to increase with increasing calcination temperature up to 450°C. However, Ir oxide can be identified already at 250°C and is present at all other temperatures.

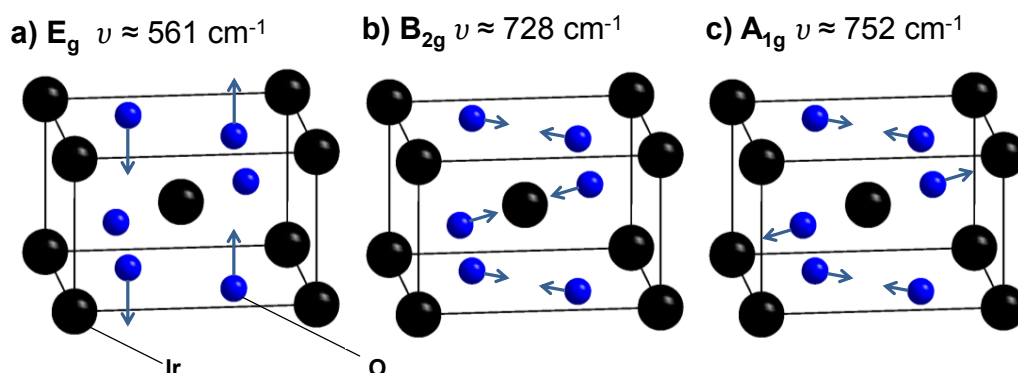


Figure 22: Graphical representation of the E_g , B_{2g} and A_{1g} lattice vibrations in the rutile-type structure according to⁸² together with the vibration frequencies from⁸¹.

At a calcination temperature of 450°C, an additional weak feature at $\sim 450 \text{ cm}^{-1}$ becomes discernible. This peak persists at 550°C and is accompanied by a shoulder at approximately 620 cm^{-1} . These features can be attributed to the most intense modes of rutile-type TiO_2 located at 447 (E_g) and 612 cm^{-1} (A_{1g}).⁸³ Remarkably, the IrO_2 signals sharply decrease in intensity moving from 450°C to 550°C calcination temperature. This observation can be attributed to a decreased amount of original IrO_2 accompanied by TiO_2 formation. According to section 4.1.1.2 the loss of original IrO_2 might be related to an intermixing of Ir and Ti oxide. Additionally, a diffuse scattering background is observable up to 400 cm^{-1} which is attributed to photoluminescence of semiconducting TiO_2 .

4.1.3 Surface chemical characterization

4.1.3.1 XPS

The chemical state of the near surface region was characterized by X-ray photoelectron spectroscopy. Figure 23a shows photoelectron spectra of the Ir 4f region of IrOF coated TS for all calcination temperatures. The Ir 4f region (Figure 23a) of all samples shows an asymmetric peak profile, with the binding energy of $\sim 61.7 \text{ eV}$, being very close to that of

IrO₂. This demonstrates that oxidized Ir is present on all surfaces, even already for IrOF(250°C). This is in line with the Raman spectroscopic observations presented in section 4.1.2.2. Closer inspection of the XPS profiles reveals slight differences, as the spectrum of IrOF(550°C) is sharper and the width of the peak seems to increase towards lower calcination temperatures. The Ir 4f spectrum of IrOF(550°C) overlays perfectly with a reference IrO₂ sample measured in the same instrument.⁸⁴ The strong asymmetry of the IrO₂ signals is due to the high density of state at the Fermi level (Figure 23b) and a corresponding high degree of core hole screening (core hole-valence electron interaction).⁸⁵ The valence band reveals also a clear modulation of the density of states with calcination temperature. Lowering the calcination temperature decreases the occupation of low binding energy states. Owing to the direct coupling of the density of state and the Ir 4f line shape, the small modulation of the Ir 4f line shape has its origin in these differently occupied low binding energy states. The well-developed Fermi edge of the films calcined at and above 450°C similar to IrO₂ indicates first neighbor Ir-Ir interactions. The valence band of IrOF(250°C) suggests that the near surface region of the sample consists of an oxidized Ir, but the band structure typical for crystalline IrO₂ is not yet developed.

Figure 23c depicts O1s spectra of IrOFs with basically three components (adsorbed water: ~533 eV, hydroxyl groups: ~531-531.5 eV and lattice oxygen from IrO₂: ~530 eV) in varying ratios depending on the calcination temperature. All IrOFs calcined between 250–450°C are predominantly hydroxyl terminated with a growing fraction of lattice oxygen upon higher calcination temperature. The lattice oxygen of well-developed IrO₂ has a similar asymmetric line shape, as observed for Ir 4f.⁸⁵ However, due to the lack of crystalline IrO₂ phases after low temperature calcination, the asymmetrical line shape towards high binding energies suggests the presence of adsorbed water on all samples. At a calcination temperature of 550°C the spectrum of the O1s region changes drastically compared to lower calcination temperatures. Here, TiO₂ was detected in the near surface region with a Ti/Ir ratio of 0.9 (Figure 23d), but not upon lower calcination temperatures. Oxygen originating from Ti oxide overlaps with the other signals in the O1s spectrum after 550°C calcination. The appearance of Ti in the 550°C sample is in

line with the observed intermixing of Ti oxide and Ir oxide (see Figure 17) and the morphological change (see Figure 16) exclusively found with this sample.

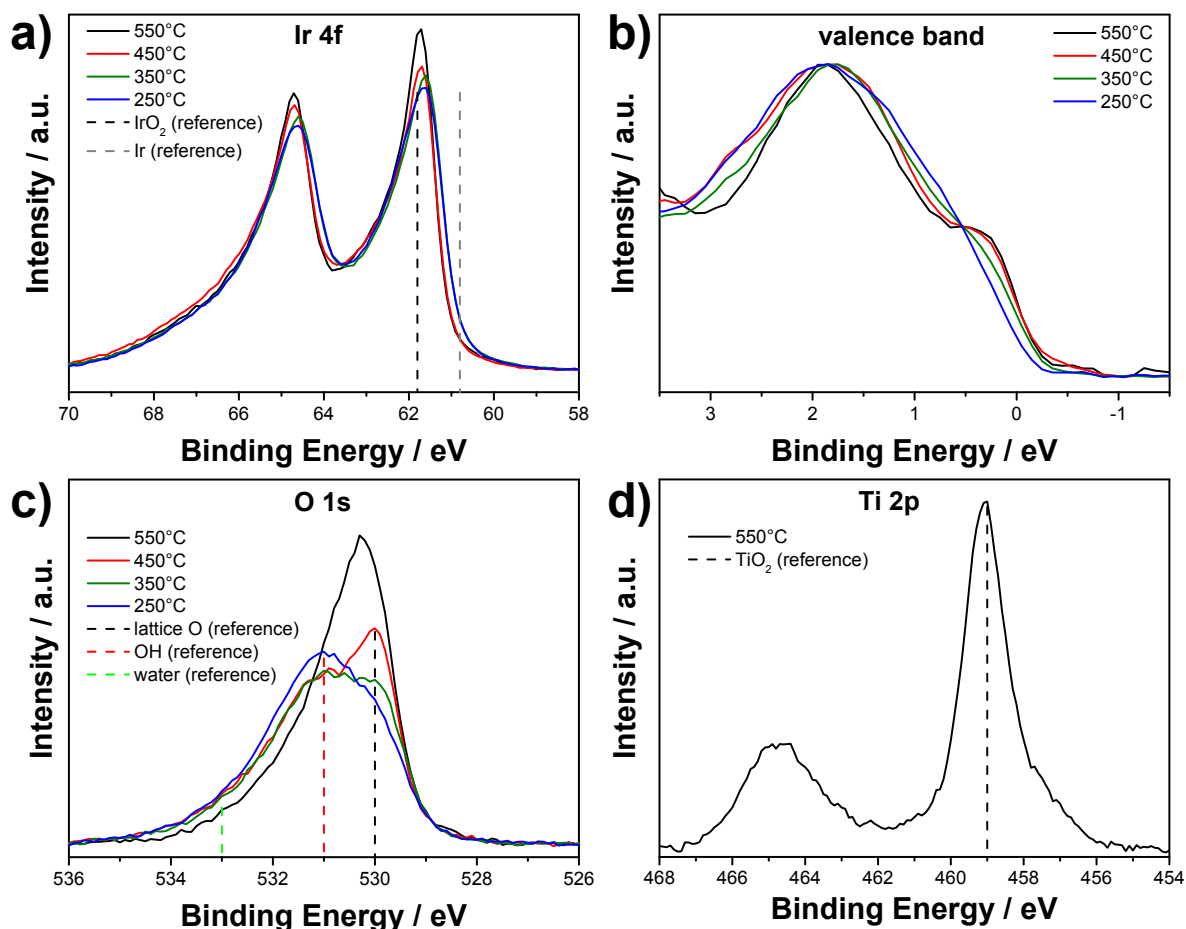


Figure 23: XPS measurements of IrOFs on TS, (a) Ir 4f region, (b) valence band, (c) O 1s and (d) Ti 2p region. The applied photon energies were as follows. Ir4f and VB 599 eV, O1s 1080 eV and Ti2p 1010 eV.

4.1.3.2 Cyclic voltammetry

Electrochemical surface characterization was performed by CV as depicted in Figure 24. Figure 24a demonstrates large changes in the pseudo-capacitive charge q^* , recorded between 0.4 and 1.4 V, depending on the calcination temperature. Remarkably, the charge q^* increases by more than one order of magnitude from the highest to the lowest temperature. The quantity of q^* is frequently interpreted as a relative measure of the electrochemically active surface area^{23,72,74}, and therefore the decay of the pseudo-capacitive charge has important implications for the intrinsic reactivity of the IrOFs. Compared to Ir oxide, Ti oxide has a small contribution to q^* .⁸⁶ Hence, q^* can be applied

as good approximation for the electrochemically active Ir oxide surface area even in presence of Ti oxide. This is relevant for the IrOF(550°C) where Ti oxide was identified in the near surface region. A surface area trend comparable to the q^* values was observed within BET measurements of micelle-templated mesoporous Ir oxide films.⁸⁷

Figure 24b shows electrochemical surface redox properties of IrOFs calcined at different temperatures. Here, currents have been normalized with respect to q^* (measured between 0.4 and 1.4 V, 50 mV s^{-1}) in order to provide comparable current densities. On the basis of this comparison, Figure 24b demonstrates different electrochemical redox properties for the IrOFs calcined at various temperatures. IrOF(450°C) and IrOF(550°C) show a significant current increase above 0.4 V leading to a plateau without formation of defined, clearly discernible peaks. This is a common behavior of thermally prepared IrO₂ electrodes^{30,72}.

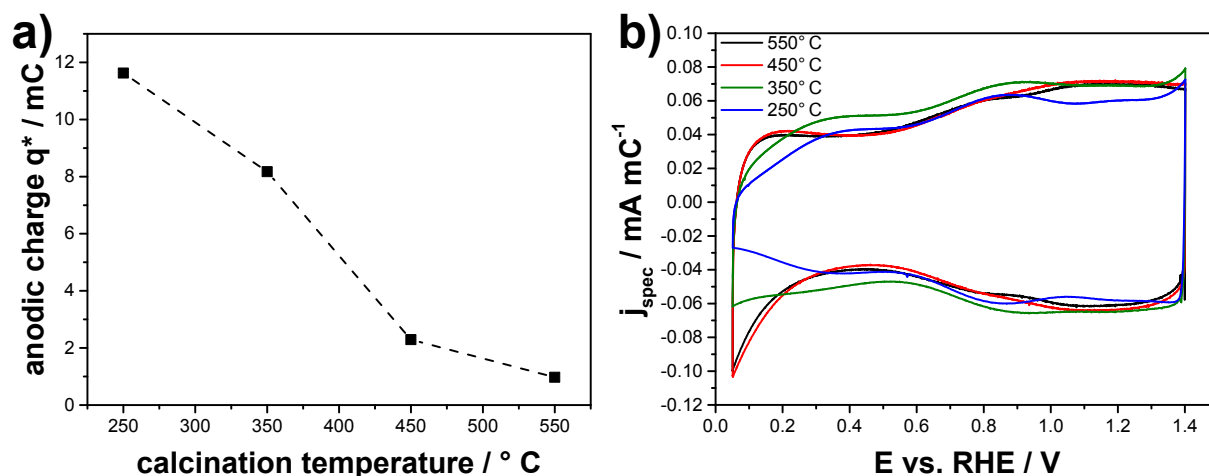


Figure 24: Anodic charge q^* obtained by integration of anodic currents of a CV measured between 0.4 and 1.4 V (50 mV s^{-1}) for IrOFs on Ti cylinders (a). Cyclic voltammetry measured between 0.05 and 1.4 V with 50 mV s^{-1} at room temperature in 0.1 M HClO₄ for Ir oxide films on Ti cylinders (b).

Notably, the IrOF(250°C) shows a clearly distinguishable current peak at approximately 0.9 V. This peak is also present at 350°C calcination temperature, but is slightly shifted towards higher potential. The formation of such a peak is usually observed for electrochemically formed Ir oxides, where it is connected to the Ir(OH)₃/Ir(OH)₄ redox couple.^{15,16} This implies a similar surface species to be present under the mild calcination temperatures of 250 and 350°C.

Considering the low potential region in Figure 24b, further differences are evident. Samples calcined at 450°C and 550°C show a rather sharp reduction feature close to 0 V lacking its direct counterpart in the anodic cycle, common for thermally prepared IrO₂ electrodes^{30,72}. This feature is not observed for the IrOF(250°C). Here, the IrOF(350°C) shows an intermediate behavior, not providing axial symmetry (with respect to the potential axis) like the 250°C sample, but neither displaying the sharp reduction current close to 0 V. Therefore, the IrOF(350°C) can be regarded as intermediate state between the IrOFs calcined at 250°C and 450°C. Connecting this result to XRD and XPS measurements, it can be concluded that the surface chemistry of Ir oxide changes sensitively with crystallinity and the appearance of lattice oxygen at the surface.

4.2 Temperature programmed reduction: Ir oxide and its interaction with the Ti substrate

Temperature programmed reduction (TPR) probes the stability of oxides against reduction and is, therefore, highly sensitive towards their chemical properties. In a TPR measurement the sample is placed in a tubular reactor under continuous H₂/Ar stream while the temperature is raised linearly. The hydrogen consumption is then measured as a function of temperature, demonstrating which portion of the sample is reduced at which temperature. TPR is applied here to identify and analyze chemically different Ir oxide phases and their interactions with the Ti substrate. Properties of pure Ir oxides, without interference of Ti (oxides), were investigated utilizing silicon wafers as substrate. Control experiments by XRD (not shown) indicated no Ir silicide formation under the conditions applied here. Furthermore, uncoated but calcined (in air between 250 and 550°C) Si wafers were measured by TPR and showed no significant reduction peaks. Thus, for the TPR experiments we can rule out the interference of these two effects.

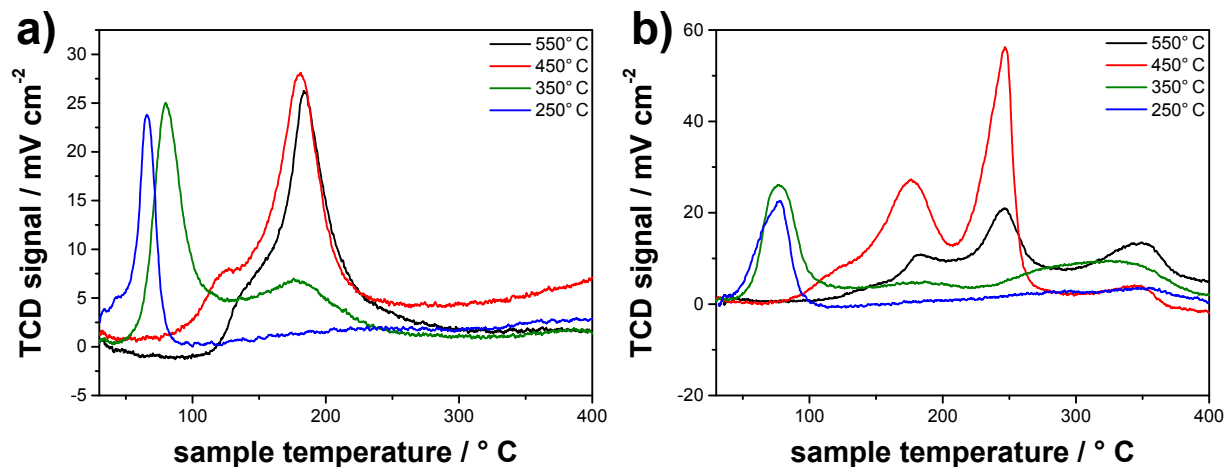


Figure 25: Temperature programmed reduction measured with 10 K min^{-1} . Ir oxide films on silicon wafers (a) and Ir oxide films on TS (b). The detector signal is normalized to the applied geometric film area.

Figure 25a shows TPR results for IrOFs on Si wafers. Here, significantly different reduction properties are apparent depending on the calcination temperature. The IrOF(250°C) shows one major reduction peak around 70°C whereas the IrOF(550°C) shows a major reduction feature at 180°C. This difference indicates a lower stability towards reduction for the IrOF(250°C).

The IrOF(550°C) is not composed of only one Ir oxide phases, as demonstrated by a small shoulder of the main peak around 150°C. This shoulder is more pronounced for the IrOF(450°C). However, beside this the TPR profile is similar to that of IrOF(550°C). Since the IrOF(450°C) and IrOF(550°C) are crystalline whereas the IrOF(250°C) is amorphous, the observed difference in TPR can be correlated to the crystallinity of the IrOFs. Therefore, the main peak at 180°C can be attributed to the crystalline Ir oxide phase and the peak at 70°C to the amorphous Ir oxide/hydroxide. Interestingly, for the IrOF(350°C) a mixture of both oxide phases, the crystalline and the amorphous one, appears, with the larger fraction being the amorphous oxide. This result is in accordance with the intermediate behavior observed in cyclic voltammetry of the IrOF(350°C) (see Figure 25b).

To probe interactions and chemical changes due to the presence of a Ti substrate, TS were applied. Ti and Si are known to react at elevated temperature to form silicides.⁸⁸ However, reference measurements with uncoated TS substrates revealed no TPR

signals up to 400°C and therefore, if any Ti silicide formed, this does not interfere with the reduction pattern of the active coating.

TPR results reveal no significant differences between films on Si and TS calcined at 250°C (see Figure 25a and b). Thus, substrate oxidation effects can be ruled out at this temperature. For the IrOF(350°C) the main features observed on Si are retained, but additionally a new very broad peak appears at approximately 320°C. Since the Ir oxide peaks are retained, this peak can be attributed to a Ti oxide. For the IrOF(450°C) the Ir oxide peaks observed on pure Si are retained in form and size, but additional peaks emerge at approximately 250°C and 350°C. Since Ir oxide is completely reduced at 250°C (signals from IrOF on Si fully retained), this peaks can be attributed to the reduction of Ti oxide species. The preservation of the Ir oxide signals indicate that here Ir oxide is not chemically altered by Ti or Ti oxide. The IrOF(550°C) displays some similarities to the 450°C sample. The peaks around 180°C, 250°C and 350°C are apparent. The latter two peaks have already been assigned to the reduction of Ti oxide species before. Compared to the film on pure Si, the main Ir oxide peak at 180°C diminishes. The diminishment of the Ir oxide peak demonstrates a partial chemical alteration of the Ir oxide induced by the Ti substrate, maybe due to the formation of an Ir-Ti mixed oxide. Evidence for this intermixing are obtained from STEM cross section microscopy (see section 4.1.1.2), XPS (see section 4.1.3.1) and Raman spectroscopy (see section 4.1.2.2).

4.3 Electrocatalytic OER activity

Quasi stationary OER polarizations curves of IrOFs are depicted in Figure 26. For each IrOF two quasi stationary polarization curves were recorded, one at the outset of the electrochemical measurements (OER Scan 1), before the CV measurements in the low potential region were conducted, and one thereafter (OER Scan 2) (see section 2.4.1 for details). For all IrOFs OER Scan 2 yielded a higher OER activity than OER Scan 1, judged based on the overpotential at a constant current density. Thus, the CV measurements appear to have a beneficial effect on the OER activity and act as an activation step. However, all IrOFs experience a rather similar improvement of the OER performance and, hence, relative OER activity trends are not affected although the absolute activities are changed. To evaluate the OER activity of IrOFs and relate it to the

material properties determined in the as prepared state, the OER activity of IrOFs was evaluated based on OER Scan 1.

Figure 27a depicts Tafel plots of OER Scan 1 and shows an almost identical OER performance for IrOFs calcined at 250 and 350°C (overpotential at the same current density). At higher calcination temperatures the curves are shifted towards more positive electrode potentials. The voltage necessary to reach a certain current density (0.5 mA cm^{-2}) can serve as a measure for the electrocatalytic OER activity of a catalyst and is depicted in Figure 27b. IrOFs calcined at 250° and 350°C provide the highest activity, while the activity drops at higher calcination temperatures. The IrOF calcined at 550°C requires the most positive potentials and thereby offers the lowest OER activity. Hence, Ir is most efficiently used in the 250 and 350°C samples, since the Ir loading is constant for all films due to the applied spin-coating process (compare Figure 16).

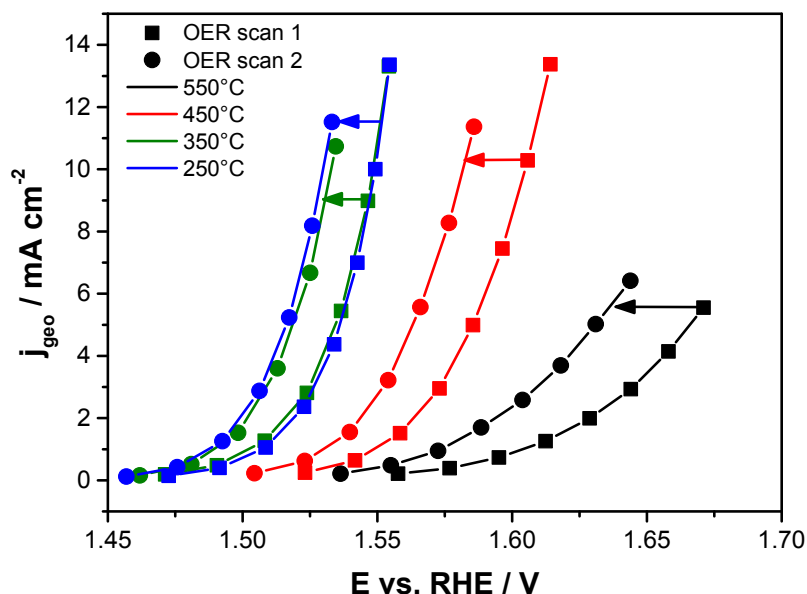


Figure 26: *Quasi stationary OER polarization curves for IrOFs on Ti recorded at the outset of the electrocatalytic measurements (OER scan 1) before the CVs were recorded and thereafter (OER scan 2).*

Due to the different calcination temperatures, the Ir oxide surface areas differ, as was shown in section 0. In Figure 27b, the influence of the Ir oxide surface area is excluded by normalizing the currents to q^* (charge measured between 0.4 and 1.4 V, 50 mV s^{-1}). As pointed out before, q^* is a relative measure of the electrochemically active surface

area, thus this normalization results in surface specific activities. Figure 27b depicts the potential required to reach a specific current density of 0.5 mA mC^{-1} as a measure for the surface specific OER activity. However, considering this measure the principle trend remains unchanged. The IrOFs calcined at 250 and 350°C remain the most active catalysts while the overpotential increases at higher calcination temperatures. Therefore, the observed differences in OER performance are at least partially of intrinsic nature (see Figure 27).

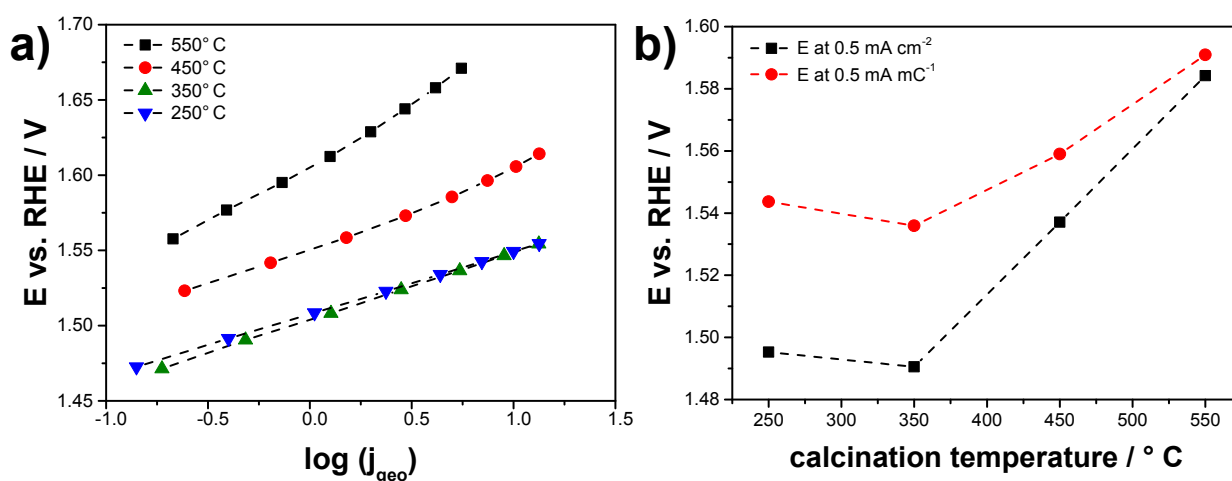


Figure 27: Quasi-stationary OER polarization curves for IrOFs on Ti (OER scan 1). Tafel plot (a) and potential at a current density of 0.5 mA cm^{-2} or, respectively, 0.5 mA mC^{-1} as measure for the OER activity (b).

Tafel slopes in the range of 40 to 60 mV dec^{-1} , common for Ir oxides^{26,28,30,39}, were observed for IrOFs calcined at and below 450°C . Notably, an unusually large Tafel slope of 72 mV dec^{-1} was observed for the IrOF calcined at 550°C . As recently shown by Scheuermann et. al., introducing a TiO_2 layer between catalyst and substrate causes a sharp increase in OER overpotential and Tafel slope due to the poor conduction properties of TiO_2 .⁵⁹ A Ti oxide interlayer was identified in the 550°C samples (see Figure 16 and Figure 17), which can explain the significantly increased Tafel slope and additionally the lowest OER activity observed for IrOFs here. However, the situation is somewhat more complex since indications for a chemical interaction between Ti- and Ir

oxide were evident at 550°C (see sections 4.1.1.2, 4.1.2.2 and 4.2). Furthermore, the observed difference in the OER activity between the IrOFs calcined at 350°C and 450°C cannot be explained on the basis of a Ti oxide interlayer, since the Tafel slopes are not distinctly different. Moreover, no indications for a chemical interaction between Ir oxide and Ti or Ti oxide were found at and below 450°C (compare section 4.2). Therefore, the observed difference in intrinsic electrocatalytic OER activity is more likely related to the presence of distinct Ir oxide phases, which form as function of calcination temperature. The amorphous Ir oxy-hydroxide formed at low calcination temperatures provides a higher OER activity than the crystalline Ir oxide phase.

4.4 Potential-resolved dissolution measurements of Ir and Ti

Stability is the major issue of OER catalysts besides activity and is of utmost importance to ensure long service life and low maintenance on the application level. After the OER activity of IrOFs has been described in the previous section, the Ir and Ti dissolution stability will be the subject of the following section. The Ir stability against dissolution was measured in cooperation with Dr. Serhiy Cherevko from the group of Prof. Dr. Karl Mayrhofer at the Max-Planck-Institut für Eisenforschung in Düsseldorf. The measurements were performed with a scanning flow cell connected to an inductively coupled plasma mass spectrometer (ICP-MS) allowing for the potential and time resolved detection of trace amounts of metal ions in the electrolyte (see section 2.4.2 for details). Here, Ir and Ti were monitored to probe catalyst and substrate corrosion processes.

Figure 28 shows current densities (grey) as function of the electrode potential superimposed with the dissolution profiles of Ir (upper row, a1-e1) and Ti (lower row, a2-e2). Herein, a potential scan was performed in anodic direction starting from -0.05 V_{RHE} until a current density of 30 mA cm⁻² was reached. Beside the IrOFs a polished metallic Ir electrode was investigated for comparison. All samples except the IrOF(550°C) showed an initial Ir dissolution wave below 0.5 V. In contrast, no initial Ir dissolution was detected, if the measurements were started from OCP (approx. 0.9-1.0 V). Thus, this dissolution process is attributed to transient cathodic dissolution related to the reduction of an Ir oxide at low potentials. The IrOF(350°C) showed the highest cathodic transient Ir dissolution amongst the IrOFs (note the different scaling of the axis representing the

dissolution rate in each plot), as can be traced in Figure 28 and Figure 29. Surprisingly, the largest extent of cathodic transient Ir dissolution was detected for metallic Ir. Since cathodic transient dissolution is related to an oxide reduction, this observation indicates the formation of surface oxides on the polished Ir electrode due to the contact with air.

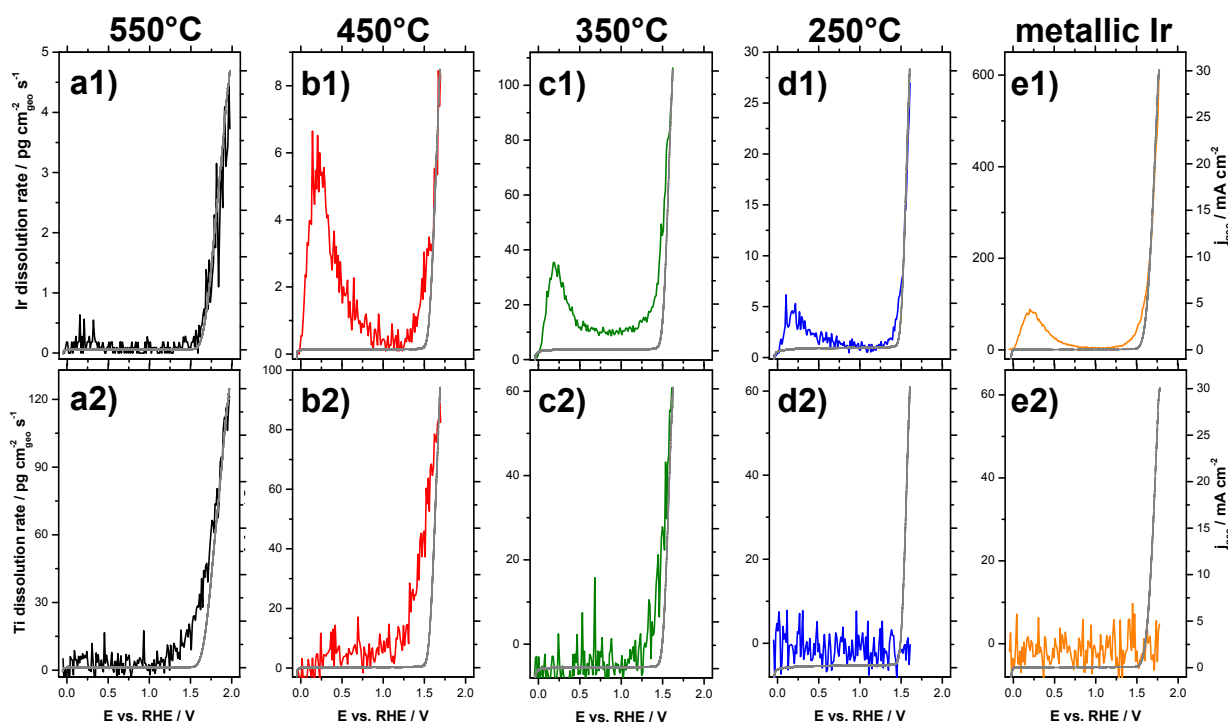


Figure 28: *Potential resolved dissolution measurements of Ir (1, upper row) and Ti (2, lower row) measured for IrOFs (550°C-250°C, a-d) and metallic Ir (e). Reproduced with permission of Elsevier.⁸⁹*

Proceeding to higher electrode potentials, Ir dissolution could be traced for every sample when the OER was in progress. Interestingly, Ir dissolution showed a lower onset potential than the OER, except for IrOF(550°C). The origin of the lower onset potential is not completely clear, but it indicates that both processes are not directly related. Ir atoms may change oxidation state which may trigger Ir dissolution before bulk oxygen evolution is occurring. The integral amounts of dissolved Ir are plotted in Figure 29. Herein, the IrOF(550°C) showed the smallest amount of dissolved Ir (normalized to the geometric surface area) whereas the metallic Ir electrode showed the largest amount of dissolved Ir, which was more than one order of magnitude larger than the highest value observed for the IrOFs (note the break in the axis). Thus, distinct differences in the Ir

dissolution stability were detected. The Ir dissolution stability of low and high temperature Ir oxide phase can be compared based on IrOF(250°C) and IrOF(450°C) in which the low or, respectively, the high temperature Ir oxide phase were exclusively present (see section 4.2). Considering IrOF(250°C) the amount of dissolved Ir was approximately three times bigger than for IrOF(450°C). Thus, crystalline order and a higher fraction of lattice oxygen species in the near surface region improve the Ir dissolution stability. A further improvement of Ir dissolution stability was obtained for IrOF(550°C). Herein, Ti from the substrate was intermixed with the Ir oxide layer during calcination (see sections 4.1.1.1, 4.1.1.2, 4.1.3.1 and 4.1.2.2) giving rise to the improved stability. Remarkably, IrOF(350°C) provided a ~4 times higher Ir dissolution rate than IrOF(250°C), although both were predominantly composed of the X-ray amorphous low temperature IrO_x phase (see section 4.2). In contrast to IrOF(250°C), the IrOF(350°C) also included a minor fraction of the high temperature IrO_x phase. Thus, the coexistence of both phases in one IrOF is detrimental for the Ir corrosion stability. Speculatively, Ir atoms might be in an intermediate state neither included in the crystalline high temperature nor in the amorphous low temperature phase. These Ir atoms are expected to be less sufficiently stabilized against dissolution giving rise to a higher Ir dissolution rate. Interestingly, the trends for anodic and transient cathodic Ir dissolution are rather similar (see Figure 29), indicating that the same material properties are relevant in both cases.

Ti dissolution profiles are shown in the lower row in Figure 28. Compared to Ir dissolution, Ti dissolution appeared solely in the high potential range above 1.0 V, cathodic transient dissolution was not observed. Here, Ti dissolution was traceable for all IrOFs beside IrOF(250°C). The amount of dissolved Ti (during the anodic scan) increased with increasing calcination temperature, as shown in Figure 29. Similarly, TiO_x formation by substrate oxidation was detectable for all IrOFs beside IrOF(250°C) (see section 4.2). Thus, Ti dissolution is related to the formation of TiO_x species at the interface between IrO_x layer and substrate.

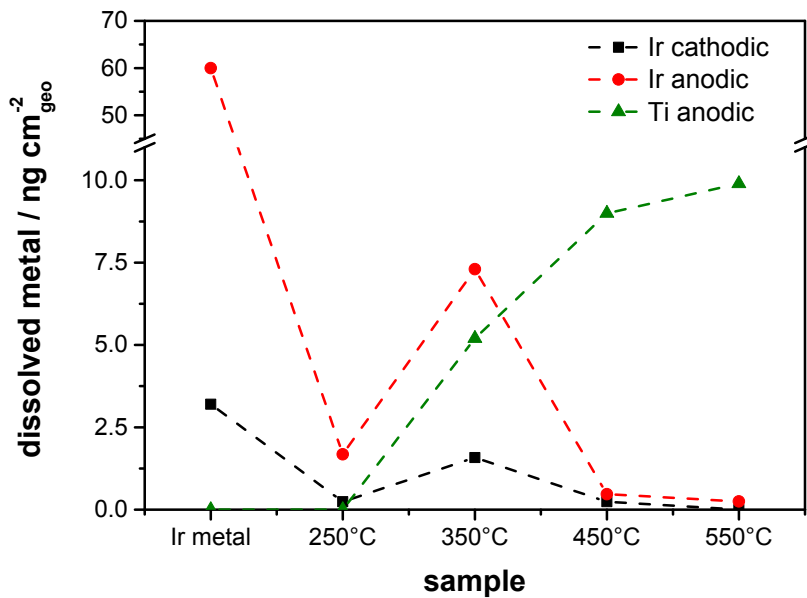


Figure 29: *Integral amount of Ir and Ti dissolved during the potential resolved measurement provided in Figure 28. Ir dissolution is splitted into cathodic (low potential) and anodic (high potential) dissolution.*

Beside the potention-dynamic measurements provided in Figure 28, quasi-steady-state chrono-potentiometric measurements were performed at a fresh spot (see Figure 30). Therefore, the current density was stepped from $j=0 \text{ mA cm}^{-2}$ (Open circuit potential, OCP) to $j=1 \text{ mA cm}^{-2}$ and $j=2 \text{ mA cm}^{-2}$ each for 600 s divided by a break of 180 s at OCP, as depicted in Figure 30a. The related electrode potentials are depicted in Figure 30c and demonstrate an OER activity trend similar to the RDE measurements (see section 4.3). The Ir dissolution rates for all samples, depicted in Figure 30b, showed a sharp peak after stepping to $j=1 \text{ mA cm}^{-2}$ with a fast decay over the first 100 s and a slower decrease in the following 500 s, whereby the Ir dissolution rate appears to converge against a steady state value. However, in case of IrOF(450°C) and IrOF(550°C) the Ir dissolution rate dropped below the detection limit (mean value plus three times standard deviation) at the end of each step. Thus, in the as prepared state some weakly bound Ir species appear to be present that dissolve initially giving rise to a rather high initial dissolution rate. Therefore, potention-dynamic measurements tend to overestimate the dissolution rate on an application level. The metallic Ir electrode showed a rather similar, slightly faster decay of the Ir dissolution rate than the IrOFs.

However, the actual dissolution rate was approximately one order of magnitude larger compared to IrOF(350°C) (note the different scaled axis). This observation underlines the lower stability of electrochemically oxidized Ir compared to the thermally prepared IrOFs.

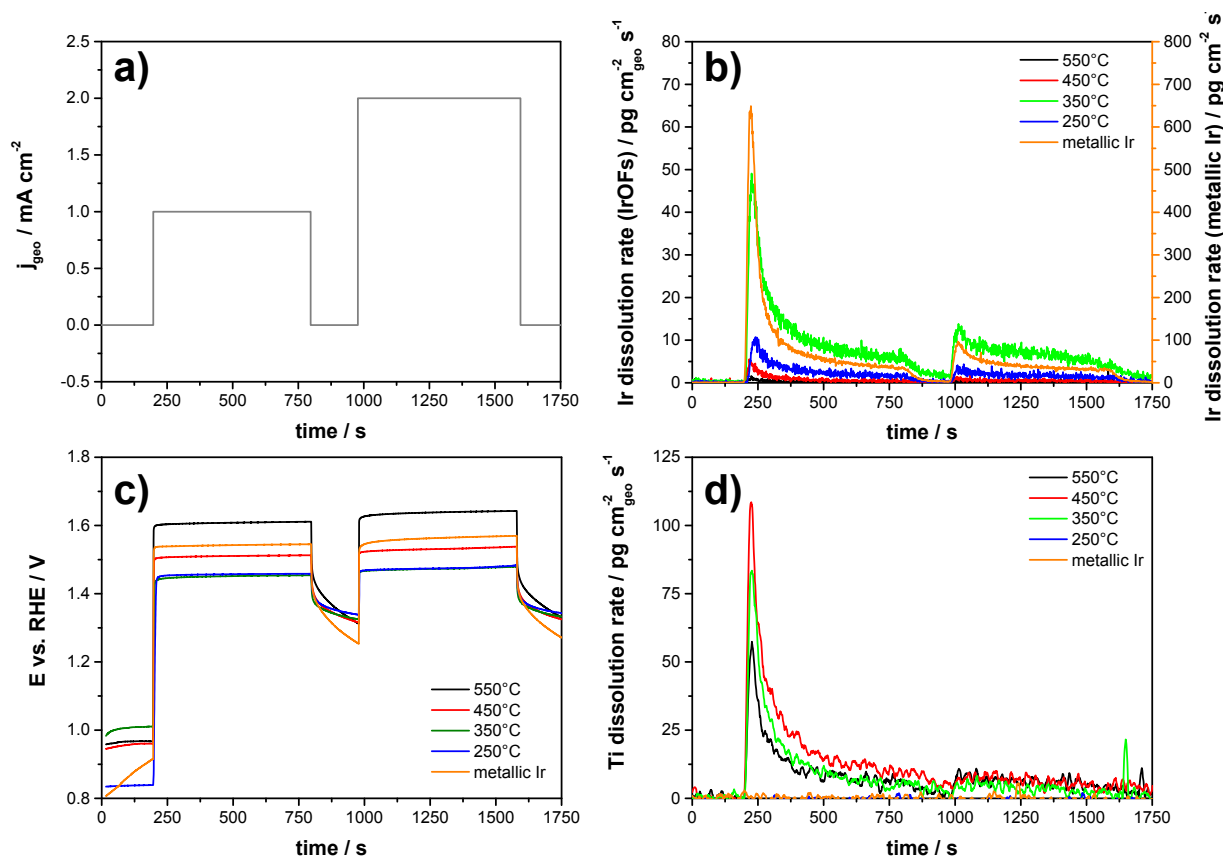


Figure 30: *Potential resolved online ICP-MS Ir and Ti dissolution measurements during chrono-potentiometric OER at 1 and 2 mA cm⁻². Current density and electrode potential as function of time are shown in a and c, respectively. Ir and Ti dissolution rates are depicted in b and d, respectively. Reproduced with permission of Elsevier.⁸⁹*

Considering the second step to $j=2 \text{ mA cm}^{-2}$, the Ir dissolution rate showed a peak again, although less pronounced than for the first step. Thus, some weakly bounded Ir species appear to be recovered during the 180 s break at OCP. Nevertheless, the trend obtained from quasi-steady-state dissolution rates (integral over the step at $j=2 \text{ mA cm}^{-2}$, see Figure 31) was similar to the trend obtained from potentiodynamic measurements (Figure 29).

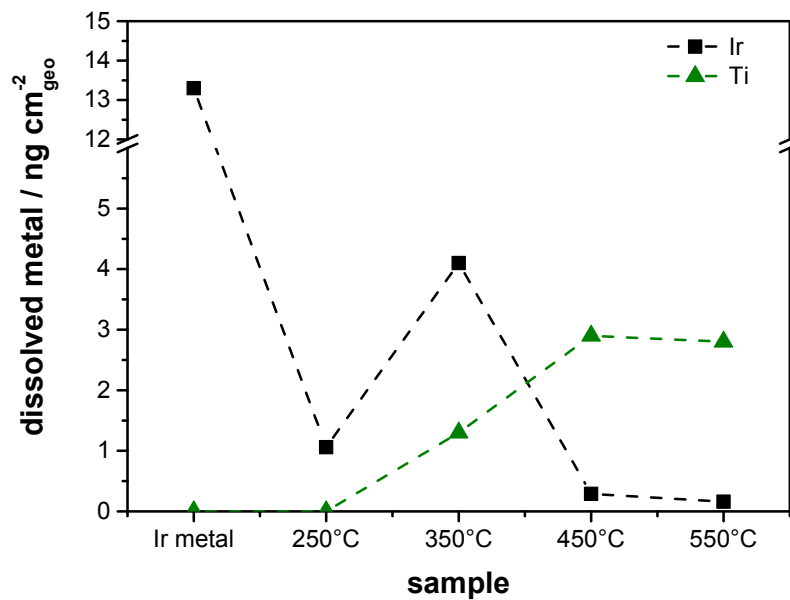


Figure 31: *Integral amount of Ir and Ti dissolved during the second chrono-potentiometric step (2 mA cm^{-2}) depicted in Figure 30.*

In case of Ti dissolution, the dissolution rate showed a peak stepping to $j=1 \text{ mA cm}^{-2}$, similar to Ir dissolution, which decays almost to the background level during the first step (Figure 30d). No peak appeared for the second step. Thus, labile TiO_x species in the as prepared state - formed during calcination - were almost completely dissolved during the first step. Once these labile TiO_x species are dissolved, Ti dissolution falls to a low level but not completely fades out within the time of the measurement. However, the Ti dissolution rates are small.

4.5 Conclusions

In conclusion, two chemically distinct Ir oxides were formed as function of the applied calcination temperature, characterized mainly by differences in crystalline structure, long range order, fraction of surface OH groups and stability against reduction. Electrocatalytic OER measurements demonstrated that the low temperature Ir oxide provided a higher surface specific OER activity than the high temperature Ir oxide whereas the Ir dissolution stability showed an opposite behavior. Thus, one or more of the previously mentioned material properties is expected to be responsible for the difference in OER performance. Additionally, moderate calcination temperatures yielded

maximum electrocatalytically active surface areas. Therefore, the best Ir utilization was achieved at calcination temperatures of 250 and 350°C, which showed almost identical OER activities. Although the OER activities were similar the Ir dissolution rates differed by a factor of ~4. Unexpectedly, the IrOF(350°C) provided a lower stability of Ir against dissolution, which was attributed to the presence of both Ir oxide phases in this film - the low and the high temperature Ir oxide phase. Hence, contrary to often claimed there is not necessarily a tradeoff between OER activity and stability.

Evidence for Ti (substrate) oxidation was found for calcination temperatures $\geq 350^\circ\text{C}$. However, the electrocatalytic properties of Ir oxide were only affected by Ti oxide formation at the highest studied calcination temperature of 550°C. Here, a Ti oxide interlayer was formed and Ti oxide migrated into the Ir oxide layer modifying it chemically. As a result the catalyst calcined at 550°C provided the lowest electrocatalytic OER activity but the highest stability of Ir against dissolution. Ti dissolution increased with increasing calcination temperature and was not observed at a calcination temperature of 250°C. However, Ti dissolution was most pronounced at the outset of the measurement and almost faded out during the course of the measurement. Thus, Ti is an excellent substrate material for OER catalysts.

5 Molecular insight in structure and activity of highly efficient Ir-Ni oxide catalysts for electrochemical water splitting (OER)

This chapter is predominantly based on the following publication:

Reier, T.; Pawolek, Z.; Cherevko, S.; Bruns, M.; Jones, T.; Teschner, D.; Selve, S.; Bergmann, A.; Nong, H. N.; Schlögl, R.; Mayrhofer, K. J. J.; Strasser, P. *J. Am. Chem. Soc.* **2015**, *137*, 13031 (DOI: 10.1021/jacs.5b07788)

Reprinted (adapted) with permission from the American Chemical Society (Reier, T. et al., *J. Am. Chem. Soc.* **2015**, *137*, 13031, DOI: 10.1021/jacs.5b07788). Copyright (2015) American Chemical Society.

Two distinct pure Ir oxide species with distinctly different OER activity and Ir stability were identified in chapter 4. These distinct Ir oxide species were characterized mainly by differences in crystalline structure, fraction of surface OH groups and stability against reduction. Hence, one or more of the before-mentioned material properties appear to determine the OER performance of Ir oxide. Unfortunately, the material properties determining the OER performance cannot be unequivocally identified based on only two data points. To identify the material properties relevant for the OER performance a system is required in which the OER activity and stability can be continuously varied. Monitoring the material properties while the OER activity and Ir stability are changed the governing material properties can be uncovered.

The OER activity of Ru oxide has been modified based on Ru-Ni mixed oxides, which showed enhanced OER activity depending on the Ni content.⁴⁴ This was explained by Ni-rich defects in the Ru oxide lattice acting as preferential sites for the OER⁴⁵. Unfortunately, Ru oxides suffer from severe corrosion under PEM-OER conditions,^{14,46-48} rendering them unsuitable as stable OER catalysts. On the other hand, Nong et al. demonstrated that the addition of Ni to Ir in form of electrochemically oxidized IrNiO_x core-shell nanoparticles boosted the Ir utilization and the intrinsic Ir OER activity.^{49,50} This suggests the great promise of this approach for a continuous variation of the

material properties of Ir oxide. However, to fully unfold its potential, this approach has to be extended to thermally prepared Ir-Ni oxides, because only thermally prepared oxides provide the superior stability required for proton exchange membrane (PEM) electrolyzers or photoelectrochemical cells (PECs).²⁵

In the following thermally prepared Ir-Ni mixed oxide thin-film catalysts will be studied with respect to their OER performance and material properties. The material properties will be examined before and after the OER measurement in order to trace changes induced by the electrochemical treatment. Correlating the OER performance results with the knowledge obtained about the material properties, structure-activity-stability relations can be uncovered.

At the outset of this study seven Ir-Ni mixed oxide thin-film catalysts were prepared, ranging from 0 atomic% (at%) Ni to 100 at% Ni in composition, using the spin-coating approach described in section 2.1.2.3 and 3.4. For convenience and clarity in the following, Ir-Ni mixed oxide catalysts will be referred to as x%Ni-MO (MO for Ir-Ni mixed oxide). Thereby, x specifies the fraction of Ir atoms substituted by Ni (in at%) in the as-prepared mixed oxide.

5.1 Electrocatalytic OER activity and Ir dissolution

The electrocatalytic OER performance of the MO film catalysts was explored using the Rotating Disk Electrode (RDE) technique. Figure 32a depicts quasi-stationary OER polarization curves of pure Ir oxide and MO catalysts. Clearly, mixing Ir and Ni in form of an oxide exhibits a tremendously beneficial effect on the electrocatalytic OER activity yielding in catalyst materials that, judged by their current density at a given overpotential, significantly exceed the catalytic activity of pure Ir oxide. Pure NiO is not shown in Figure 32a due to its poor OER activity in perchloric acid (see Figure 57).

Catalytic OER current densities at a fixed overpotential of 300 mV (1.530 V_{RHE}) are plotted and compared in Figure 32b as measure for the OER performance. Therein, the geometric and the Ir mass based current density exhibit a volcano type curve with a maximum at high Ni contents (67 at% - 79 at%). Compared to the Ir oxide reference catalyst the OER performance was improved by a factor of ~8, based on the geometric current density (j_{geo}), or even more remarkably, by a factor of ~20, based on the Ir mass

based current density (j_{mass}). In other words, using Ir-Ni mixed oxides, the Ir amount of a water splitting anode catalyst could be reduced by a factor of 20 while maintaining the identical OER rate at the same electrode potential. Finally, in order to explore the origin of the tremendous improvement in OER activity, the surface specific OER activity was determined. The established method for the determination of the active Ir oxide surface area makes use of the anodic charge q^* obtained in a fixed potential window (0.4-1.4 V_{RHE}) as a measure proportional to the active Ir oxide area.^{23,72,74} Experimental q^* -values are plotted in Figure 32c; they exhibit a maximum at intermediate Ni contents, indicating that 39%Ni and 67%Ni-MO showed the largest active oxide surface areas. The surface specific catalytic current density (current normalized by q^*) again increase with the Ni content up to 67%Ni-MO (see Figure 32b), but levels off at higher Ni contents within the accuracy of the measurement. Compared to pure Ir oxide, the surface specific OER activity of samples with an initial Ni content at and above 67 at% was increased by a factor of about 2.6.

Besides the electrocatalytic activity, the stability is the other major issue of OER catalysts.⁹⁰ Here the stability of Ir against dissolution was measured using potential-resolved online ICP-MS analysis^{14,91} on samples which previously underwent the electrocatalytic OER protocol (x%Ni-MO-OER). In Figure 32d, the total mass of dissolved Ir during 30 min galvanostatic water electrolysis at 1 mA cm^{-2} is shown as function of the initial Ni content. For the stability discussion, the dissolved Ir mass was normalized to the geometric (black) as well as the active (red) catalyst area (reflected by q^*). Looking at the geometric stability, the amount of dissolved Ir first increased with increasing Ni content and peaked at 79%Ni-MO. At this maximum the Ir dissolution rate is approximately 47 times higher than that of pure Ir oxide, while in the case of 67%Ni-MO it is 34 times higher. Although this appears to be a substantial drop in Ir stability relative to pure Ir oxide, we note that even the least stable thermally prepared MO catalyst film of this study exhibits an Ir dissolution rate that is comparable to electrochemically oxidized Ir metal, and even much lower than electrochemically oxidized Ru metal.¹⁴ Interestingly, geometric OER performance and geometric Ir dissolution rate peak at different Ni contents. Furthermore, 21%Ni-MO-OER showed a dissolution rate 14 times higher than pure Ir oxide although the geometric OER activity

was rather similar. Both observations indicate that OER activity and stability are not directly anticorrelated as often claimed. To show this more clearly, when the amount of dissolved Ir is normalized to the electrochemically active Ir oxide surface area (reflected by q^*) a broad plateau appears at Ni contents ≤ 67 at% (red balls in Figure 32d). The data in Figure 32b and Figure 32d evidence that, although the surface specific Ir dissolution rate is rather constant across the plateau, the surface specific OER activity can be tuned and increases with the Ni content. This provides further evidence for the principle possibility of decoupling OER activity and stability implying the existence of distinct material properties relevant to activity and stability.

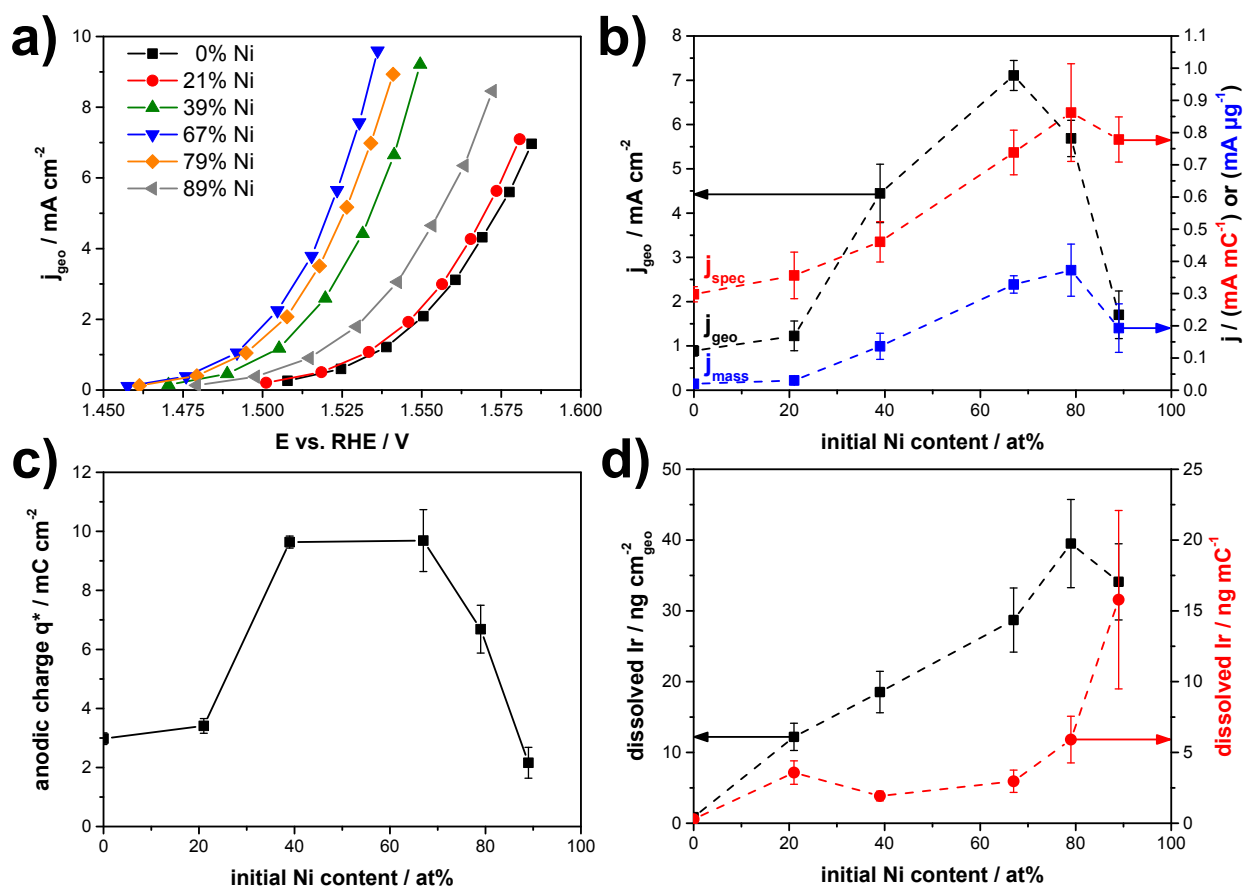


Figure 32: *Electrocatalytic measurements of OER activity and stability of Ir-Ni mixed oxide films with different Ir to Ni ratios, here referred to as x%Ni-MO (x atomic % Ni). a) Quasi stationary OER polarization curves (iR corrected). b) Current densities at an OER overpotential of 300 mV (1.530 V vs. RHE) normalized to the electrodes geometric surface area (j_{geo}), the anodic charge q^* (j_{spec}) and the applied Ir mass (j_{mass}). c) Anodic charge q^* measured by CV between 0.4 and 1.4 V with 50 mV s⁻¹. d) Amount of dissolved Ir during 30 min of OER with 1 mA cm⁻². The amount of dissolved Ir is provided normalized to the geometric surface area and to q^* .*

5.2 Electrochemical Ni dissolution, compositional, and morphological stability

To uncover macroscopic and microscopic materials properties controlling the observed OER activity and Ir dissolution a wide range of scattering, spectroscopic, and microscopic characterization techniques were applied to the as-prepared Ir-Ni mixed oxide samples (referred to as *MO-ap*) and to Ir-Ni mixed oxide samples that had undergone OER catalysis (*MO-OER*).

Scanning electron micrographs of *MO-ap* and *MO-OER*, depicted in Figure 33, revealed morphological changes of the catalysts after OER. *MO-ap* samples generally consisted of dense, grained films with a certain apparent porosity and comparable film thicknesses in the 41 to 58 nm range (see cross sectional studies Figure 58). 0%Ni-*MO-ap* and 21%Ni-*MO-ap* were composed of very fine grains. For catalysts with higher Ni contents individual grains are hardly visible, but the films still revealed an apparent porosity. Instead, some needle-shaped presumably IrO₂ crystals segregated to the surface of the 39%Ni-*MO-ap*.

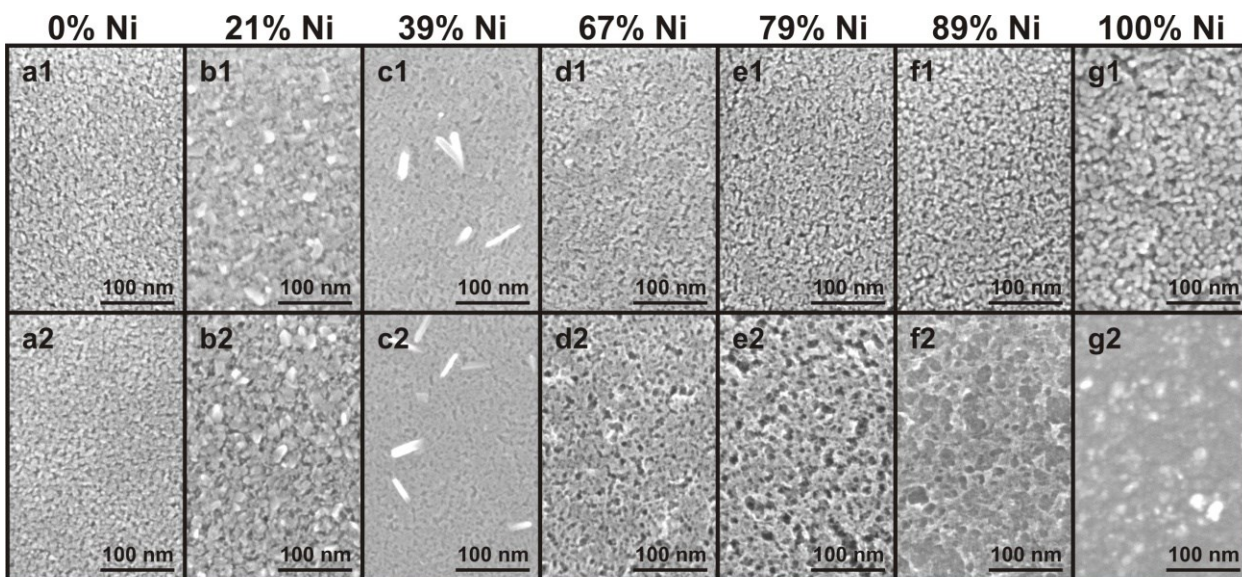


Figure 33: Topview SEM images of Ir-Ni mixed oxide films on Ti substrates with different initial Ni contents acquired on as prepared samples (*MO-ap*, upper row, a1-g1) and samples that underwent the OER protocol (*MO-OER*, bottom row, a2-g2).

After OER, catalysts with ≤ 39 at% initial Ni content remained morphologically stable, while the others showed increasing sponge like porosity with increasing Ni content. This observation suggests that Ni was more and more leached out. In the case of the 100%Ni-MO-OER film its initial nano-crystalline structure vanished after OER due to heavy corrosion.

To understand the Ni leaching, bulk and near surface composition of MO-ap and MO-OER catalysts were determined and plotted against the initial Ni content, see Figure 34a. The bulk Ni content was determined by averaging XPS sputter depth profiles (solid triangles) and for MO-ap additionally by ICP-OES. Both approaches are in excellent agreement for MO-ap, validating the approach of XPS sputter depth profile averaging for bulk Ni content determination. After OER catalysis, bulk and surface Ni content (red symbols) evidence strong, yet incomplete Ni dissolution. For initial Ni contents ≤ 67 at%, residual Ni values surprisingly levelled at around 12 at%, likely stabilized through interaction with Ir. In fact, Ni dissolution rates obtained from online ICP-MS analysis were then in the same range as Ir dissolution rates (see Figure 34b) reflecting the relative stability of remaining Ni in the leached oxides. This observation is important, as it demonstrates that about 12 at% Ni can be stabilized in the mixed oxide matrix and may contribute to electronic and geometric effects beneficial for the water splitting catalysis.

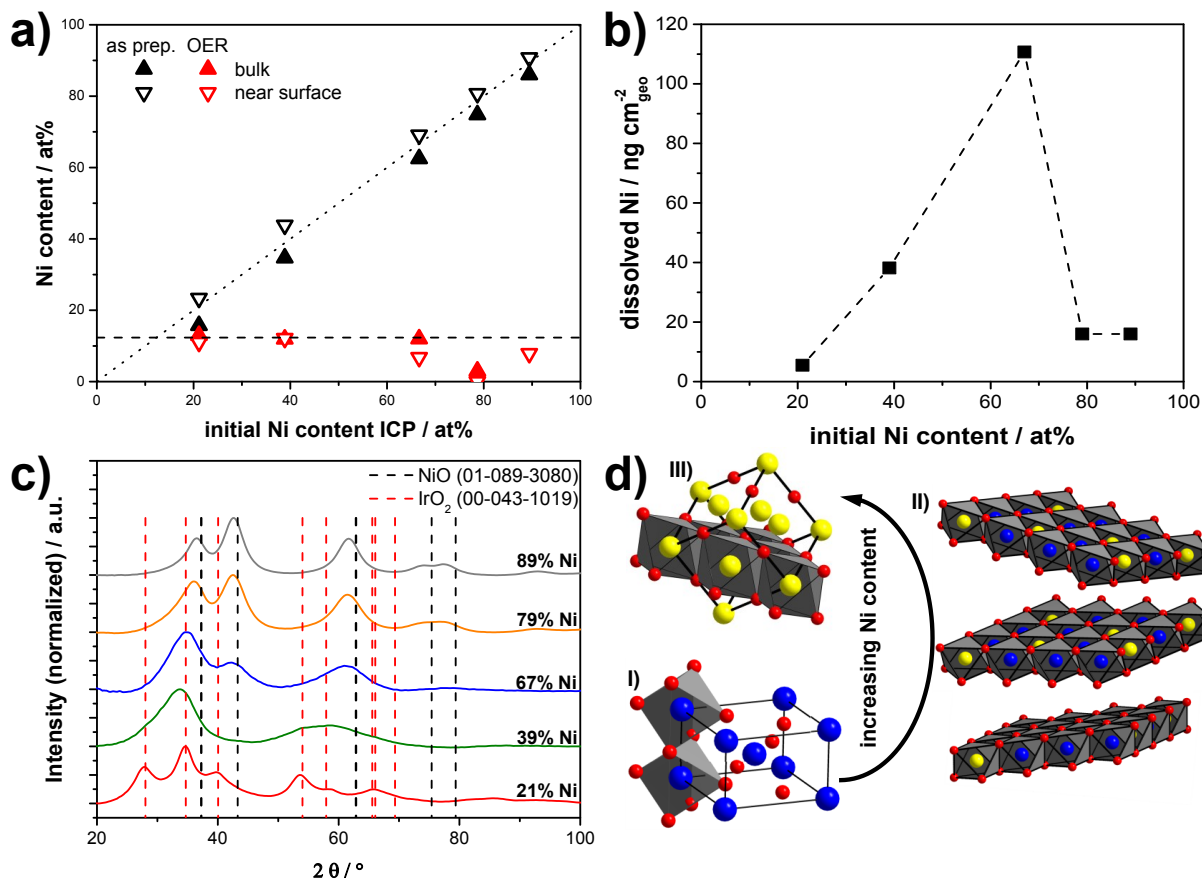


Figure 34: *a)* Near surface and bulk composition of Ir-Ni mixed oxides films before (MO-ap) and after (MO-OER) the electrocatalytic OER protocol. The Ni content measured by ICP-OES is provided on the x-axis. The near surface Ni content and the bulk Ni content shown on the y-axis were determined by XPS or, respectively, by averaging XPS depth profiles. *b)* Amount of dissolved Ni during 30 min of OER at 1 mA cm⁻² measured by potential resolved ICP-MS with MO-OER films. *c)* Integrated and base line corrected selected area electron diffraction measurements of MO-ap transformed into the 2θ scale (Cu K-α). Reference patterns from the powder diffraction file are provided for comparison. *d)* Structural model according to c). I) depicts the rutile type (IrO₂) and III) the bunsenite type (NiO) unit cell. II) depicts a structural model for 39%Ni-MO-ap. (O or OH: red, Ni: yellow, Ir: blue).

XPS sputter depth profiles of Ir and Ni for MO-OER and MO-ap catalysts are depicted in the Figure 35. For the as-prepared catalysts (MO-ap), the Ni content is basically constant across the entire film depth (Figure 35a), consistent with homogenous Ir-Ni mixed oxides. Interestingly, after OER catalysis rather constant Ni contents across the film depth were also observed up to 67 at% initial Ni content, although a large portion of Ni was leached out (Figure 35b). A Ni gradient clearly became apparent for 79%Ni-MO-

OER, although it emerged already for 67%Ni-MO-OER. The 89%Ni-MO-OER film was too thin and too porous to obtain a meaningful depth profile measurement. However, the depth profile measurements demonstrate a surprisingly homogenous Ni leaching across large distances up to 67 at% initial Ni content, precluding mass transport control of the dissolution processes and instead highlighting the formation of Ir-Ni oxide interactions.

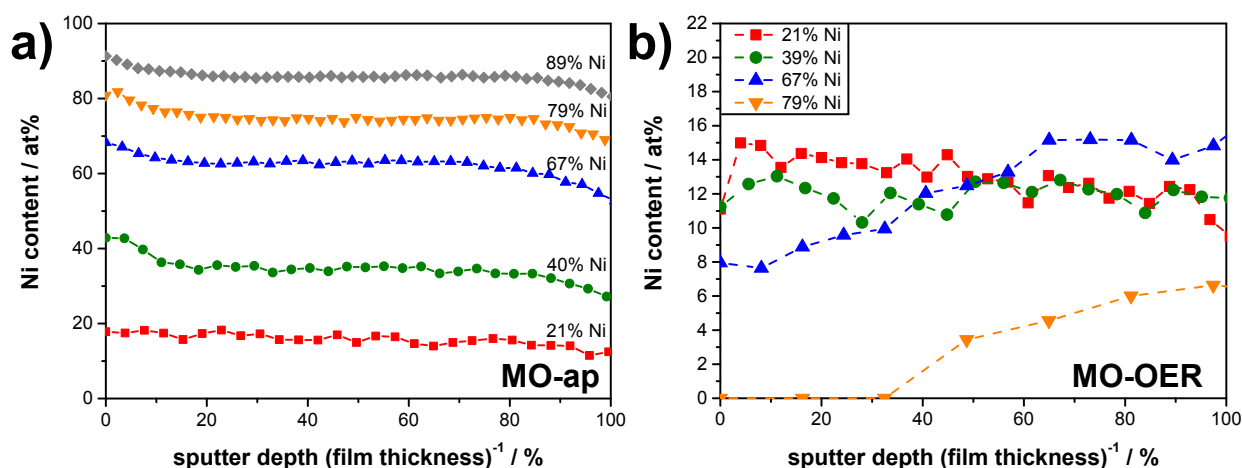


Figure 35: XPS sputter depth profile measurements of MO-ap (a) and MO-OER (b).

Ni leached out from the MO films during the electrocatalytic protocol results in certain Ni concentrations in the electrolyte. To investigate whether Ni ions in the electrolyte affect the OER activity of MO films, an electrolyte exchange measurement was performed based on 67%Ni-MO (Figure 36), which provided the highest geometric OER activity measured here (see Figure 32). For this, the electrolyte was exchanged two times during the course of the electrocatalytic protocol, once before and once after the CV measurement. Thus, Ni is expected to be absent from the electrolyte when the OER scans after the CV measurement (OER scan 2) were started. This measurement is compared to a standard OER measurement in which the electrolyte has not been exchanged (see Figure 36). Herein, both measurements reveal similar geometric OER activities for 67%Ni-MO and, hence, in this case Ni ions in the electrolyte have no effect on the electrocatalytic OER activity.

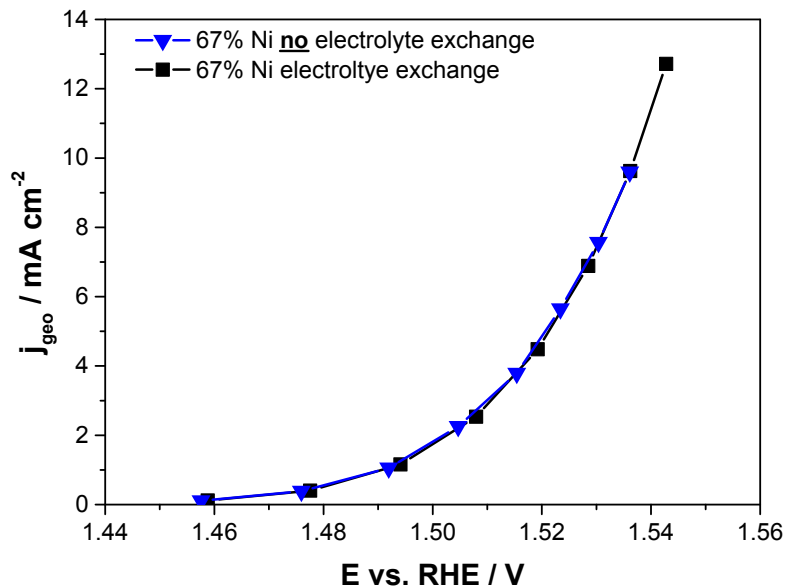


Figure 36: Quasi steady-state OER polarization curves (OER scan 2) of 67% Ni-MO with and without (standard protocol) electrolyte exchange. In case of the exchange measurement, the electrolyte was exchanged two times, once before and once after CV.

5.3 Atomic structure of Ir-Ni mixed oxides

Grazing incidence X-ray diffraction (GI-XRD) was used to probe the crystallinity and to conduct a phase analysis of the MO-ap films. Data in Figure 59 suggested that all films were X-ray amorphous, except pure Ir and Ni oxide as well as the 21%Ni-MO-ap. The pure Ni oxide film formed a single rock salt-type *bunsenite* phase. A rutile-type phase was detected for pure Ir oxide and the 21%Ni-MO-ap film. To further investigate the structure of the MO-ap films at the nanoscale, selected area electron diffraction (SAED) was employed, see Figure 34c. Now, all MO-ap samples showed clear diffraction patterns suggesting nano-crystallinity. Consistent with the GI-XRD data, a rutile-type phase was identified for 21%Ni-MO-ap. The structure of the next higher Ni content catalyst, the 39%Ni-MO-ap, however, changed drastically. Rutile-type reflections vanished in favor of new reflections at approximately 34° and 60° 2θ . With further increasing Ni content an additional reflection at approximately 42.5° evolved and grew in intensity with increasing Ni content. This was accompanied by shifts of the 34° and 60° reflections, until the pattern of an expanded *bunsenite* type structure evolved for the 89%Ni-MO-ap catalyst film.

These findings can be fully accounted for considering brucite like layered structures characterized by layers of edge-sharing Ni-O octahedra. Similar structures are commonly observed for Ni hydroxides and oxy-hydroxides, whereby the difference largely consists in the arrangement of the brucite like Ni-O layers along the *c* axis.^{92,93} Consistent with missing crystalline order between the layers in the 39%Ni-MO-ap catalyst, Figure 34d II depicts a structural model composed of misaligned, turbostratic Ni-O layers with brucite like layer structure. With increasing Ni content the Ni-O layers become more and more interconnected yielding in a three dimensionally ordered structure as seen by the growth of the bunsenite reflection at $\sim 42.5^\circ$. One Ni-O brucite like layer is highlighted in the bunsenite unit cell in Figure 34d III. The continuous downshift of the $\sim 35^\circ$ and $\sim 62^\circ$ reflections with decreasing Ni content indicates a lattice expansion due to the increased incorporation of larger Ir ions. The continuity of the structural changes strongly suggest the presence of one mixed oxide phase in each catalyst other than the pure oxides and, possibly, the 21%Ni-MO-ap, where the intense rutile reflections may impede the resolution of mixed oxide reflections.

5.4 Electronic band structure and surface chemical state of Ir-Ni mixed oxides

To get insight in the electronic structure and the surface chemical states of the Ir-Ni oxide thin-films before and after OER catalysis, X-ray absorption and X-ray photoemission studies were conducted. Figure 37a and b depict the O K-edge X-ray absorption spectra of MO-ap and MO-OER, wherein O 1s electrons are excited to unoccupied states probing the *local unoccupied O 2p density of states*, the fine structure of which is determined by mixing with metal states.⁹⁴ Clearly, the spectra after OER catalysis revealed substantial differences to the as-prepared state (compare Figure 37b and Figure 37a).

X-ray absorption spectra of the samples after OER catalysis are provided in Figure 37b. The spectra of 89%Ni and 100%Ni-MO-OER are not included, since oxygen species stemming from the oxidized Ti substrate contributed significantly to these spectra. This was because extensive Ni leaching rendered the remaining MO-OER film porous and as a result of this it did no longer sufficiently cover the substrate. Interestingly, after OER catalysis, peak 2 shifted to photon energies higher than those of pure Ir oxide and peak

1 shifted slightly to lower photon energies. Thus, the metal-oxygen binding situation is significantly altered by Ni leaching. However, from this data it is not clear if the metal-oxygen binding gets stronger or weaker.

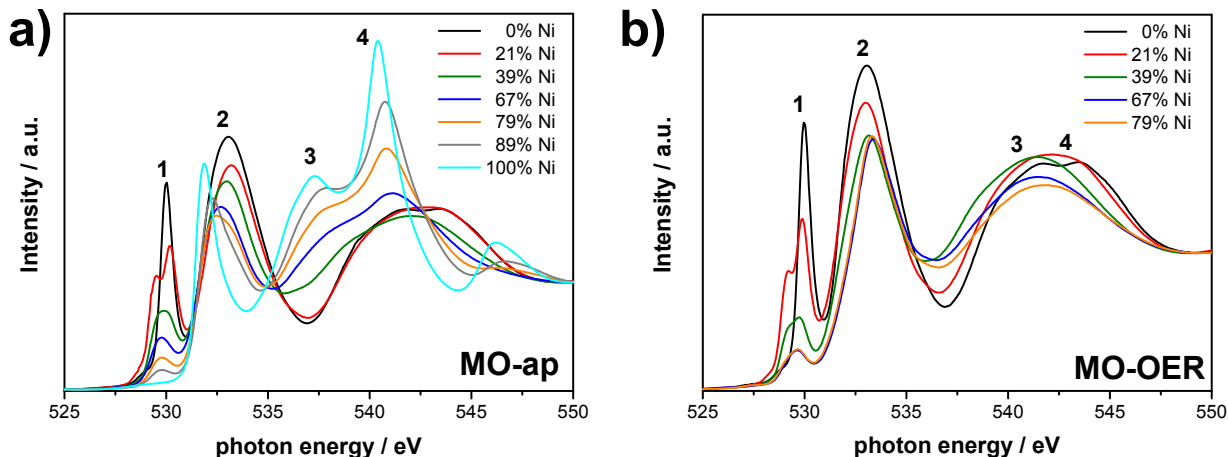


Figure 37: *O K-edge absorption spectra of Ir-Ni mixed oxide films in the a) as-prepared state (MO-ap), and b) after the OER catalysis (MO-OER).*

X-ray photoelectron spectroscopy was used to characterize the chemical state of Ir, Ni and O in MO-ap and MO-OER film catalysts. Figure 38a depict the Ni 2p region of MO-ap catalysts. The pure Ni oxide spectrum showed binding energy and line shape closely resembling to a NiO reference material⁹⁵. Line shapes and binding energies for all MO-ap are essentially similar to the pure Ni oxide film. However, the signals at ~854 eV (p1) and ~856 eV (p2) showed a varying intensity ratio depending on the Ni content. As pointed out by Alders et al. the intensity of p2 relative to p1 in NiO is a function of the local environment around the Ni atoms.⁹⁶ Thus, the observed variation of the p1/p2 intensity ratio likely indicates changes of the local Ni environment dependent on the Ni content, as expected for mixed oxides with different Ir:Ni ratios. XPS line shape and binding energy of the catalytically tested thin-films (MO-OER) in the Ni 2p region remained largely unchanged, see Figure 38c, but p1 almost disappeared consistent with a dramatic change in local Ni coordination environment due to Ni leaching.

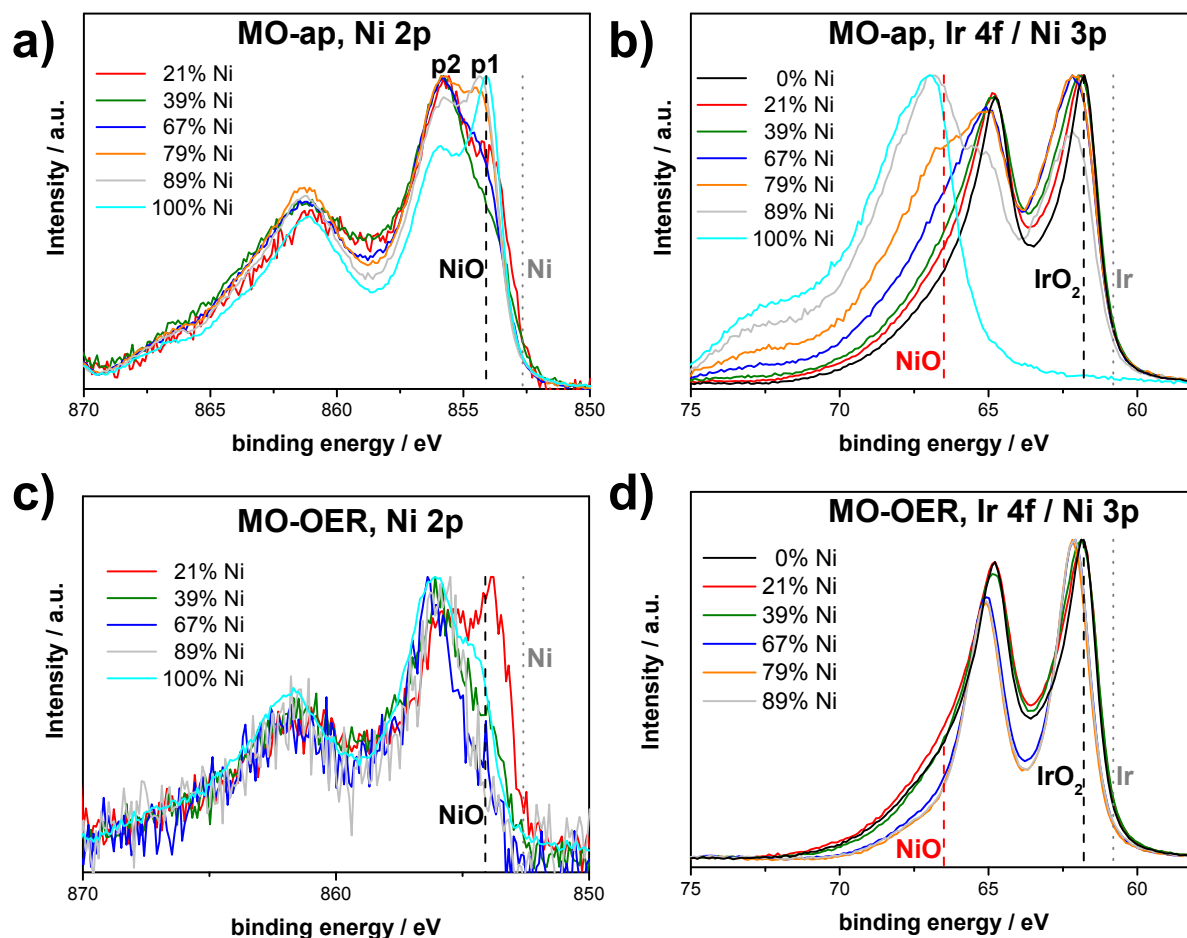


Figure 38: X-ray photoelectron spectra provided together with reference binding energies. Ni 2p region measured on as prepared (MO-ap, a) and electrochemically treated (MO-OER, c) Ir-Ni oxide films. Ir 4f and Ni 3p region measured on as prepared (MO-ap, b) and electrochemically treated (MO-OER, d) films. Reference binding energies: Ir⁹⁷, IrO₂⁸⁴, Ni⁹⁸ and NiO⁹⁹.

For the MO-ap catalyst films, Ir XPS studies are somewhat complicated to analyze due to the overlap of Ir 4f and Ni 3p signals, see Figure 38b. The spectra of the Ni leached MO-OER catalysts, however, are largely dominated by Ir, see Figure 38d. The as-prepared pure Ir oxide film showed an Ir 4f doublet with an asymmetric peak shape and a binding energy coinciding a value previously observed for IrO₂⁸⁴. As recently pointed out by Kahk et al., the asymmetric peak shape is due to final state screening and, therefore, to the metallic character of IrO₂; however, the actual screening process is not yet fully understood.¹⁰⁰ In order to obtain more detailed chemical information about Ir in MO-ap and resolve Ir from Ni signals, extensive curve fitting was applied (see Figure 60 and Figure 61). Unlike pure Ir oxide, the 4f peak width of the MO-ap increased with

increasing Ni content and required a second Ir component in order to obtain a reasonable fit quality. Note that without this second Ir 4f component it was not possible to account for the doublet area ratio. The increased peak width indicated a variation in the local surroundings of the Ir centers due to perturbation of Ir oxide by Ni. Upon Ni leaching, the signal width decreased supporting this interpretation. Interestingly, beside the width, the line shape of the Ir 4f signals in MO-ap and MO-OER samples differs depending on the initial Ni content, which can be traced directly in Figure 38d for MO-OER or, respectively, in the fits (see Figure 60) for MO-ap. For low initial Ni contents ≤ 39 at% in MO-OER the Ir signals are characterized by a pronounced asymmetry, which is reduced at higher initial Ni contents. Since the peak asymmetry is related to the metallic character the reduced asymmetry indicates a reduced metallic character. Although Ni was leached out to a large extent, the asymmetric line shape of IrO₂ did not reemerge in the leached MO-OER catalysts with initial Ni contents ≥ 67 at%.

The O 1s spectra of the catalysts prior and after OER testing are depicted in Figure 39. Fits of the O 1s spectra (Figure 62 and Figure 63) revealed up to 4 different oxygen species at about 529.2, 529.9, 531.4 and 533.1 eV. The species at ~ 533.1 eV can be assigned to adsorbed water, whereas the species at 529.9 eV and 531.4 eV are related to lattice oxygen and hydroxyl groups, respectively.^{101,102} The species at 529.2 eV appeared with mixed oxides, being particularly visible in 21%Ni-MO, and our DFT calculations indicated that lattice oxygen atoms bridging Ir and Ni atoms have an O 1s binding energy in this range. The binding energy of lattice oxygen in these metal oxides is a weak function of the Ni content, and thus that of pure NiO is located at 529.6 eV. Figure 40a depicts the fraction of surface hydroxyl species (OH-fraction) to the surface oxide related species (OH and both lattice oxygen species). In MO-ap the OH-fraction was just a weak function of the Ni content. Interestingly, after Ni leaching and OER catalysis the OH fraction increased depending on the initial Ni content. Pure Ir oxide showed almost no change in the OH fraction, while films with higher initial Ni contents showed an increased OH fraction. The OH fraction of MO-OER films increased with increasing initial Ni, until a value close to 100 % was reached for 67%Ni-MO-OER. Similar to XAS measurements for MO-OER, no OH fraction could be obtained for 89%Ni-MO-OER and the pure Ni oxide film due to the detection of Ti oxide.

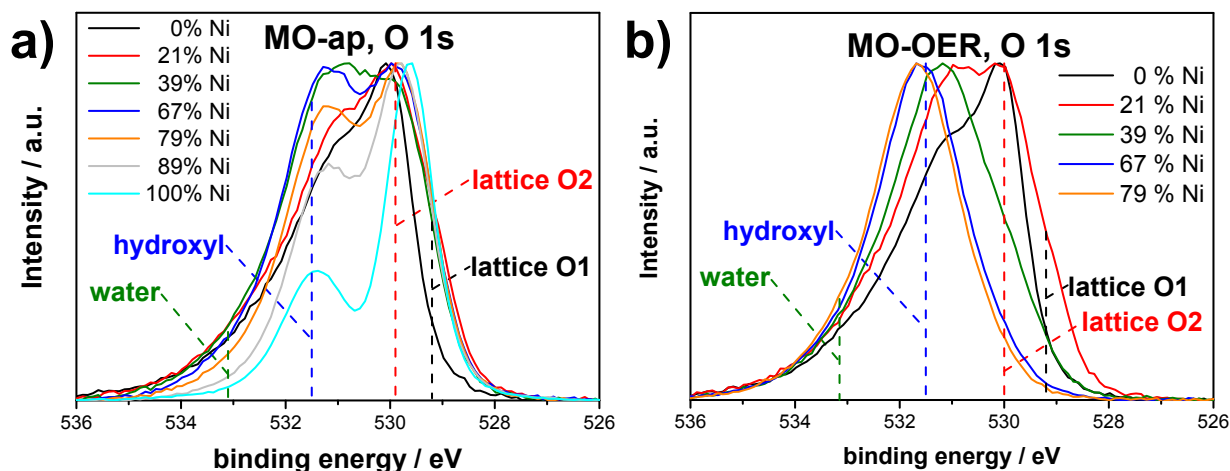


Figure 39: X-ray photoelectron spectra of the O 1s region of MO-ap and MO-OER provided together with reference binding energies from ¹⁰².

5.5 The surface electrochemistry of Ir-Ni mixed oxide catalysts

To get insight into the surface electrochemical redox processes, cyclic voltammetry (CV) was measured within the OER protocol after the first OER polarization curves (OER scan 1). Figure 40b evidences dramatic changes in the surface electrochemistry with initial Ni content. While pure Ir oxide exhibited its characteristic reduction feature close to 0 V followed by an indistinct broad redox wave between 0.4 V and 1.4 V^{30,102,103}, higher Ni contents resulted in the disappearance of the reduction feature, yet associated with a new distinct redox feature around 0.8 V. At Ni contents ≥ 67 at%, this feature was accompanied by a low-potential shoulder. Interestingly, these features are commonly observed for *electrochemically prepared* so called *hydrous* Ir oxides, where the main peak at ~ 0.8 V could be attributed to the Ir(III)/Ir(IV) transition.^{15,16,49} Overall, the thermally prepared Ir-Ni mixed oxide catalysts with initial Ni contents ≥ 39 at% displayed a surface redox chemistry that was much more similar to electrochemically prepared than to thermally prepared Ir oxides. In Figure 40c the oxidation peak potentials of Ir(III)/Ir(IV) are plotted for each catalyst over its initial Ni content. Clearly, the Ir redox potential strongly correlates with the initial Ni content, evidencing an anodic shift in redox potential (for ≥ 39 at% Ni), indicating a stabilization of the lower relative to the higher Ir oxide.

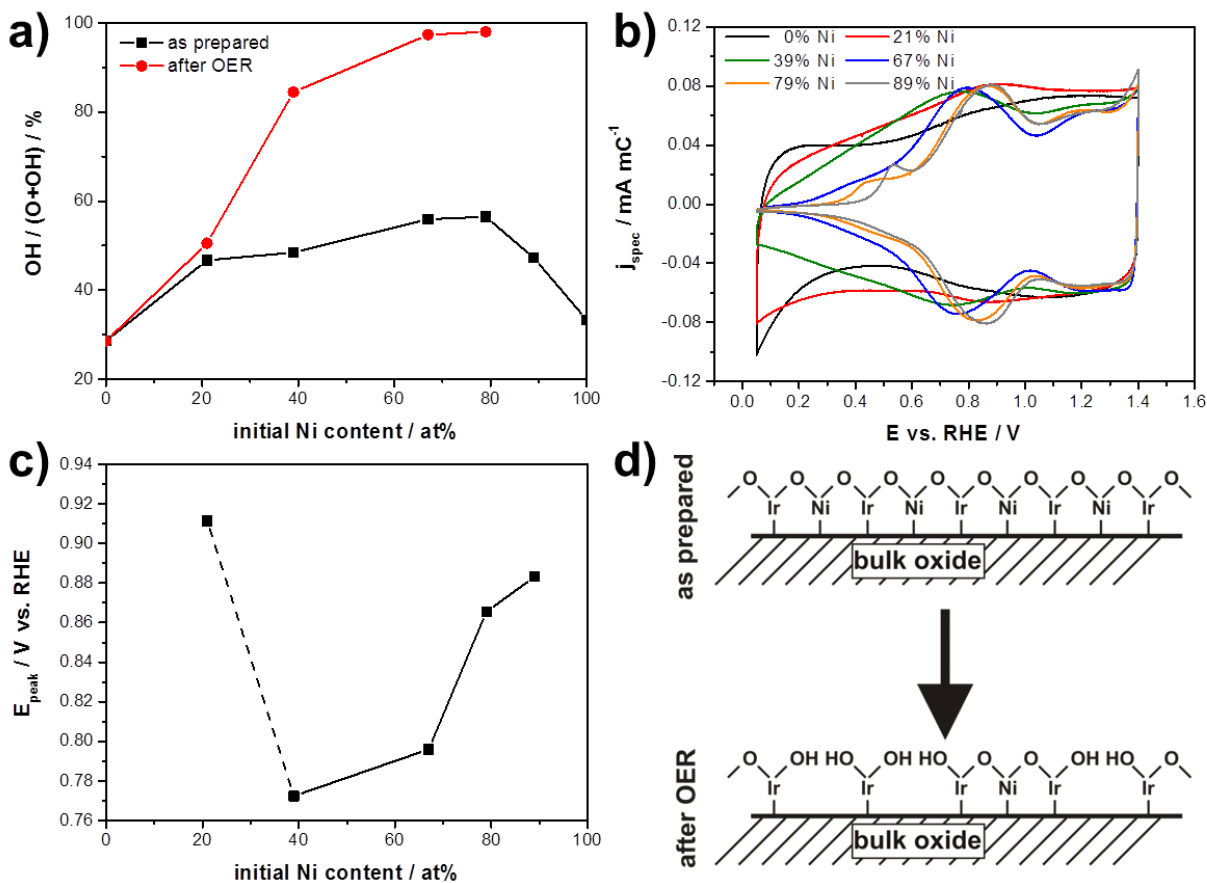


Figure 40: *a) Hydroxyl group (OH) fraction to the total oxide related oxygen (hydroxyl groups and both lattice oxygen species) as determined by XPS. b) Cyclic voltammetry measured with 50 mV s^{-1} . The current was normalized to q^* (reflecting the electrochemical active oxide surface area) c) Potential of the anodic peak observed in b). d) Model of Ni leaching from the surface of Ir-Ni mixed oxides.*

5.6 Structure-reactivity correlations and catalytic performance descriptors

The goal of the present study is a deeper understanding of the OER catalysis on Ir-Ni mixed oxide model catalysts, which will aid in the development of improved PEM electrolyzer and PEC anodes. To achieve this goal we strive to identify microscopic and macroscopic parameters that control the electrocatalytic activity and stability of the Ir-Ni oxide catalysts. For that purpose we established correlations between the trends in structure, activity, and stability.

First we address the role of Ni as a sacrificial catalyst component and the implication of Ni leaching for the active catalyst structure. The prepared MO-ap films were predominantly single phase homogenous Ir-Ni mixed oxides. Ni was leached from these oxides during the electrocatalytic OER protocol, yielding in Ir-rich oxides. As a result, the tested MO-OER films became more porous, and, on an atomic scale, the binding environment of oxygen was significantly altered. In this Ni-depleted catalytically active state, the remaining Ir-rich oxide must react structurally to compensate the Ni loss. A schematic hypothetical model for this is provided in Figure 40d, which helps to rationalize the geometric, compositional and electronic transformations during the catalyst leaching and activation.

When Ni is leached from MO-ap films, oxygen atoms lose binding partners, which is expected to weaken the binding strength of the Ni-depleted oxygen atoms to the oxide lattice. To further assure electroneutrality, the Ni-depleted oxygen atoms will take up protons from the electrolyte and, thus, form surface hydroxyl groups, as indicated in Figure 40d. Indeed, upon Ni leaching the surface OH fraction increased significantly up to 67 at% initial Ni content (Figure 40a). Importantly, the surface-specific OER activity revealed a rather similar trend as the OH fraction: Both increase with increasing Ni content and reach saturation at 67 at% Ni. Thus, we conclude that the ratio of weakly-bonded surface hydroxyls is directly related to the surface specific catalytic OER activity of Ir oxides. This trend becomes intuitive if surface OH groups are assumed to act as reactive surface intermediates on active sites of the catalytic process.

To put our conclusions in the context of a chemical reaction mechanism we refer to a recent OER reaction model⁵⁷. This mechanism puts forward the water-assisted stepwise deprotonation of hydroxyl groups forming reactive peroxide species, which are then released from the active site to form molecular oxygen. The overall process was predicted to proceed at a reasonable rate only if the surface intermediates, including hydroxyl groups, display a balanced binding to the oxide lattice. Lattice oxygen binds too strongly and was therefore not predicted to participate directly in the OER process. Our findings are in line with results by Fierro et al. that part of the evolved oxygen actually originates from the Ir oxide catalyst itself, most likely through involvement of its loosely bound surface hydroxyls.⁶¹ Although hydroxyl groups are expected to have lower

binding strengths than lattice oxygen atoms, their binding may vary with local coordination. Still, the OH groups with optimal binding energy would always dominate the overall reaction rate. Implications for changes of the oxygen binding strength were found by XAS at the O K-edge and CV.

In regard of possible Ni-related oxide lattice geometry and strain effects, it is pointed out that a strong increase in the surface specific catalytic OER activity occurred at essentially constant residual Ni contents of about 12 at% Ni in the active oxide films (for initial Ni contents ≤ 67 at%). This is in contrast to Ni-leached bimetallic PtNi alloy catalysts where residual subsurface Ni atoms gave rise to surface lattice strain effects on the catalytic activity.¹⁰⁴ It can be therefore concluded that the residual near-surface Ni ratio is not a suitable quantitative descriptor for OER activity, and oxide lattice strain effects are likely of limited significance. This conclusion does not preclude that the presence of some residual Ni may be critical to structurally support the active films. The fact that 79%Ni-MO still exhibited improved intrinsic OER activity over pure Ir oxide although the residual Ni content was far below 12 at% suggests further evidence for the critical role of the formation and presence of specific and possibly reactive oxygenated surface species.

Finally, the stability against dissolution of surface Ir ions in the mixed oxide lattice depends plausibly on the strength and the number of Ir-O-M (M: Ir or Ni) binding motifs. Following our schematic model in Figure 40d, the number of such motifs in catalytically active Ir-enriched MOs decreases with higher initial Ni content, as more Ni atoms can and will be leached out. Thus, Ir dissolution should increase with initial Ni content. Indeed, this trend was observed experimentally. We conclude and predict that a stable and active Ir oxide water splitting OER catalyst combines the highest possible number of reactive surface hydroxyl groups with the highest possible number of intact Ir-O-M binding motifs in the sub-surface.

5.7 Conclusions

Mixed bimetallic oxides offer great opportunities for a systematic tuning of electrocatalytic activity and stability. This is exemplified here using well-defined thermally prepared Ir-Ni oxide thin-films catalyzing the oxygen evolution reaction under acidic conditions similar to PEM electrolyzers or PEC devices. First, it was shown that Ir-Ni mixed oxides offer an unprecedented 20 fold improvement in Ir mass-based water splitting OER activity over state-of-art pure Ir oxide catalysts. Similarly, activity improvements were observed on a geometric as well as on an active surface area basis.

Beyond the activity improvement much emphasis has been placed on a more fundamental characterization and description of the catalysts, their performance and their Ir stability. To this end, we have studied the geometric, electronic, and morphological structure of the various Ir-Ni mixed oxide catalysts. We accomplished a number of novel correlations between activity and stability and microscopic descriptors and managed to reject others such as Ni-related geometric strain effects.

Our data and analysis have resulted in a simple, yet intuitive model for the formation of the active state of the catalytic surface. The model suggested that the coverage of reactive surface hydroxyls serves as a useful descriptor for OER activity. Formed by initial Ni dissolution and disruption of Ir-O-M motifs, the surface hydroxyls showed a reduced binding to the oxide lattice, which was conducive to catalytic activity. Though stability of Ir atoms was compromised in this process as well, surface normalized dissolution of Ir did not correlate with catalytic activity, suggesting – contrary to common believes - that a separate optimization of activity and stability may actually be possible. It was further established that thermally-prepared yet Ni-leached Ir-Ni oxide film catalysts exhibited compositional stability and surface electrochemical redox characteristics that closely resembled those of Ir oxides formed via electrochemical oxidation of metallic Ir surfaces. Hence, it was demonstrated how to balance catalytic activity advantages of oxidized metals with stability benefits of thermally prepared bulk oxides.

In more general terms, this study highlights the opportunities offered by Ir-Ni bimetallic oxides to tune their catalytic stability and electrolytic activity at anodes in highly corrosive acidic environments.

6 OER performance comparison: Ir-Ni mixed oxides versus pure Ir oxide films calcined at different temperatures

In the last chapters two different approaches for the optimization of the OER performance of Ir oxides have been described, namely the formation of binary Ir-Ni mixed oxides and the variation of the calcination temperature. So far, both approaches were comprehensively studied in separate chapters requesting for a comparative evaluation of the results which is provided in the following. Within this comparison, OER performance data of an electrochemically prepared Ir oxide (prepared by electrochemical oxidation of metallic bulk Ir cylinder) will be provided for comparison.

Here, the electrochemical Ir oxide was grown on a polished bulk Ir electrode by 500 potential cycles with 500 mV s^{-1} between 0.05 and $1.4 V_{\text{RHE}}$, as shown in Figure 41a. Whereas the first cycle reveals a cyclic voltammogram common for metallic Ir electrodes¹⁵ the higher cycle numbers clearly show the evolution of a "hydrous" electrochemical Ir oxide film (EChem-IrOF) traceable mainly by peak p1.2 and its cathodic counterpart. Peak p1.2 is commonly attributed to the Ir(III)/Ir(IV) redox couple of hydrous Ir oxide.¹⁵⁻¹⁷ In contrast to that the origin of peak p1.1 is not unambiguous. However, p1.1 becomes more pronounced with increasing cycle number and is hence related to the EChem-IrOF as well. The growth of the oxide related peaks p1.1 and p1.2 demonstrates that the EChem-IrOF is growing with increasing cycle number, in accordance with previous results^{16,17}. In contrast to that, the redox peaks below $0.35 V_{\text{RHE}}$ are assigned to hydrogen under potential deposition (Hupd) and are thus related to metallic Ir suited below the EChem-IrOF.^{15,16} The metallic Ir below the EChem-IrOF remains accessible for the electrolyte and, hence, electrochemically active due to the porosity of the EChem-IrOF.¹⁶ This explains why the Hupd peaks do not grow with increasing cycle number. In accordance with these assignments the Hupd is absent for the thermally prepared 79%Ni-MO film (Figure 41b). However, the oxide related peaks of EChem-IrOF and 79%Ni-MO are astonishingly similar. These similarities in surface redox chemistry indicate structural similarities in both oxides. With respect to its geometric OER activity the EChem-IrOF is suited rather in the middle between the

highest (67%Ni-MO) and lowest activity OER (IrOF(450°C)) of Ir-Ni mixed oxides, see Figure 42.

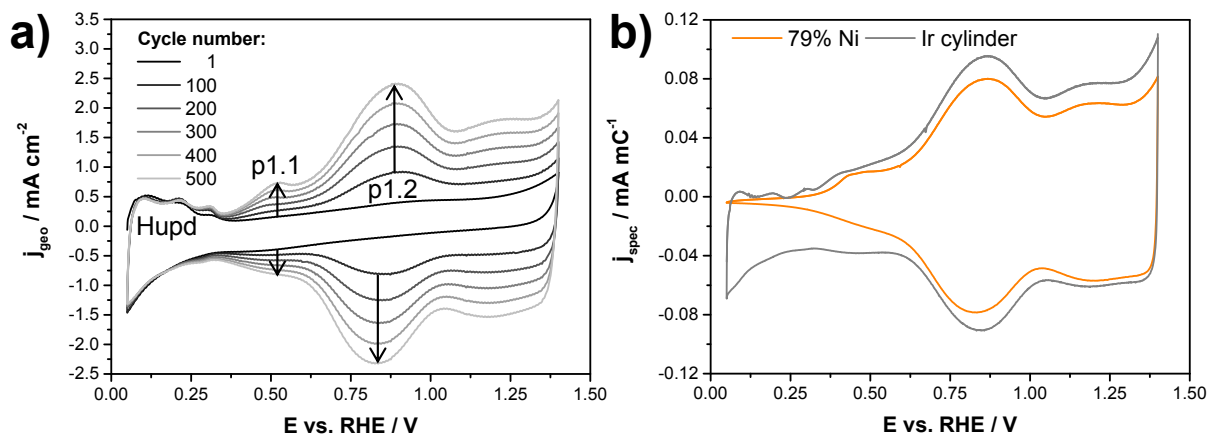


Figure 41: *a) Electrochemical Ir oxide formation on a polished metallic Ir electrode by cyclic voltammetry (500 mV s^{-1} , 0.1 M HClO_4 (N_2 degassed), 0 rpm , room temperature) performed as an additional first step prior to the OER protocol. b) Cyclic voltammetry of the electrochemically formed Ir oxide and 79%Ni-MO measured within the OER protocol after OER Scan 1 with 50 mV s^{-1} in 0.1 M HClO_4 .*

The OER activity in form of the current density at 300 mV overpotential ($1.530 \text{ V}_{\text{RHE}}$) is plotted in Figure 42 for the activity comparison of the different Ir oxides. Here, OER scan 2 was used to evaluate the OER activity of MOs and IrOFs, since Ni leaching potentially influences the OER activity measurement in OER scan 1 for MOs. As mentioned before, OER scan 1 and 2 yield similar trends for the OER activity of IrOFs. However, for a comparison always the same scan should be used, since the absolute values differ (see section 4.3).

It is clearly evident from Figure 42 that IrOF(250°C) and IrOF(350°C) provide rather similar geometric OER activities which are suited slightly above the geometric activity maximum of MOs, provided by 67%Ni-MO. It should be noted that the pure Ir oxide film in the MO series and IrOF(450°C) constitute equivalently prepared samples from different sets of measurements. The observed similarity in OER activity for these samples is, therefore, expected and proves the reproducibility of the measurement and the synthesis.

Albeit the geometric OER activity of Ir oxide calcined at 450°C was largely improved by intermixing with Ni it did not reach the value achieved by IrOFs calcined at 250°C and 350°C. However, for Ir-Ni mixed oxides a substantial fraction of Ir was substituted by Ni and thus the surface specific and the mass based OER activity provide a better comparability than the geometric OER activity. Considering the Ir mass based OER activity, the high Ni content MOs (67%, 79%) double the highest mass based activities obtained for IrOFs (IrOF(250°C) and IrOF(350°C)) (see Figure 43a).

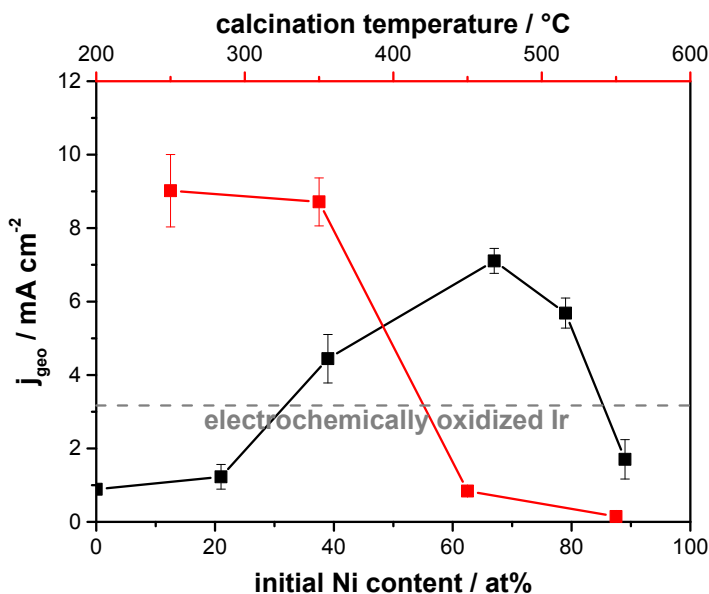


Figure 42: Geometric OER current density obtained at 300 mV overpotential ($1.530 V_{\text{RHE}}$) from OER scan 2 for Ir oxide films calcined at different T , Ir-Ni mixed oxides and electrochemically oxidized Ir.

Compared on a surface specific level (see Figure 43b) the maximal OER activities of both, the IrOFs and the MOs, reveal similar values of $\sim 0.8 \text{ mA mC}^{-1}$, for high Ni contents (67%-89%Ni) or, respectively, low calcination temperatures (350°C). The observation of a rather similar maximal specific OER activity within different optimization approaches indicates that this value might constitute the global maximum for thermally prepared Ir oxides. However, the EChem-IrOF shows an even slightly higher surface specific OER ($\sim 1 \text{ mA mC}^{-1}$) than the maximum observed for thermally prepared Ir oxides.

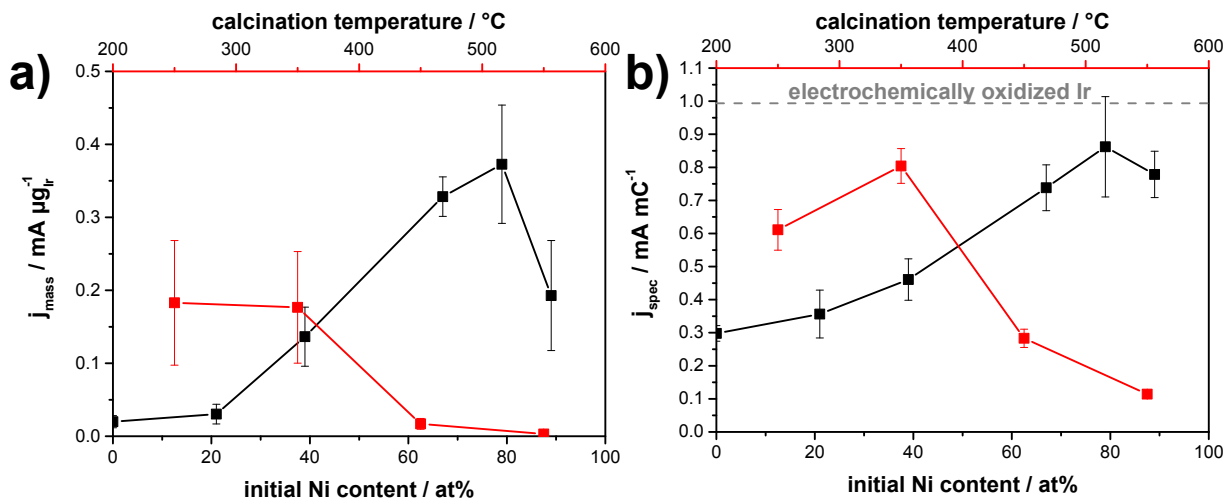


Figure 43: *Ir* Mass based (a) and surface specific (b, based on q^*) OER current densities obtained at 300 mV overpotential ($1.530 V_{\text{RHE}}$) from OER scan 2 for *Ir* oxide films calcined at different T , *Ir*-*Ni* mixed oxides and electrochemically oxidized *Ir*.

In contrast to the OER activity, the stability of metallic *Ir* against dissolution was by far the lowest observed here (see Figure 44). For metallic *Ir* a comparably huge *Ir* dissolution rate can be initially observed when stepping into the OER, which contributes strongly to the integral value plotted in Figure 44. Even if this initial *Ir* dissolution is neglected and only the steady state value at the end of the step is considered, the *Ir* dissolution rate of the metal is still 1.7 times bigger than the highest steady state value observed for MOs, although the active surface area of the porous MO-OER can be considered to be much bigger than that for the dense metallic *Ir* electrode. In this context it should be stated that the *Ir* electrode used for the stability test was not oxidized by electrochemical cycling.

Generally, the IrOFs showed a higher *Ir* dissolution stability than the MOs, as apparent from Figure 44. Whereas the *Ir* dissolution remained comparable for MOs $\leq 39\% \text{Ni}$ and IrOFs calcined at 250 and 350°C, higher Ni contents yielded in higher *Ir* dissolution and, hence, increased the difference between IrOFs and MOs. The least stable MOs more than doubled the amount of dissolved *Ir* observed for the least stable IrOF. In this context, it should be stated that the IrOFs were measured in the as prepared state whereas the dissolution of MOs was measured on samples that underwent the OER protocol (MO-OER). However, this difference in the measurement appears to have no

influence on the result, since similar amounts of dissolved dissolution were measured for the pure Ir oxide film in both series (IrOF and MO).

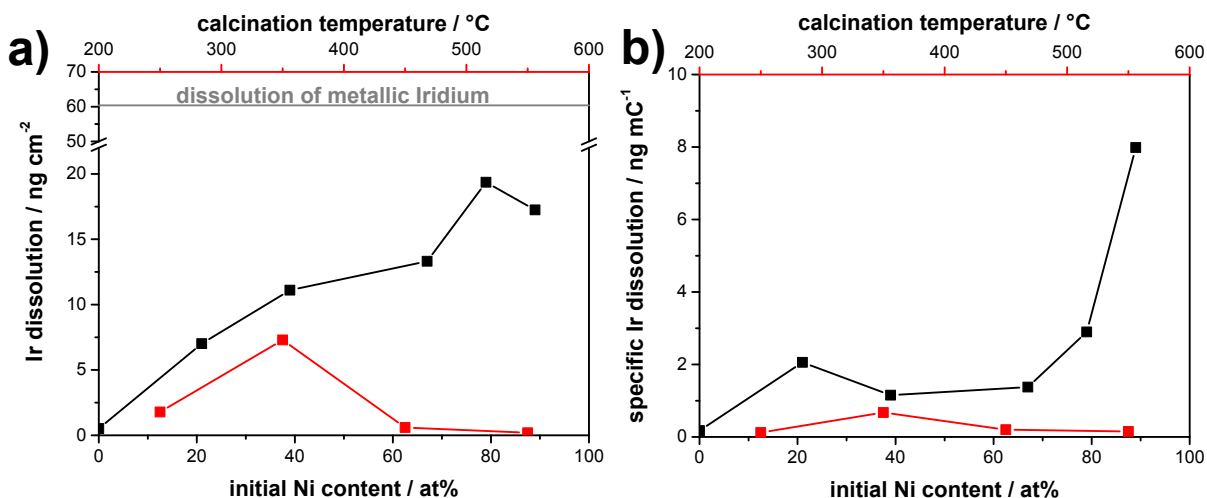


Figure 44: *Ir amount dissolved during 10 min OER at 1 mA cm^{-2} measured by PR-ICP-MS normalized to the investigated geometric surface area (a) or, respectively, q^* representing the electrochemically active surface area of Ir oxide (b). The measurements were performed for Ir oxide films calcined at different T , Ir-Ni mixed oxides and a metallic Ir electrode.*

Similar to the geometric Ir dissolution stability, the surface specific normalization of the dissolved Ir amounts shows that MOs provide a lower stability than the IrOFs. The surface specific Ir dissolution shows a plateau at intermediate Ni contents, as pointed out before (see section 5.1). In the plateau region the stability of MOs is only slightly lower than for the least stable IrOF, which was IrOF(350°C). However, the IrOF(250°C) offered an almost similar surface specific OER activity as IrOF(350°C) but a much smaller surface specific Ir dissolution rate. Compared to this IrOF the MOs in the plateau region yield substantially lower surface specific stabilities.

6.1 Conclusion

In the context of OER activity and Ir utilization the MOs outperform the pure IrOFs yielding a two times higher Ir utilization. However, when it comes to Ir dissolution stability, it is just the opposite; IrOFs provide lower dissolution rates than MOs. The best compromise of both, OER activity and Ir dissolution stability, is provided by the IrOF(250°C), which shows an Ir utilization half as high as the maximal MO and an exceptional stability.

The OER performance of IrOF(250°C) with respect to activity and stability can be understood based on the model invoked within the MO study. According to the model, a large fraction of OH surface groups is required to ensure a high OER activity. The low calcination temperature of IrOF(250°C) ensures that a large fraction of surface OH groups is present, whereas their fraction is reduced at higher calcination temperatures. Hence, the model explains the high OER activity of IrOFs calcined at low temperatures. Considering the stability the model predicts that a large number of metal-oxygen-metal (M-O-M) motifs is advantageous. Unfortunately, this aspect was not studied for IrOFs. But it appears plausible that there are more M-O-M motifs in a pure than in a Ni-leached Ir oxide, since in the latter case vicinal metal partners are dissolved which is believed to reduce the amount of M-O-M motifs.

7 In-situ detection of surface species during the OER using shell isolated nanoparticle enhanced Raman spectroscopy

7.1 Introduction

Having obtained improved understanding of the material properties of Ir oxide that determine OER activity and Ir stability, the following section will provide direct new insights into mechanistic aspects of the OER pathway by an in-situ spectroscopic approach. As explained in section 1.4 the OER mechanism still remains uncertain although the OER as anodic reaction of electrocatalytic water splitting is known since 1789.⁵⁴ As long as the mechanism remains uncertain, the actual reasons for the catalytic overpotential in the OER remain uncertain. Thus, the basis for a rational knowledge-based optimization of the OER activity of a catalyst is missing. This underlines the need for in-situ spectroscopic insights under reaction conditions.

Due to the harsh acidic corrosive OER reaction conditions and the inherent high electrode potentials combined with the presence of large quantities of water, most in-situ surface confined analytical methods – electron and photon based - are not appropriately applicable. However, surface enhanced Raman spectroscopy (SERS) has proven its excellent applicability for the study of OER surface species on roughened gold electrodes, which resulted in the identification of an OOH surface species during the OER.^{54,55} However, this approach is limited to nano-structured metal electrodes that provide a locally enhanced radiation field at the metal-dielectric interface by resonant coupling of light with the surface plasmons of the metal.¹⁰⁵ Thus, Au is an excellent SERS substrate but it is unfortunately not a highly active OER catalyst, since the OER on gold proceeds with significant rates only at and above $\sim 2 V_{\text{RHE}}$, whereas highly active OER catalysts like Ru and Ir oxide already evolve oxygen below $1.5 V_{\text{RHE}}$.^{13,15,54,103} Furthermore, Ru and Ir oxide appear not to obey the oxide decomposition OER mechanism (see section 1.4 for details) identified for Au.^{54,61,62,106} Thus, spectroscopic insights obtained on gold may not be transferrable to highly active benchmark OER catalysts like Ru and Ir oxide.

On the other hand, metal oxide OER catalysts do not exhibit plasmon-induced surface enhancement impeding SER spectroscopic analysis. Fortunately, this limitation can be overcome placing resonant plasmonic noble metals as optical amplifiers in close vicinity to the interface of interest.^{107,108} However, to use such an approach for studying OER reaction intermediates at the inherent high electrode potentials it has to be guaranteed that the noble metal amplifiers are electrochemically inert within the investigated potential range and do not form potential-dependent oxide species. On benchmark OER catalysts the OER commences with significant rates above $1.4 V_{\text{RHE}}$ ^{10,12} and hence the potential range of interest extends at least up to $1.4 V_{\text{RHE}}$ and preferably a few hundred mV above. However, even the noblest metal Au forms surface oxides/hydroxides already around 1.3 V.^{54,55} Oxidation of the noble metal optical amplifier may affect the surface enhancement and, more importantly, evoke additional Raman signals as observed for Au.^{54,55} For instance, the presence of OOH species on Au can potentially impede the detection of similar intermediates on benchmark OER catalysts. Fortunately, metal oxidation can be avoided applying a technique called shell-isolated nanoparticle enhanced Raman spectroscopy (SHINERS).^{65,109} In this approach, Au nanoparticles (NPs) are coated with a very thin silica shell retaining most of their electric field enhancement but avoiding electric contact to the electrode.^{65,109} Due to the absence of the electrical contact, electrochemical oxidation of Au is inhibited. Within this approach optical amplifiers and the OER catalyst are synthesized separately and, thus, virtually every heterogeneous OER catalyst can be investigated.

In the following, the SHINERS approach is applied to study surface confined processes during the OER on a thin-film Ru oxide model catalyst, the preparation of which was widely similar to the Ir and Ir-Ni oxide catalysts presented in the previous chapters. Here, thermal Ru oxide was chosen to obtain mechanistic insights because it is the most active PEM OER catalyst that is stable enough to be investigated by in-situ SHINERS. A novel electrochemical in-situ cell with minimized optical losses but optimized electrochemical reaction conditions was designed to obtain high quality Raman spectra under OER reaction conditions.

7.2 Characterization of the RuO₂ thin-film catalyst

The Ru oxide thin-film catalysts applied for the in-situ SHINERS study were synthesized similar to the Ir oxide films by spin-coating of an acetate based precursor solution onto a Ti substrate. The precursor film is then thermally converted into the oxide by calcination in air. However, different to the synthesis of Ir oxide films, Ru acetate was first decomposed at low temperature (250°C) in air and then crystallized in inert argon atmosphere at 400°C to obtain a fine crystalline film with a high degree of crystallinity. Crystallinity and present phases were analyzed by GI-XRD (see Figure 45).

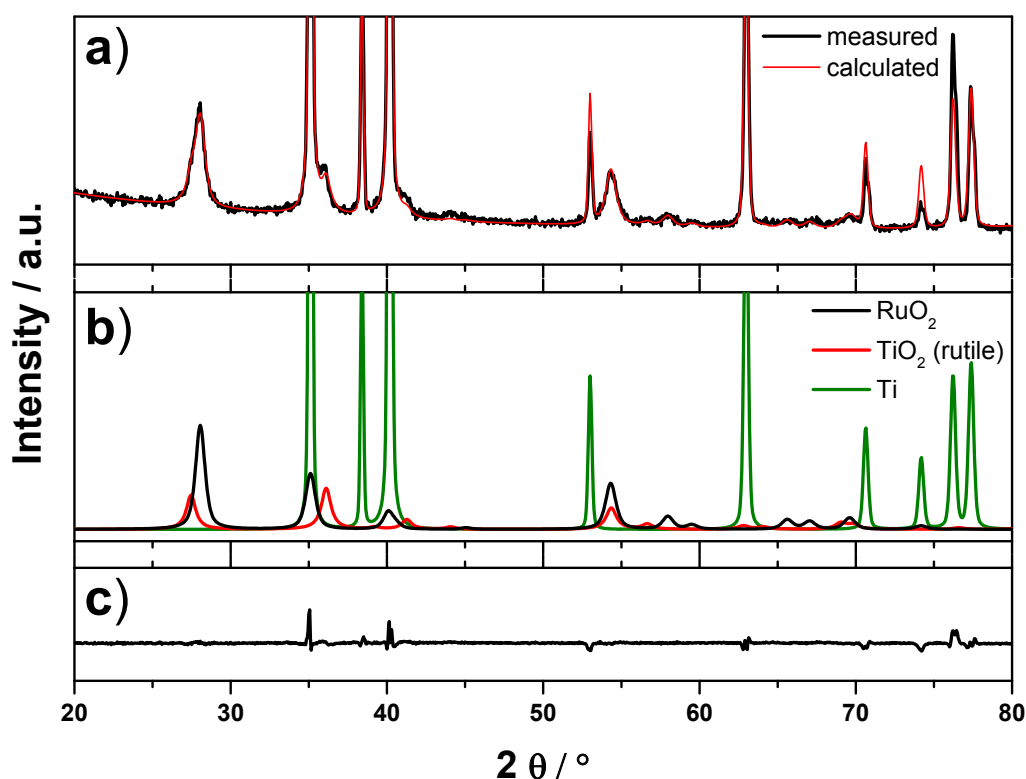


Figure 45: *Grazing incidence X-ray diffraction measurement of a RuO₂ thin-film catalyst on a Ti cylinder together with results from Rietveld refinement. a) Measured and calculated diffraction pattern, b) separate contribution of components used within the refinement and c) difference between measured and calculated diffraction pattern.*

Rietveld refinement revealed the presence of two separate rutile-type phases, attributed to RuO₂ and TiO₂, and a hexagonal phase dedicated to the metallic Ti substrate (Figure 45b and Table 4). The quality of the refinement was principally high (GOF: 2.67), only

some reflections of the metallic Ti substrate were not perfectly described. Although the analysis is complicated by the close similarity of RuO_2 and TiO_2 , as well as the overlap of some RuO_2 reflections with Ti reflections, the presence of a shoulder of the Ti (010) reflection at about $35^\circ 2\theta$ towards higher diffraction angles clearly demonstrates the presence of a TiO_2 phase separated from the RuO_2 phase. The lattice parameters of all included phases (RuO_2 , TiO_2 and Ti) were fixed to the reference values and, thus, not included in the refinement. Since a good refinement quality could be obtained without changing the lattice parameters an extensive intermixing between RuO_2 and TiO_2 appears unlikely. Based on the line broadening analysis crystallite sizes of ~ 13 and ~ 19 nm were obtained for TiO_2 and RuO_2 , respectively.

Morphology and film thickness of the RuO_2 film were studied by SEM as depicted in Figure 46.

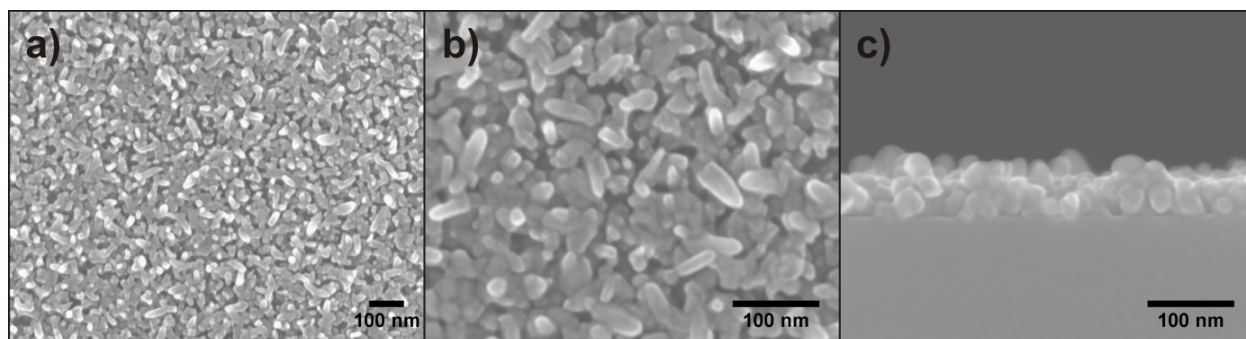


Figure 46: *Scanning electron micrographs of a RuO_2 thin-film. Figure a) and b) show top-view images with different magnifications (substrate: Ti cylinder) and Figure c) shows a cross-section micrograph (substrate: Si wafer).*

In accordance with the diffraction data the film is composed of RuO_2 nanocrystals bigger than those obtained for the Ir oxide films (compare section 4.1.1.1). Although the nanocrystals are homogeneously distributed on the substrate, some small voids are apparent, due to the rather big crystallite size. The cross-section image depicted in Figure 46c shows similarly the rather large crystallite size and reveals a film-thickness of about 50 nm.

7.3 Characterization of silica coated gold nanoparticles

The silica shell thickness of silica-coated gold nanoparticles ($\text{Au}@SiO_x$) was optimized to achieve the highest possible electric field enhancement. Therefore, the reaction time at 90°C during the synthesis of $\text{Au}@SiO_x$ was varied from 30 to 120 minutes (see Figure 47). Although the measured shell thickness has a rather large standard variation compared to the average value, the average shell thickness clearly increases linearly with the reaction time. Thus, the shell thickness can be adjusted based on the reaction time in the low nm range.

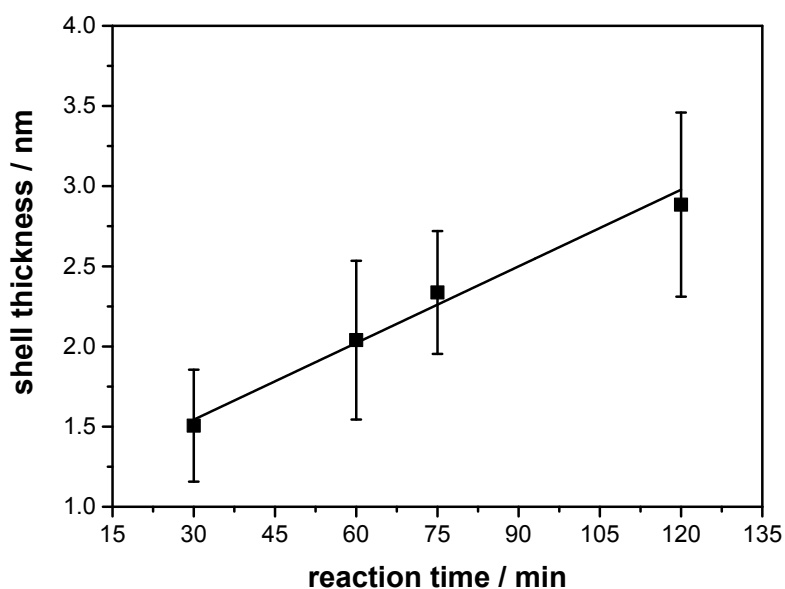


Figure 47: Average silica shell thickness and related standard deviation of $\text{Au}@SiO_x$ nanoparticles obtained for different reaction times at 90°C as measured by TEM.

To evaluate the coverage of the silica coating for the shortest reaction time (30 min), cyclic voltammetry of pristine Au and $\text{Au}@SiO_x$ NPs was measured (Figure 48). Uncoated Au NPs show oxidation and reduction peaks characteristic of polycrystalline gold surfaces.⁵⁴ However, for $\text{Au}@SiO_x$ NPs these features largely disappear demonstrating that, despite the thin coating, the silica shell covers the particles almost completely. Based on the Au oxide reduction charge (determined by integration of the Au reduction peak), which is a common measure for the active gold surface area,¹¹⁰ only 0.6 % of the particles surface area remained electrochemically addressable. If the shell thickness was increased extending the reaction time, still a certain small fraction of the

gold surface remained electrochemically addressable (CV not shown). Thus, the smallest shell thickness (reaction time 30 min) obtained here is used for further experiments, since the principle problem of a small addressable gold surface fraction remained for all tested shell thicknesses and, therefore, has to be tackled - as will be shown later - in any case.

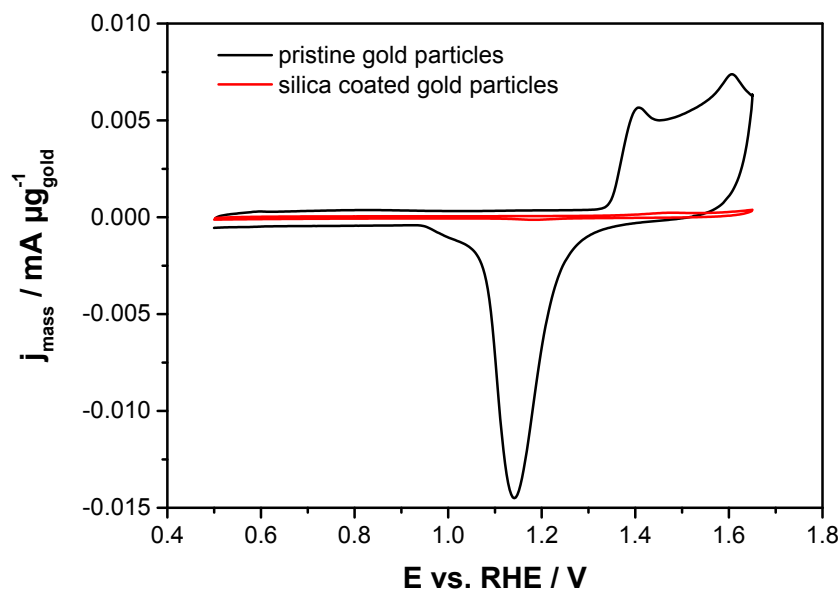


Figure 48 : *Cyclic voltammetry of pristine and silica coated (30 min reaction time) gold NPs measured with 50 mV s^{-1} in $0.05 \text{ H}_2\text{SO}_4$. The current was normalized according to the applied gold mass.*

Figure 49 shows exemplarily a TEM micrograph of an Au@SiO_x nanoparticle. The silica shell (grey) with a thickness $\leq 2 \text{ nm}$ can be identified around the gold particle of $\sim 50 \text{ nm}$ diameter. The Au@SiO_x NPs were deposited onto the RuO₂ film adopting a Teflon coating ring (see Figure 6) which was pressed onto the RuO₂ surface. An aliquot of the Au@SiO_x NP suspension was then pipetted into the Teflon coating ring and subsequently dried in vacuum. The Teflon coating ring allows for controlling the shape of the water-air interface which is a key parameter for the formation of particle arrays from suspensions.⁶⁶ Thereby, a rather homogenous distribution of Au@SiO_x NPs was obtained on the RuO₂ film (see Figure 49c and d). This is because the suspension dries from the middle to the outside, if a Teflon coating ring is used, and not the other way around.⁶⁶

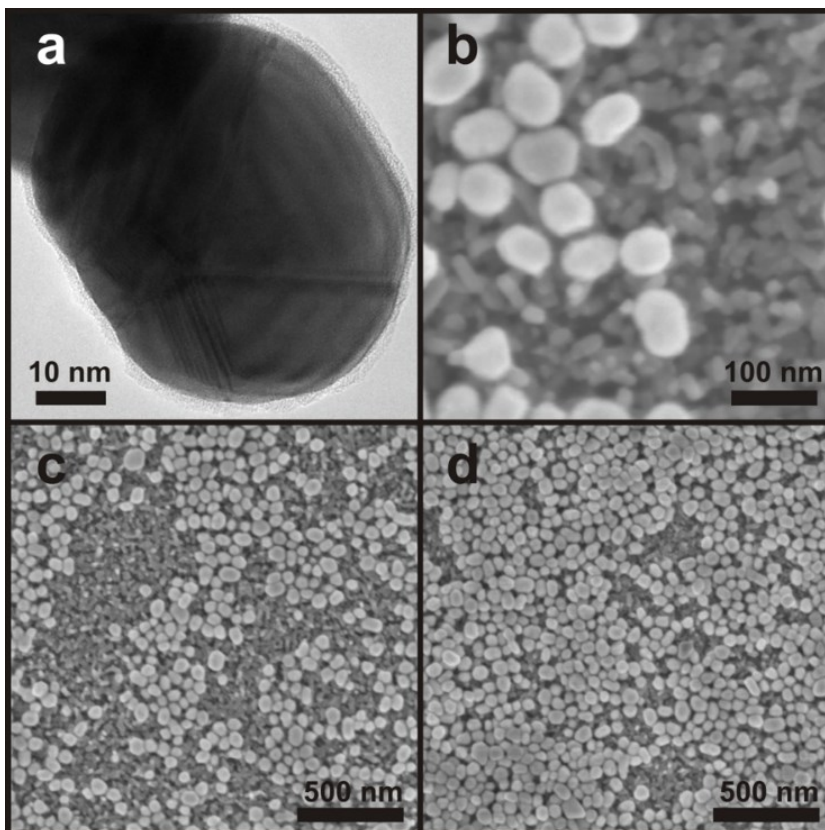


Figure 49: *TEM micrograph of a silica coated gold ($Au@SiO_x$) nanoparticle (a). SEM micrographs of $Au@SiO_x$ NPs applied on top of the RuO_2 film with higher (b) and lower magnification at two different positions on the sample (c and d). SEM images were acquired with an acceleration voltage of 4 kV.*

Figure 49b provides a high resolution SEM image of the $Au@SiO_x$ NPs on top of the RuO_2 catalyst film. Here, the NPs appear as bright objects positioned directly on top of the nano-crystalline RuO_2 film. The distribution of $Au@SiO_x$ NPs on the RuO_2 film at two different positions is shown in Figure 49c and d. The NPs cover a significant fraction of the RuO_2 film. Apparently, most of the NPs do not appear separately but arrange in the vicinity of other NPs leading to small two-dimensional aggregates with different average NP coverage (Figure 49c and d). The described state appears optimal for in-situ SHINERS, since particle aggregates cause a boosted electromagnetic field enhancement⁶⁵ and the catalyst surface still remains accessible for sufficient transport of educts and products.

Whether or not the Au@SiO_x particles interfere with the RuO₂ catalyst film altering its electrocatalytic properties was investigated by CV (Figure 50). It is clearly apparent that the OER commences just below 1.4 V_{RHE} independent if Au@SiO_x NPs were deposited or not. The electrocatalytic OER activity (current density at a certain overpotential) and the electrochemical redox behavior of RuO₂ prior to the OER onset (E<1.4) are almost identical in both cases. Thus, the Au@SiO_x NPs do not electrochemically interfere with the RuO₂ film. The small differences observed are most likely related to the partial blocking of the RuO₂ surface area by Au@SiO_x particles and, hence, not by any chemical interaction. Therefore, Au@SiO_x NPs are not expected to alter the surface species present on RuO₂ during the OER.

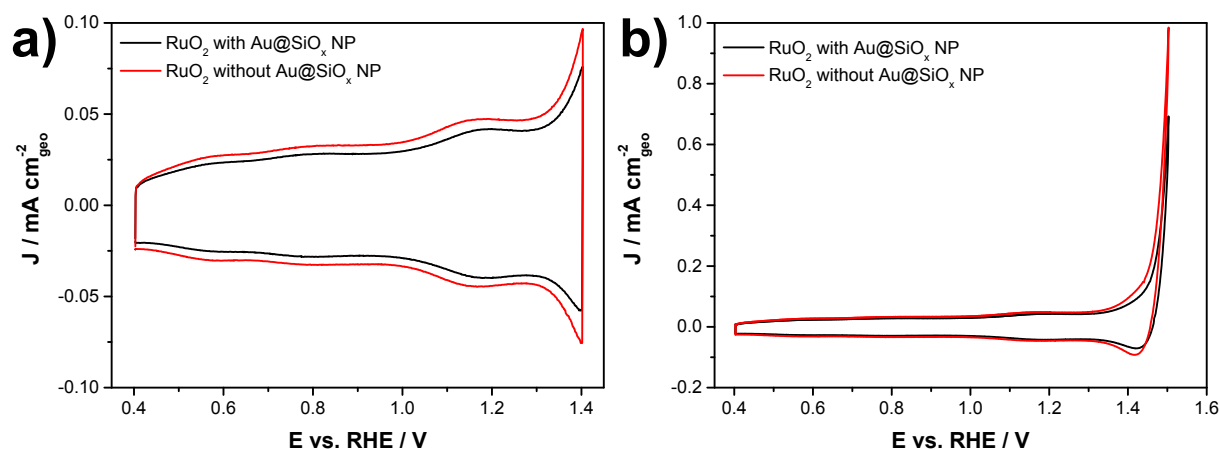


Figure 50: *Cyclic voltammetry of the RuO₂ catalyst film measured with and without Au@SiO_x NP coating between 0.4 V and 1.4 V (a) or 1.5 V (b), respectively. The measurements were performed in 0.1 M HClO₄ with 50 mV s⁻¹.*

7.4 Design of electrochemical in-situ SHINERS cell

The spectro-electrochemical cell developed for in-situ SHINERS measurements is depicted in Figure 51. Therein, a leak-free micro Ag/AgCl reference electrode - avoiding chloride contamination of the electrolyte - was positioned close to the working electrode. A Pt mesh served as counter electrode. It was positioned in a glass tube connected to the cell body over a porous glass drip to separate products formed at the counter electrode from the working electrode compartment. A water immersion objective with high numerical aperture was applied for Raman measurements to minimize optical

losses. To avoid contaminations during the measurement the cell was covered with a transparent fluorinated ethylene propylene (FEP) copolymer foil exhibiting nearly the same refractive index as water. To exclude an influence of lateral inhomogeneities with respect to Au@SiO_x NP coverage, the Raman measurements were averaged over a large fraction of the electrode surface area by moving the electrochemical in-situ cell repeatedly 1 mm back and forth in the focal plane.

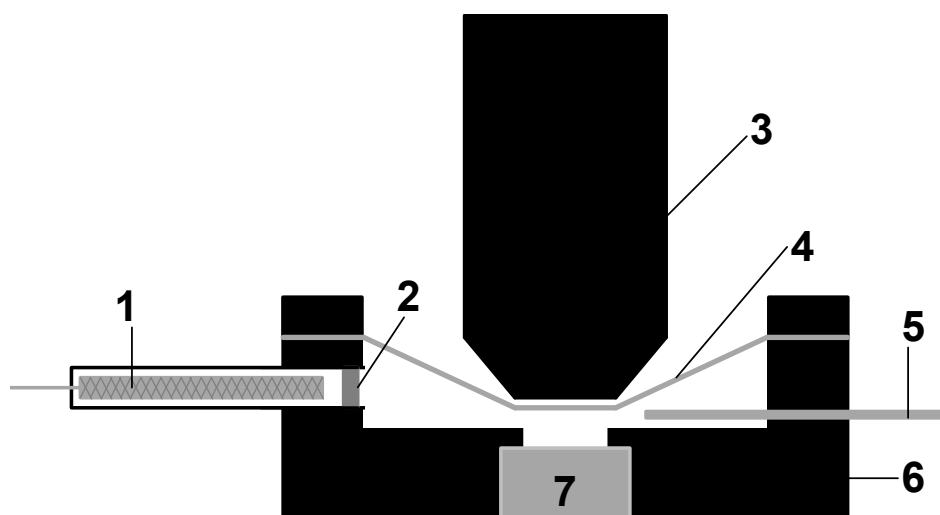


Figure 51: *Schematic representation of the spectro-electrochemical cell. 1: Pt mesh counter electrode, 2: porous glass drip, 3: immersion objective, 4: transparent polymer foil, 5: Ag/AgCl reference electrode, 6: cell body, 7: sample*

7.5 In-situ SHINERS measurements

With the setup described above, in-situ SHINERS spectra depicted in Figure 52 were obtained at potentials below (0.4 and 1.2 V_{RHE}) and within the OER (1.4 and 1.5 V_{RHE}).

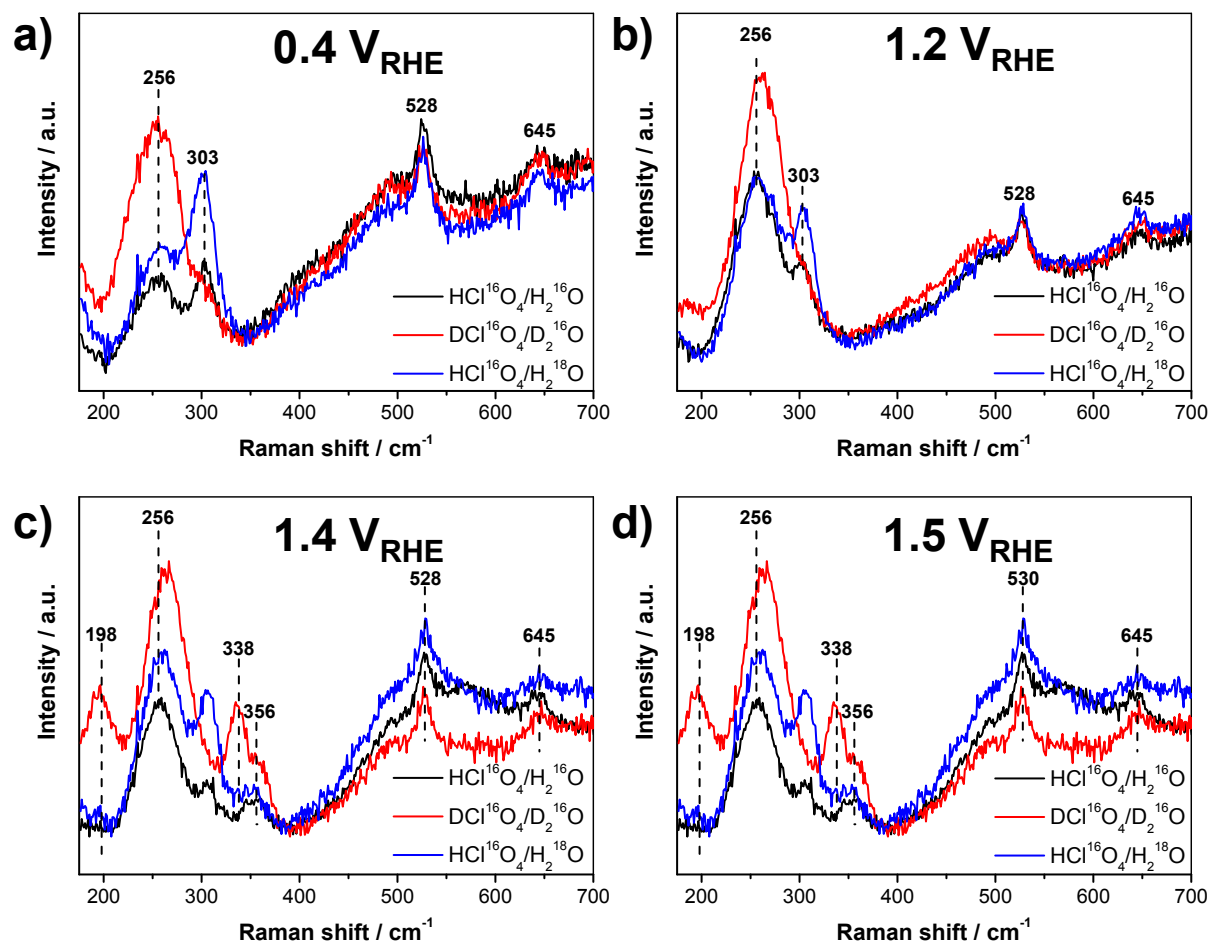


Figure 52: SHINER spectra acquired at electrode potentials of (a) 0.4, (b) 1.2, (c) 1.4, and (d) 1.5 V_{RHE} . The SHINER measurements were performed in 0.1 M $HCl^{16}O_4/H_2^{16}O$ (black), $DCI^{16}O_4/D_2^{16}O$ (red) and $HCl^{16}O_4/H_2^{18}O$ (blue) electrolyte of 0.1 M concentration, respectively.

To identify Raman bands corresponding to OER intermediates, all measurements were performed with 0.1 M $HCl^{16}O_4/H_2^{16}O$, $DCI^{16}O_4/D_2^{16}O$ and $HCl^{16}O_4/H_2^{18}O$ as electrolyte. In the latter case the presence of $HCl^{16}O_4$ in $H_2^{18}O$ is not expected to alter the isotopic purity of water since oxygen atoms of water and perchloric acid are not expected to exchange. At 0.4 V basically four signals were present in the spectrum located at ca. 256, 303, 528 and 645 cm^{-1} . In comparison with data obtained for RuO_2 films and single

crystals, the signals at ~ 528 and ~ 645 cm^{-1} can be identified as E_g and A_{1g} mode of bulk lattice RuO_2 .^{111,112} In accordance with these assignments, both bands did not display any H/D isotopic shifts, remained unchanged at all applied potentials (Figure 52), and were also found in measurements of RuO_2 without $\text{Au}@SiO_x$ particles (Figure 53). The slight differences observed with respect to the Raman shift of the RuO_2 E_g and A_{1g} mode can be rationalized by the different backgrounds and the experimental error and are thus not of significance here.

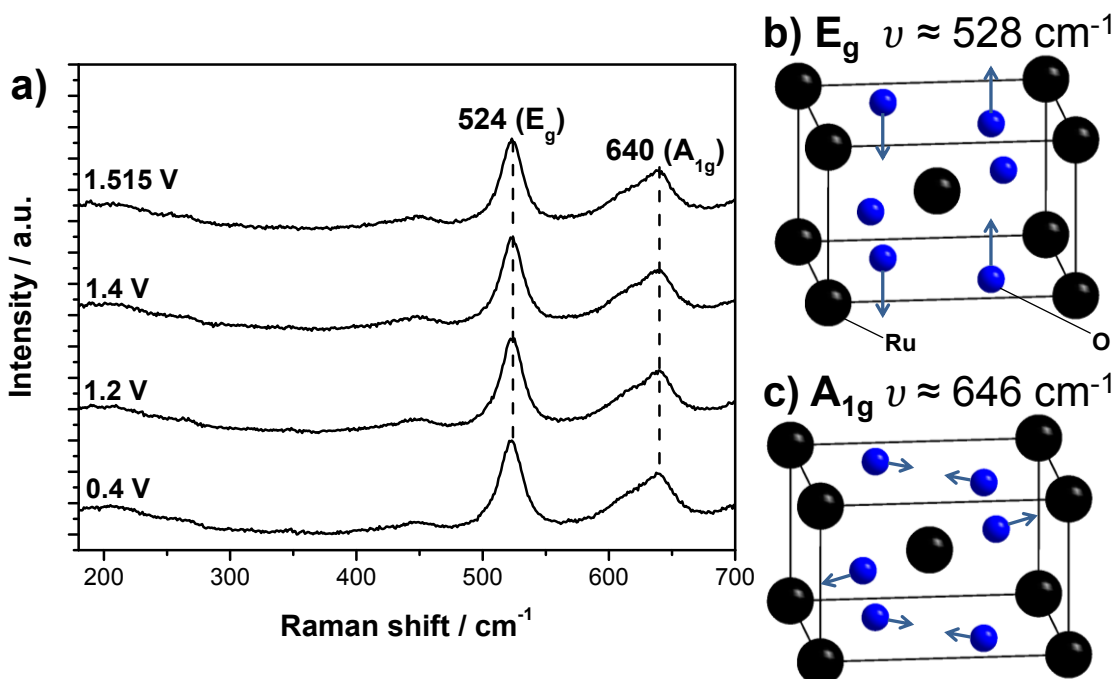


Figure 53: a) *in-situ* Raman spectra of a RuO_2 catalyst **without** $\text{Au}@SiO_x$ NP at different potentials measured in 0.1 M $\text{HCl}^{16}\text{O}_4/\text{H}_2^{16}\text{O}$. b) and c) Illustration of the E_g and A_{1g} lattice vibration of RuO_2 according to reference⁸² together with vibration frequencies measured for a RuO_2 single crystal¹¹¹.

Control measurements in which the $\text{Au}@SiO_x$ NPs were directly applied onto the Ti substrate in form of polished Ti and TiO_x (thermally oxidized equivalent to RuO_2 catalysts) - without any RuO_2 film - were carried out to identify signals which do not originate from the RuO_2 catalyst or its surface species (Figure 54a and b). In these experiments only two potential-independent signals were found at ~ 250 and ~ 300 cm^{-1} , which were also observed for the $\text{Au}@SiO_x$ NP coated RuO_2 film. Hence, these bands were attributed exclusively to the $\text{Au}@SiO_x$ NPs. Again, the slight differences with

respect to the Raman shifts are assigned to the different backgrounds and the experimental error and thus are not of significance here. Interestingly, the intensity of the signal $\sim 300\text{ cm}^{-1}$ decreased during the measurements. Thus, this band may result from impurities adsorbed on the particles which were slowly dissolved or decomposed by the acidic solution. Furthermore, the signal at $\sim 250\text{ cm}^{-1}$ shows a slightly potential-dependent intensity variation in both the control experiments (see Figure 54) and the measurements of the RuO_2 surface (Figure 52).

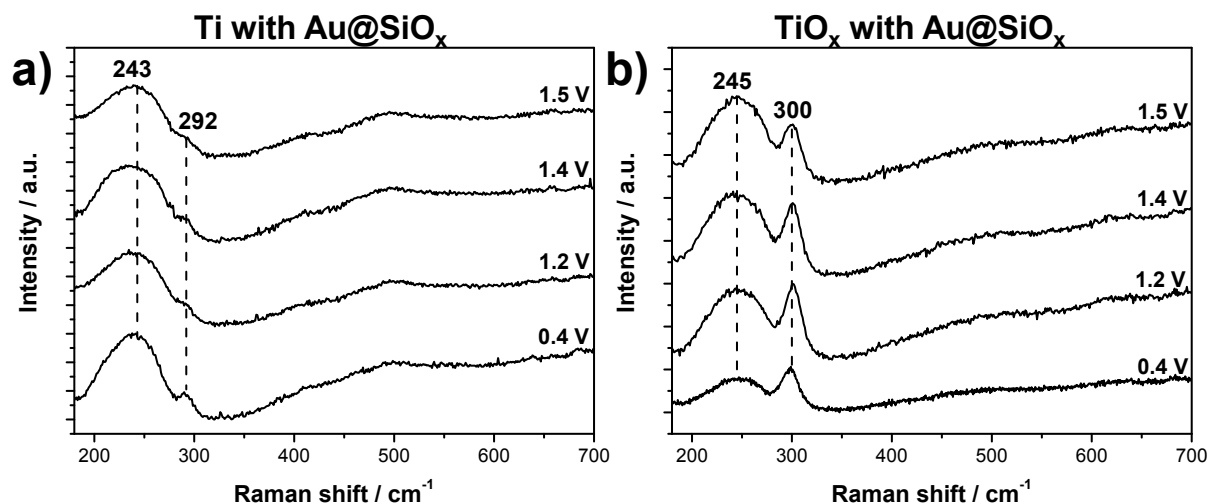


Figure 54: in-situ SHINER spectra of a) polished Ti and b) TiO_x (polished and thermally treated equivalent to RuO_2 catalyst) reference samples covered with Au@SiO_x NPs at different potentials measured in $0.1\text{ M HCl}^{16}\text{O}_4/\text{H}_2^{16}\text{O}$.

In the potential range of the OER, new bands appeared which, therefore, undoubtedly are related to the catalytic process. At 1.4 V a band at 356 cm^{-1} emerged and became more pronounced when the OER rate was increased at 1.5 V . In a previous resonance Raman spectroscopic study of μ -oxo bridged $\text{cis,cis-}[(\text{bpy})_2\text{Ru}(\text{OH}_2)]_2\text{O}^{4+}$ in aqueous solution, a band at 358 cm^{-1} was assigned to the H/D insensitive symmetric stretching mode of the Ru-O-Ru entity.¹¹³ For the present 356 cm^{-1} band, this assignment can be discarded since this band red-shifted to 338 cm^{-1} in $\text{DCl}^{16}\text{O}_4/\text{D}_2^{16}\text{O}$ solution, which demonstrates that H is involved in this species. Moreover, the assignment to a rocking vibration of a peroxy species, predicted as OER intermediate by DFT (see section 1.4), is unlikely, because no corresponding $\nu(\text{O-O})$ stretching vibration, expected around 800 cm^{-1} ,⁶⁶ was seen in the high wavenumber portion of the SER spectra (Figure 55).

The peak at 934 cm^{-1} in Figure 55 is most likely related to the Cl-O stretching mode of perchlorate ions from the electrolyte.⁵⁴ The signal visible at $\sim 1000\text{ cm}^{-1}$ remains unassigned but its intensity decreases with increasing potential making a correlation to the OER unlikely. It should be pointed out that only those reaction intermediates are commonly observable, which show a sufficiently high surface coverage, hence, constitute a reactant of the rate limiting step of the reaction. Thus, the lack of peroxide related signals does not rule out the involvement of such species at low steady state concentrations in the OER mechanism.

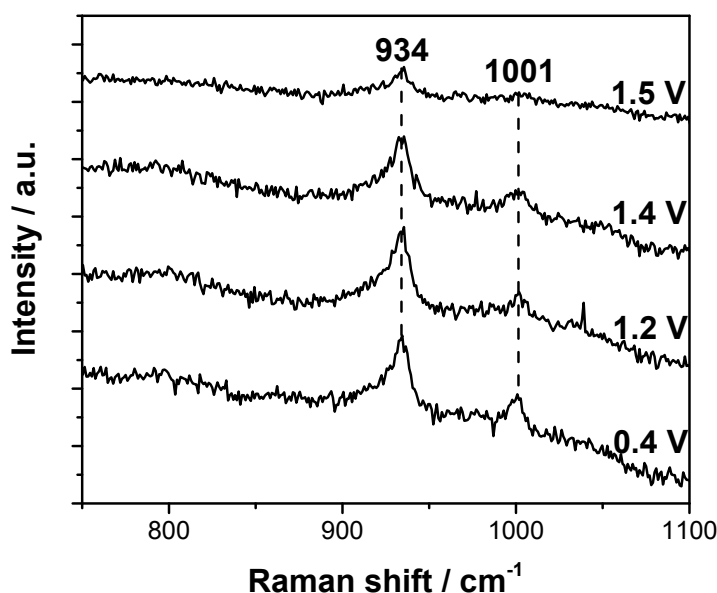


Figure 55: in-situ SHINER spectra of the RuO_2 catalyst covered with Au@SiO_x NPs at higher Raman shifts measured in $0.1\text{ M HCl}^{16}\text{O}_4/\text{H}_2^{16}\text{O}$ at different potential (vs. RHE).

We therefore conclude that the band at 356 cm^{-1} (H/D shift: 18 cm^{-1}) originates from either an OH or OH_2 surface species. Assignment to the symmetric stretching of the $\text{Ru}-\mu(\text{OH})-\text{Ru}$ group is favored in view of a very similar H/D isotopic shift of 16 cm^{-1} that has been observed for a $\text{Cu}-\mu(\text{OH})-\text{Cu}$ complex.¹¹⁴ Moreover, this assignment is in line with the absence of any $^{18}\text{O}/^{16}\text{O}$ shift, which implies that the oxygen atom involved in this mode is strongly bonded to the catalyst so that it cannot exchange with the electrolyte as expected for a $\text{Ru}-\mu(\text{OH})-\text{Ru}$ group. However, the band position argues against this assignment. Interestingly, a $\nu(\text{Ru}-\text{OH}_2)$ asymmetric stretching vibration was detected at

357 cm^{-1} in $\text{Ru}_2\text{OCl}_{10}^{4-}$ complexes.¹¹⁵ For such a mode an H/D shift by a factor of 0.95 is expected, which perfectly fits to the shift observed here but cannot explain the observed absence of any $^{18}\text{O}/^{16}\text{O}$ shift. A Ru- ν (OH_2)-Ru species has been observed in HREELS experiments on a $\text{RuO}_2(110)$ surface in presence of H_2 .¹¹⁶ However, the applied reductive conditions in this single crystal study make the appearance of a similar species under the oxidative OER conditions present in this work less likely.

Alternatively, a rocking vibration of an OH group connected to one Ru center in a $[\text{Ru}(\text{NH}_3)_4(\text{OH})(\text{NO})]^{2+}$ complex has been detected at 283 cm^{-1} by Raman spectroscopy.¹¹⁷ This mode, however, should be accompanied by a stretching vibration between 500 and 700 cm^{-1} . Unfortunately the presence of RuO_2 bulk modes at ~ 530 and $\sim 645\text{ cm}^{-1}$ hampers the accurate identification of other signals in this range such that assignment of the 356 cm^{-1} band to a rocking vibration cannot be verified or excluded. Therefore, to this end, it cannot be unambiguously determined whether an OH or OH_2 species is present at the RuO_2 surface under reactive OER conditions, although the presence of a Ru- μ (OH)-Ru group appears more probable.

The band at 190 cm^{-1} , which emerges in $\text{DCl}^{16}\text{O}_4/\text{D}_2^{16}\text{O}$ at OER potentials, is not yet identified. A shift of the potential-independent band at $\sim 250\text{ cm}^{-1}$, which is due to the NPs, appears unlikely, since the band at $\sim 190\text{ cm}^{-1}$ increases with potential. The most probable explanation here is an overlap of two different bands at $\sim 250\text{ cm}^{-1}$, with one of them shifting upon H/D exchange. This will be part of a future investigation.

7.6 Conclusion

The SHINERS approach was extended to the in-situ investigation of thermally prepared RuO₂ catalysts during the OER. To achieve this, an additive-free nanoparticle deposition technology was developed following previous approaches, adopted to the current catalytic system and successfully utilized to obtain a quite homogenous particle distribution on the RuO₂ film. Furthermore, an in-situ cell was designed specifically for the OER in which optical losses were minimized. The continuous change of the measuring position based on a motorized x-y-table avoided beam damage and achieved an averaging over a large portion of the surface. Thus imperfections in the sample, problematic for spatially resolved techniques, were unable to disturb the measurements, given their fraction remained small.

Based on the SHINERS approach a surface modification in the catalytically active state of RuO₂ could be monitored. An OH, or perhaps an OH₂, surface species was identified in-situ under OER conditions based on H/D exchange measurements. This OH_x species is thought to be involved in the rate determining step, since it was spectroscopically observable and thus had a rather high surface coverage. However, this OH_x species itself seems not to be further oxidized to O₂, since it was insensitive to H₂¹⁸O/ H₂¹⁶O exchange. This does not mean that the OH_x species is not relevant for the OER process, since it appeared exclusively during the OER. Different possibilities appear conceivable how the OH_x species might be involved in the OER process. Speculatively, the OH_x species can be crucial to modify the binding properties of an OER reaction intermediate adsorbed on an adjacent active site or it might be involved in facilitating fast proton transfer away from the active site. However, the purpose of the OH_x species in the OER mechanism on RuO₂ needs to be clarified in a future study.

8 Conclusion and Perspective

Thin-film catalysts, based on Ir and Ru oxide, were developed and used as model systems to study structure-activity-stability relations for the OER as well as OER surface species under reaction conditions. For the examination of OER surface species, RuO₂ catalysts were investigated by in-situ shell isolated nanoparticle enhanced Raman spectroscopy. Considering the study of OER structure-activity-stability relations, initially the influence of calcination temperature on pure Ir oxides films and their interaction with the substrate were analyzed. To optimize and study Ir oxide in more detail, Ir-Ni mixed oxides were introduced and used to continuously vary the OER performance based on the Ni content. Monitoring the material properties during the continuous variation of the OER performance, the material properties relevant for the OER performance were identified. Although the OER performance was optimized substantially using Ir-Ni oxides, the identified material properties prefigure further optimization potential. Within this optimization process, catalyst substrate interactions and the catalyst substrate boundary are both of great importance and have to be included, as was shown for pure Ir oxide films. Furthermore, the obtained insights into OER surface species provide first insights into the OER mechanism and the actual rate determining step and, hence, provide a starting point for the OER performance optimization. Thus, the fundamental insights obtained here aid to achieve the most efficient utilization of scarce noble metals like Ir and Ru in PEM OER catalysts.

8.1 Pure Ir oxides and their interaction with the Ti substrate

The calcination temperature dependent study of pure Ir oxide films and their interaction with Ti substrates demonstrate the formation of two chemically distinct Ir oxides as function of the applied calcination temperature. Electrocatalytic OER measurements demonstrated that the low temperature Ir oxide provided a higher surface specific OER activity than the high temperature Ir oxide whereas the Ir stability showed an opposite behavior. The two Ir oxides were mainly characterized by differences in crystalline order, surface OH fraction, surface redox chemistry and stability against reduction. Thus, one or more of these properties is expected to be relevant for the OER performance.

Additionally, moderate calcination temperatures afforded maximum electrocatalytically active surface areas. Therefore, the best Ir utilization for pure Ir oxide films was achieved at calcination temperatures of 250 and 350°C, which showed almost identical OER activities. Although the OER activities were similar, the Ir dissolution rate differed by a factor of ~4. Unexpectedly, the IrOF calcined at 350°C provided a lower Ir stability, which was attributed to the presence of both Ir oxide phases in this film - the low and the high temperature phase. Hence, contrary to often claimed, there is not necessarily a tradeoff between OER activity and stability.

Evidence for Ti (substrate) oxidation was present for calcination temperatures $\geq 350^\circ\text{C}$. However, the formed Ti oxides did not affect the OER performance of Ir oxide at calcination temperatures $\leq 450^\circ\text{C}$. In contrast, at 550°C a Ti oxide interlayer was formed and Ti oxide migrated into the Ir oxide layer resulting in a chemically modified Ir oxide, which constituted a lower OER activity but an improved Ir dissolution stability. Ti dissolution increased with increasing calcination temperature and was not observed at a calcination temperature of 250°C. Thus, Ti dissolution is caused by Ti oxide species formed during calcination. However, Ti dissolution was most pronounced at the outset of the measurement and almost faded out during the course of the measurement for all samples. Hence, Ti is an excellent stable substrate material for OER catalysts.

8.2 Ir-Ni mixed metal oxides

Although there is an exceptional optimization potential for pure Ir oxides, this can still be extended by thermally prepared binary mixed oxides. Mixed oxides offer great opportunities for a systematic tuning of electrocatalytic activity and stability. This was exemplified here using well-defined thermally prepared Ir-Ni oxide thin-films. The Ir-Ni mixed oxides offer an unprecedented ~20 fold improvement in Ir mass-based OER activity over pure Ir oxide catalysts, calcined at the same temperature. Similarly, activity improvements were observed on a geometric as well as on an active surface area basis. Beyond the activity improvement, Ir-Ni mixed oxides were perfectly suited to analyze the material properties leading to a continuous variation of OER activity and stability. Therefore, the geometric, electronic, and morphological structures of the various Ir-Ni mixed oxide catalysts were examined. Based on these data, a number of novel

correlations between activity and stability and microscopic material descriptors were identified whereas others, such as Ni-related geometric strain effects, could be ruled out.

These data and analysis have resulted in a simple, yet intuitive model for the formation of the active state of the catalytic surface. The model suggested that the coverage of reactive surface hydroxyls serves as a useful descriptor for the OER activity. Formed by initial Ni dissolution and disruption of Ir-O-M motifs, the surface hydroxyls showed a reduced binding to the oxide lattice, which was conducive to catalytic activity. Though stability of Ir atoms was compromised in this process as well, surface normalized dissolution of Ir did not correlate with catalytic activity, suggesting – contrary to common beliefs - that a separate optimization of activity and stability may actually be possible. Thermally-prepared yet Ni-leached Ir-Ni oxide film catalysts exhibited compositional stability and surface electrochemical redox characteristics that closely resembled those of Ir oxides formed via electrochemical oxidation of metallic Ir surfaces. Hence, it was demonstrated how to balance catalytic activity advantages of oxidized metals with stability benefits of thermally prepared bulk oxides.

As a result to obtain the highest possible OER activity paired with the highest possible stability for an Ir oxide based catalyst, the number OH surface species and the number of Ir-O-M (M: other metal cation) motives in the sub-surface should both be maximized.

8.3 Comparison: IrNi mixed oxide vs. pure Ir oxides calcined at different temperatures

In the context of OER activity and Ir utilization Ir-Ni mixed oxides outperformed pure Ir oxides calcined at different temperatures resulting in a ~two fold higher Ir utilization (compared at $\eta=300$ mV). However, when it comes to Ir stability, the findings are reverse: pure Ir oxides provide lower dissolution rates than Ir-Ni mixed oxides (measured during 10 min OER with 1 mA cm^{-2} geometric current density). The best compromise of both OER activity and Ir stability is provided by the Ir oxide film catalyst calcined at 250°C , which shows a mass based Ir utilization half as high as the maximal MO and an exceptional stability.

8.4 In-situ Raman spectroscopic investigation of RuO₂

As the OER relevant material properties of IrO_x were identified, a further optimization requires mechanistic insights. Since Raman spectroscopy suffers from weak scattering cross-sections and, thus, weak intensities, the study of surface intermediates requires surface enhancement approaches applicable and inert under high potential acidic PEM OER conditions. All these requirements are fulfilled by shell isolated nanoparticle enhanced Raman spectroscopy, which was applied here to thermally prepared RuO₂ catalysts during the OER. Therefore, an electrochemical in-situ cell with minimized optical losses was designed specifically for the OER.

Based on the SHINERS approach a surface modification in the catalytically active state of RuO₂ could be monitored. An OH, or perhaps an OH₂, surface species was identified in-situ under OER conditions based on H/D exchange measurements. This OH_x species is thought to be involved in the rate determining step, since it was spectroscopically observable and thus had a rather high surface coverage. However, this OH_x species itself seems not to be further oxidized to O₂, since it was insensitive to H₂¹⁸O/ H₂¹⁶O exchange. This does not mean that the OH_x species is not relevant for the OER process, since it appeared exclusively during the OER. Different possibilities appear conceivable how the OH_x species might be involved in the OER process. Speculatively, the OH_x species can be crucial to modify the binding properties of an OER reaction intermediate adsorbed on an adjacent active site or it might be involved in facilitating fast proton transfer away from the active site. However, the purpose of the OH_x species in the OER mechanism on RuO₂ needs to be clarified in a future study.

8.5 Perspective

Based on the knowledge obtained about surface termination and bulk properties required for achieving a high OER activity and stability on Ir oxides, the Ir-Ni approach can be further optimized and, moreover, new synthesis strategies can be purposefully developed. Beside the optimization of the active component, OER activity restricting catalyst-substrate interactions can be avoided in these synthesis strategies by the knowledge obtained in this work. Thus, the development of synthesis strategies is expected to yield in catalysts with optimized OER activity and stability.

The identification of an OH_x surface group during the OER by shell isolated nanoparticle enhanced Raman spectroscopy (SHINERS) is an important new insight into the OER mechanism. Although the OH_x is not a direct intermediate in the OER pathway - which means that it is not undergoing a reaction cascade to O_2 - the OH_x might be important to facilitate the OER pathway. This aspect has so far been mostly overlooked in the context of PEM-OER catalysts and needs closer investigations. Therefore, the exact nature of the observed OH_x species and its purpose in the OER mechanism have to be studied for instance by SHINER spectroscopy at different pH values for different catalyst materials in close relation with additional surface sensitive analytical techniques and theoretical DFT based calculations.

9 Appendix

Table 2: Rietveld refinement results for IrOF(550°C)/Ti cylinder (GOF: 2.81)

phase	space group	crystallite size / nm	lattice parameters			preferred orientation	
			a/ Å	b/ Å	c/ Å		
IrO ₂	P42/mnm	7.4	4.5051	-	3.1586	0.727 (1 1 0)	-
TiO ₂	P42/mnm	12.2	4.5922	-	2.9574	1.104 (1 1 0)	-
TiO _x	P63/mmc	24.8	2.9607	-	4.7347	-	-
Ti	P63/mmc	67.8	2.9500	-	4.6860	0.140 (0 0 1)	0.935 (0 1 0)

Table 3 : Rietveld refinement results for IrOF(450°C)/Ti cylinder (GOF: 2.15)

phase	space group	crystallite size / nm	lattice parameters			preferred orientation	
			a/ Å	b/ Å	c/ Å		
IrO ₂	P42/mnm	4.5	4.5051	-	3.1586	0.805 (1 1 0)	1.880 (0 1 1)
Ti	P63/mmc	61.2	2.9500	-	4.6860	0.586 (0 1 0)	0.866 (0 1 1)

Table 4: Rietveld refinement results for the RuO₂ thin-film on a Ti cylinder (GOF: 2.67)

phase	space group	crystallite size / nm	lattice parameters			preferred orientation	
			a/ Å	b/ Å	c/ Å		
RuO ₂	P42/mnm	19.2	4.4968	-	3.1049	0.844 (1 1 0)	
TiO ₂	P42/mnm	13.0	4.5922	-	2.9574	0.981 (1 1 0)	0.433 (0 1 1)
Ti	P63/mmc	70.5	2.9500	-	4.6860	0.317 (0 1 0)	0.618 (1 1 0)

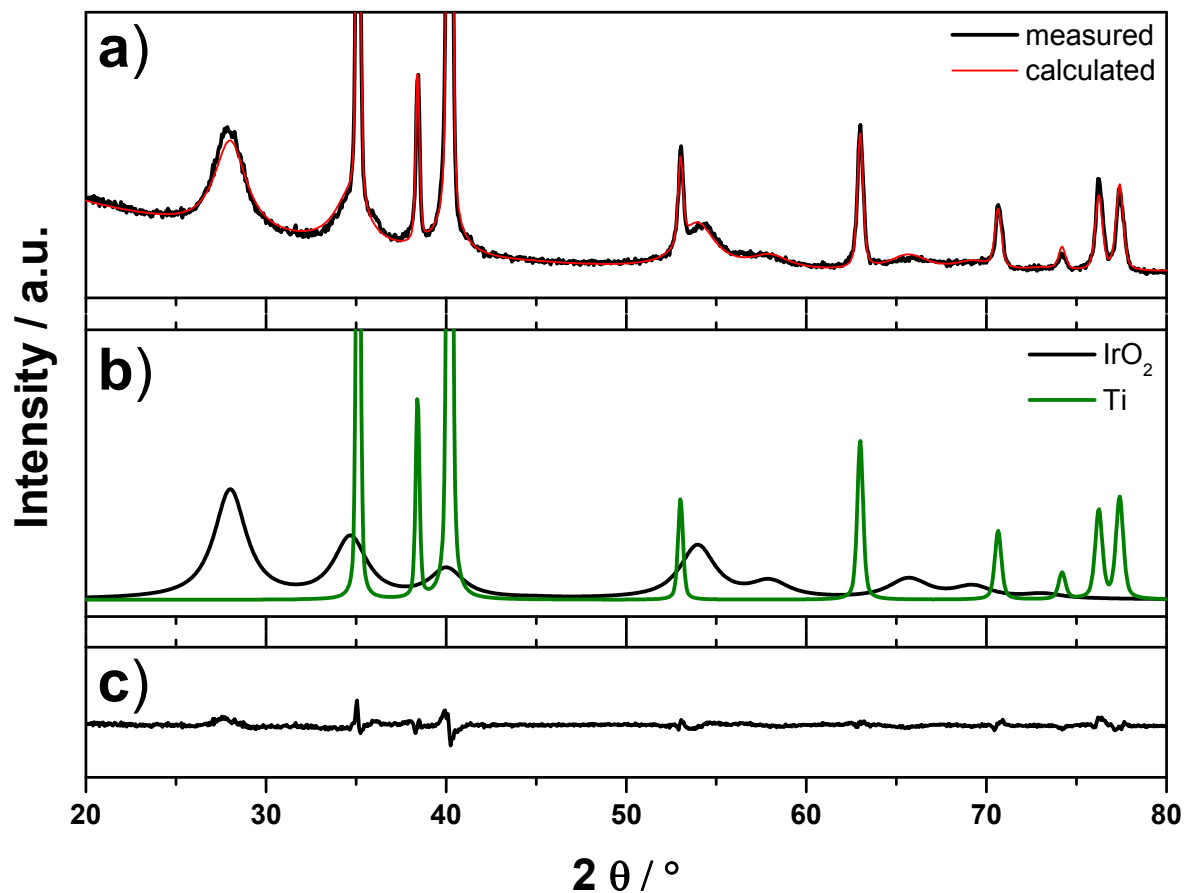


Figure 56: *Grazing incidence X-ray diffraction measurement of IrOF(450°C) on a Ti cylinder together with results from Rietveld refinement. a) Measured and calculated diffraction pattern, b) contribution of the individual phases used within the refinement and c) difference between measured and calculated diffraction pattern.*

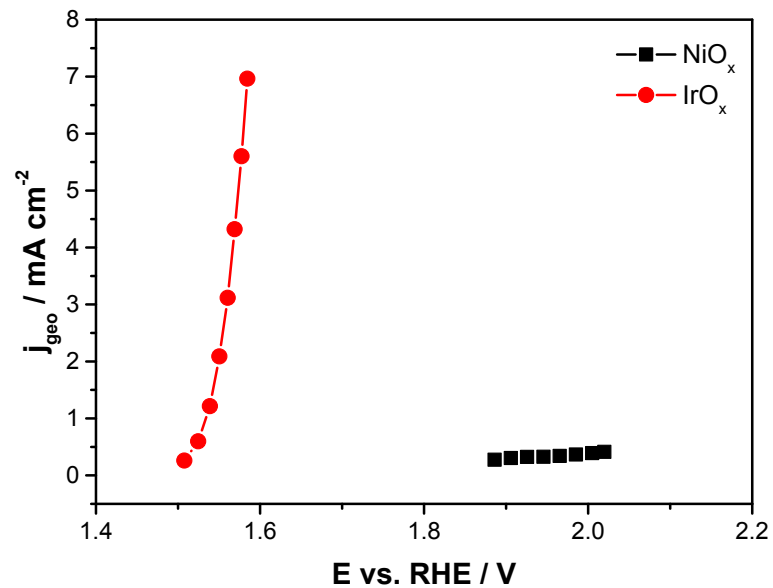


Figure 57: Quasi stationary polarization curves for pure Ir and pure Ni oxide films (iR corrected).

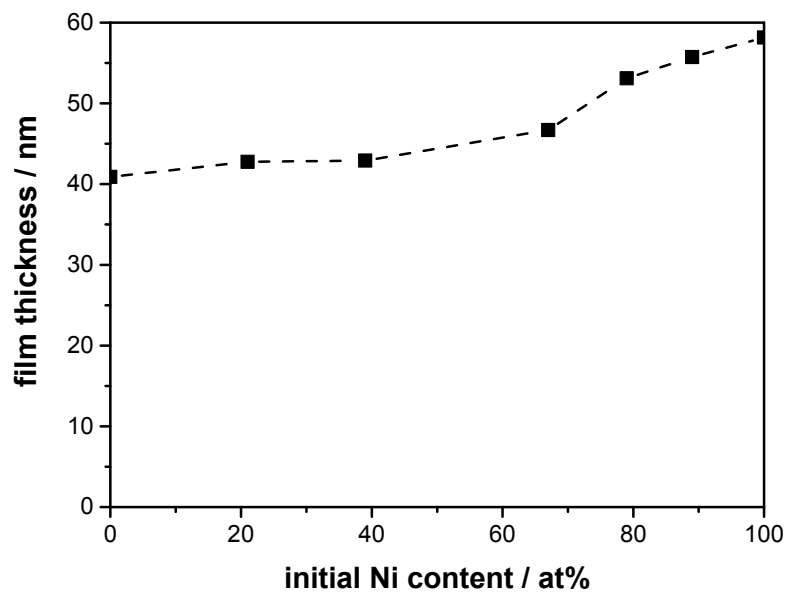


Figure 58: Film thickness of MO-ap as function of the initial Ni content measured by cross section SEM. Silicon wafers were applied as substrates.

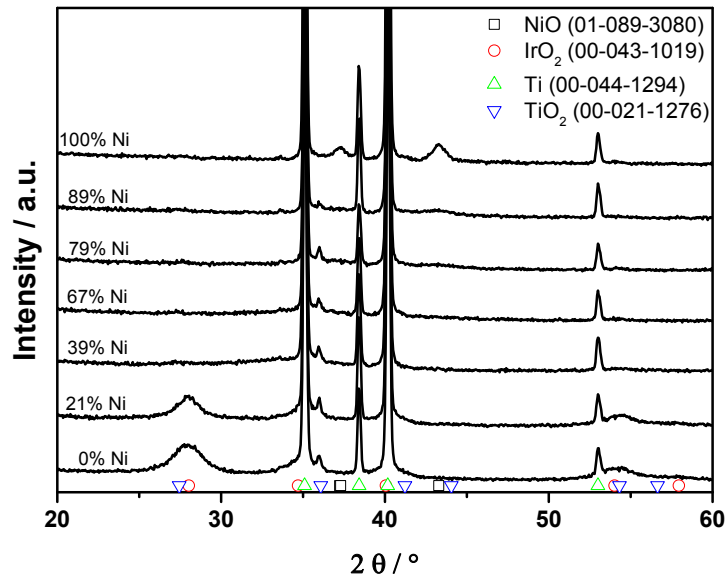


Figure 59: Grazing incidence X-ray diffraction measurements of MO-ap. Reference patterns from the powder diffraction file are provided for comparison.

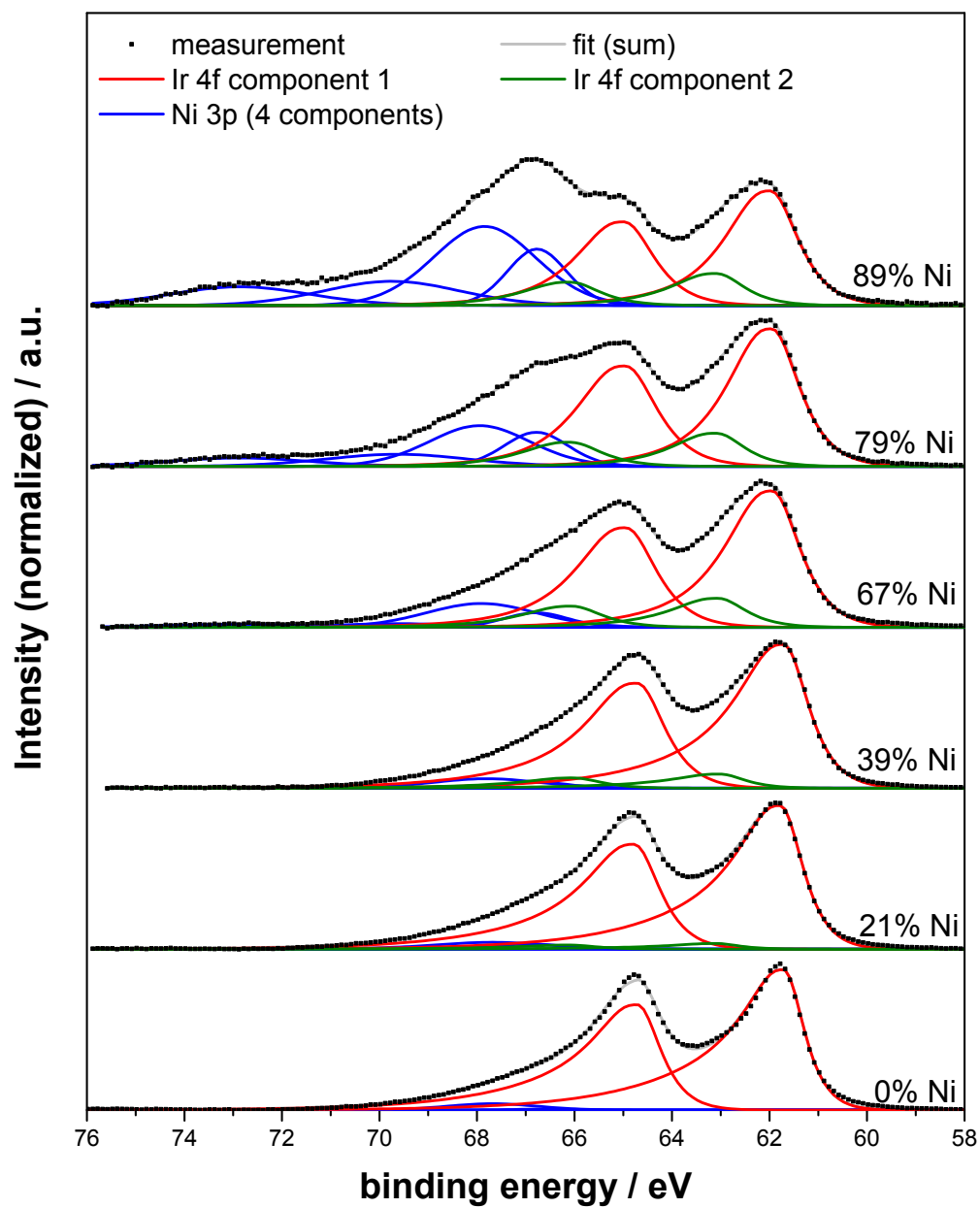


Figure 60: Fitted X-ray photoelectron spectra of the Ir 4f and Ni 3p region of MO-ap.

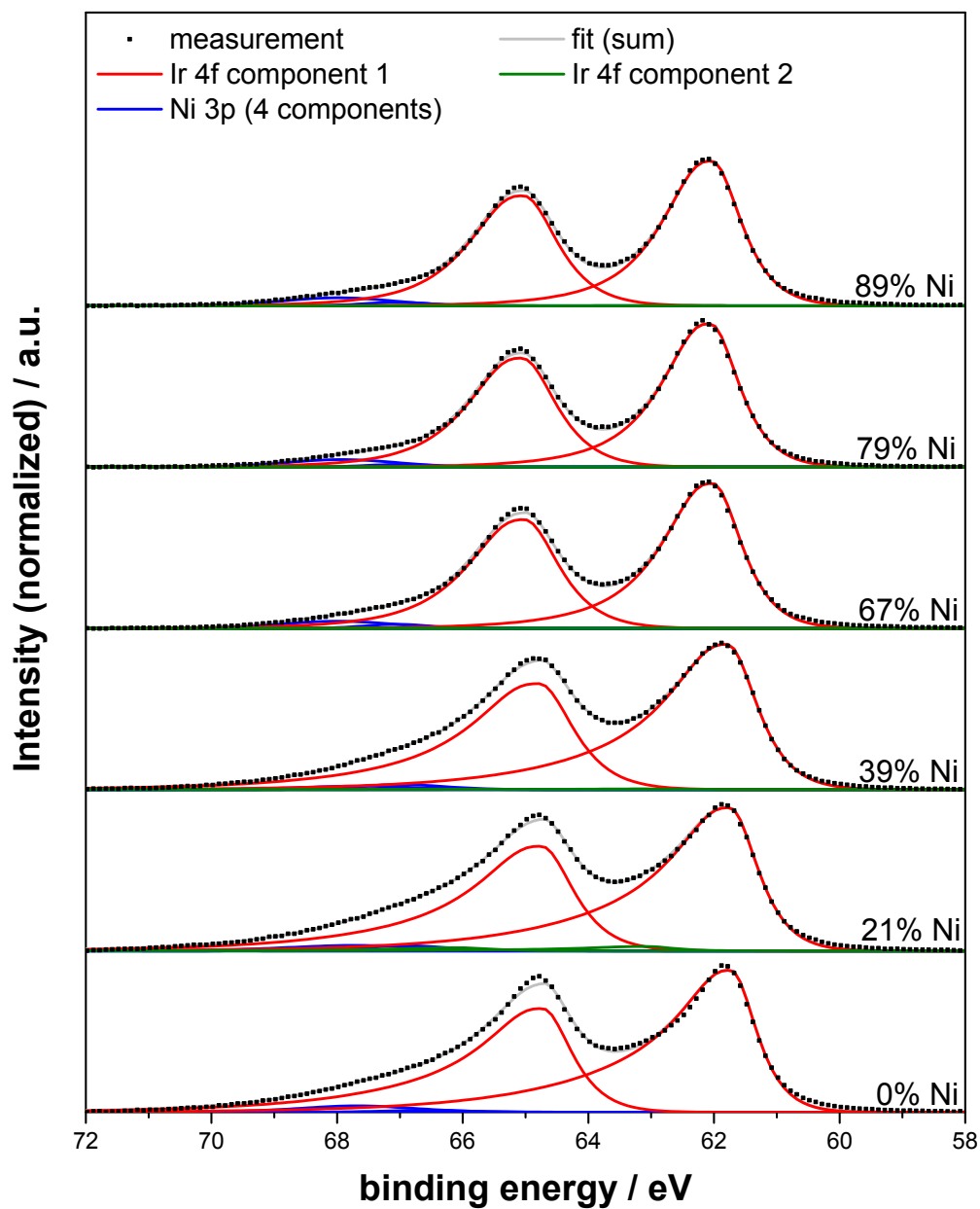


Figure 61: Fitted X-ray photoelectron (XP) spectra of the Ir 4f and Ni 3p region of MO-OER.

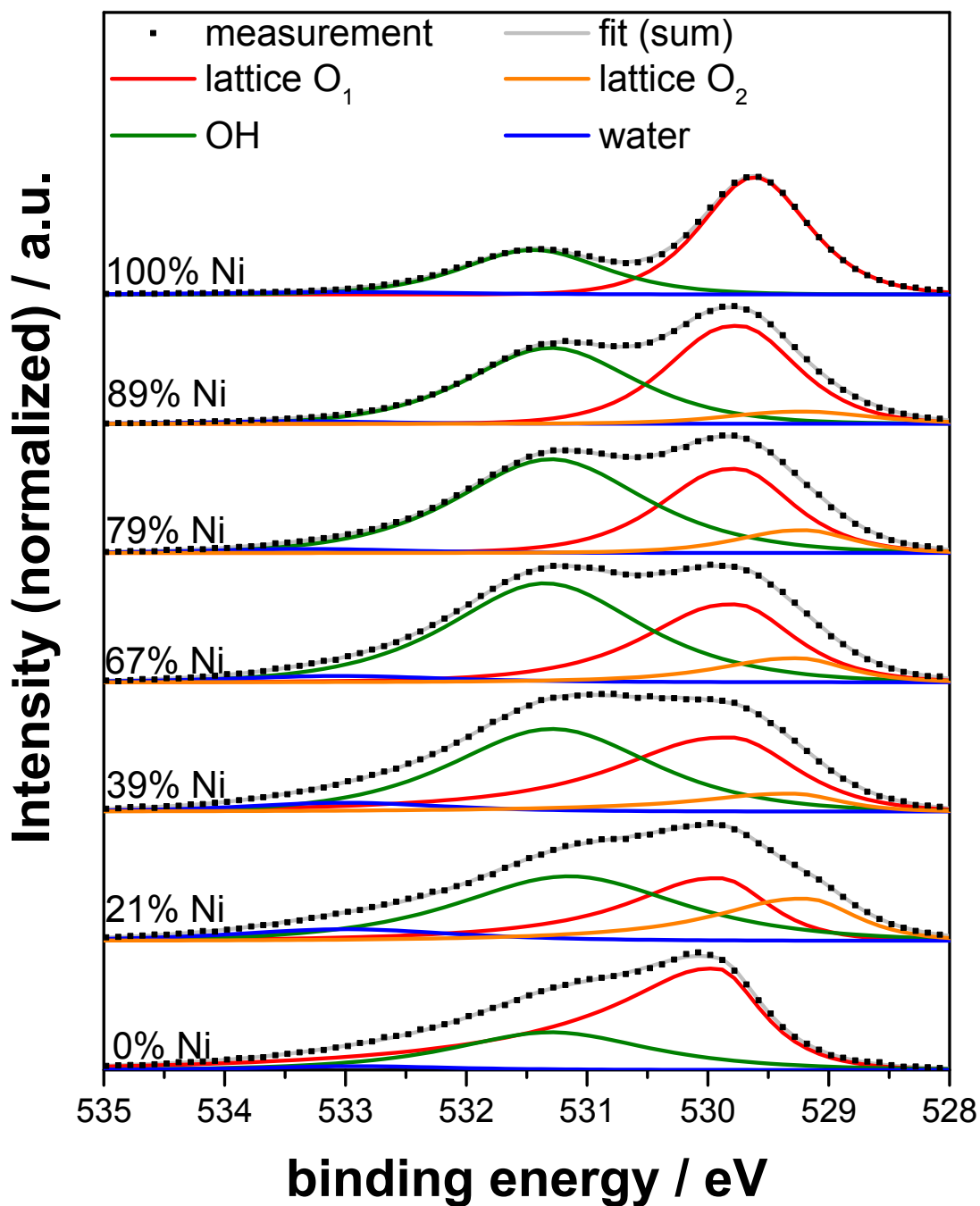


Figure 62: Fitted X-ray photoelectron spectra of the O 1s region of MO-ap.

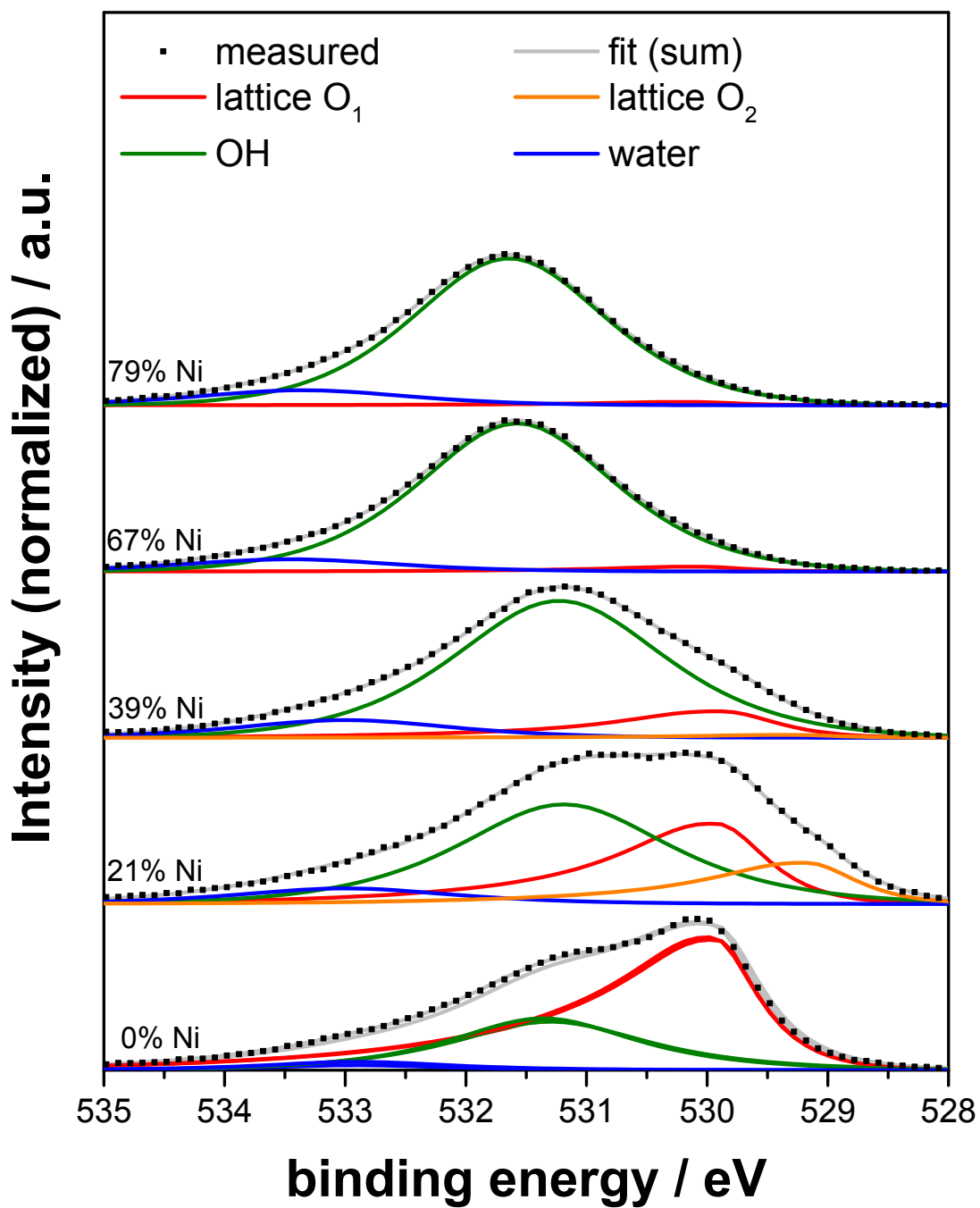


Figure 63: Fitted X-ray photoelectron spectra of the O 1s region of MO-OER.

10 References

- (1) https://www.energy-charts.de/power_de.htm, Fraunhofer ISE, access date: 09.01.2015
- (2) Beck, H.-P.; Engel, B.; Hofmann, L.; Menges, R.; Turek, T.; Weyer, H.; Benger, R.; Beyer, K.; Brenner, S.; Funck, F.; Güttel, R.; Hingst, J.; Franziska, L.; Mbuy, A.; Minke, C.; Neumann, C.; Runge, S. A.; Schöß, M. A.; Springmann, J.-P.; Unger, D.; Lipinski, L. W. *Studie zum Erhalt der Systemsicherheit*, Energie-Forschungszentrum Niedersachsen, 2013.
- (3) Sherif, S. A.; Barbir, F.; Veziroglu, T. N. *Sol. Energy* **2005**, *78*, 647.
- (4) Bockris, J. O. M. *Science* **1972**, *176*, 1323.
- (5) Crabtree, G. W.; Dresselhaus, M. S.; Buchanan, M. V. *Phys. Today* **2004**, *57*, 39.
- (6) Carmo, M.; Fritz, D. L.; Merge, J.; Stolten, D. *Int. J. Hydrogen Energy* **2013**, *38*, 4901.
- (7) Laguna-Bercero, M. A. *J. Power Sources* **2012**, *203*, 4.
- (8) Dau, H.; Limberg, C.; Reier, T.; Risch, M.; Roggan, S.; Strasser, P. *ChemCatChem* **2010**, *2*, 724.
- (9) Beer, H. B. *J. Electrochem. Soc.* **1980**, *127*, C303.
- (10) Nora, V. D.; Burgsdorff, J. W. K. V. *Chem. Ing. Tech.* **1975**, *47*, 125.
- (11) Hollemann, A. F.; Wiberg, E.; Wiberg, N. *Lehrbuch der Anorganischen Chemie*; Walter de Gruyter: Berlin, 2007; Vol. 102.
- (12) Matsumoto, Y.; Sato, E. *Mater. Chem. and Phys.* **1986**, *14*, 397.
- (13) Danilovic, N.; Subbaraman, R.; Chang, K. C.; Chang, S. H.; Kang, Y. J. J.; Snyder, J.; Paulikas, A. P.; Strmcnik, D.; Kim, Y. T.; Myers, D.; Stamenkovic, V. R.; Markovic, N. M. *J. Phys. Chem. Lett.* **2014**, *5*, 2474.
- (14) Cherevko, S.; Zeradjanin, A. R.; Topalov, A. A.; Kulyk, N.; Katsounaros, I.; Mayrhofer, K. J. J. *ChemCatChem* **2014**, *6*, 2219.
- (15) Reier, T.; Oezaslan, M.; Strasser, P. *ACS Catal.* **2012**, *2*, 1765.
- (16) Conway, B. E.; Mozota, J. *Electrochim. Acta* **1983**, *28*, 9.
- (17) Mozota, J.; Conway, B. E. *Electrochim. Acta* **1983**, *28*, 1.
- (18) Gottesfeld, S.; Srinivasan, S. *J. Electroanal. Chem.* **1978**, *86*, 89.
- (19) Beni, G.; Schiavone, L. M.; Shay, J. L.; Dautremontsmith, W. C.; Schneider, B. S. *Nature* **1979**, *282*, 281.
- (20) Miles, M. H.; Huang, Y. H.; Srinivasan, S. *J. Electrochem. Soc.* **1978**, *125*, 1931.
- (21) Matsumoto, Y.; Tazawa, T.; Muroi, N.; Sato, E. *J. Electrochem. Soc.* **1986**, *133*, 2257.
- (22) Trasatti, S. In *Electrochemistry of Novel Materials*; Lipkowski, J., Ross, P. N., Eds.; Wiley-Interscience: 1994; Vol. 3.
- (23) Trasatti, S. *Electrochim. Acta* **1984**, *29*, 1503.
- (24) Fabbri, E.; Haberer, A.; Waltar, K.; Kotz, R.; Schmidt, T. J. *Catal. Sci. Technol.* **2014**, *4*, 3800.
- (25) Cherevko, S.; Reier, T.; Zeradjanin, A. R.; Pawolek, Z.; Strasser, P.; Mayrhofer, K. J. J. *Electrochem. Commun.* **2014**, *48*, 81.
- (26) de Oliveira-sousa, A.; da Silva, M. A. S.; Machado, S. A. S.; Avaca, L. A.; de Lima-Neto, P. *Electrochim. Acta* **2000**, *45*, 4467.
- (27) Kulandaisamy, S.; Rethinaraj, J. P.; Chockalingam, S. C.; Visvanathan, S.; Venkateswaran, K. V.; Ramachandran, P.; Nandakumar, V. *J. Appl. Electrochem.* **1997**, *27*, 579.
- (28) Ouattara, L.; Fierro, S.; Frey, O.; Koudelka, M.; Comninellis, C. *J. Appl. Electrochem.* **2009**, *39*, 1361.
- (29) Vukovic, M. *J. Appl. Electrochem.* **1990**, *20*, 969.
- (30) Fierro, S.; Kapałka, A.; Comninellis, C. *Electrochem. Commun.* **2010**, *12*, 172.
- (31) Kötz, R.; Stucki, S. *J. Electrochem. Soc.* **1985**, *132*, 103.
- (32) Kotz, R.; Stucki, S. *Electrochim. Acta* **1986**, *31*, 1311.
- (33) Yeo, R. S.; Orehotsky, J.; Visscher, W.; Srinivasan, S. *J. Electrochem. Soc.* **1981**, *128*, 1900.

- (34) Danilovic, N.; Subbaraman, R.; Chang, K. C.; Chang, S. H.; Kang, Y. J.; Snyder, J.; Paulikas, A. P.; Strmcnik, D.; Kim, Y. T.; Myers, D.; Stamenkovic, V. R.; Markovic, N. M. *Angew. Chem. Int. Ed.* **2014**, *53*, 14016.
- (35) Comninellis, C.; Vercesi, G. P. *J. Appl. Electrochem.* **1991**, *21*, 335.
- (36) Ye, Z.-G.; Meng, H.-M.; Chen, D.; Yu, H.-Y.; Huan, Z.-S.; Wang, X.-D.; Sun, D.-B. *Solid State Sci.* **2008**, *10*, 346.
- (37) Terezo, A. J.; Bisquert, J.; Pereira, E. C.; Garcia-Belmonte, G. *J. Electroanal. Chem.* **2001**, *508*, 59.
- (38) Chen, G.; Chen, X.; Yue, P. L. *J. Phys. Chem. B* **2002**, *106*, 4364.
- (39) De Pauli, C. P.; Trasatti, S. *J. Electroanal. Chem.* **2002**, *538-539*, 145.
- (40) Ardizzone, S.; Bianchi, C. L.; Borgese, L.; Cappelletti, G.; Locatelli, C.; Minguzzi, A.; Rondinini, S.; Vertova, A.; Ricci, P. C.; Cannas, C.; Musinu, A. *J. Appl. Electrochem.* **2009**, *39*, 2093.
- (41) Wang, X.-M.; Hu, J.-M.; Zhang, J.-Q. *Electrochim. Acta* **2010**, *55*, 4587.
- (42) Zhang, J.-J.; Hu, J.-M.; Zhang, J.-Q.; Cao, C.-N. *Int. J. Hydrogen Energy* **2011**, *36*, 5218.
- (43) Oh, H. S.; Nong, H. N.; Strasser, P. *Adv. Funct. Mater.* **2015**, *25*, 1074.
- (44) Macounová, K.; Jirkovský, J.; Makarova, M. V.; Franc, J.; Krtíl, P. *J. Solid State Electrochem.* **2009**, *13*, 959.
- (45) Petrykin, V.; Bastl, Z.; Franc, J.; Macounova, K.; Makarova, M.; Mukerjee, S.; Ramaswamy, N.; Spirovova, I.; Krtíl, P. *J. Phys. Chem. C* **2009**, *113*, 21657.
- (46) Kötz, R.; Stucki, S.; Scherson, D.; Kolb, D. M. *J. Electroanal. Chem. Interfacial Electrochem.* **1984**, *172*, 211.
- (47) Wohlfahrt-Mehrens, M.; Heitbaum, J. *J. Electroanal. Chem. Interfacial Electrochem.* **1987**, *237*, 251.
- (48) Frydendal, R.; Paoli, E. A.; Knudsen, B. P.; Wickman, B.; Malacrida, P.; Stephens, I. E. L.; Chorkendorff, I. *Chemelectrochem* **2014**, *1*, 2075.
- (49) Nong, H. N.; Gan, L.; Willinger, E.; Teschner, D.; Strasser, P. *Chem. Sci.* **2014**, *5*, 2955.
- (50) Nong, H. N.; Oh, H. S.; Reier, T.; Willinger, E.; Willinger, M. G.; Petkov, V.; Teschner, D.; Strasser, P. *Angew. Chem. Int. Ed.* **2015**, *54*, 2975.
- (51) *CRC Handbook of chemistry and physics*; 90th ed.; CRC Press/Taylor and Francis: Boca Raton, FL, 2010.
- (52) Ramette, R. W. *J. Chem. Educ.* **1987**, *64*, 885.
- (53) Zeng, K.; Zhang, D. K. *Prog. Energy Combust. Sci.* **2010**, *36*, 307.
- (54) Diaz-Morales, O.; Calle-Vallejo, F.; de Munck, C.; Koper, M. T. M. *Chem. Sci.* **2013**, *4*, 2334.
- (55) Yeo, B. S.; Klaus, S. L.; Ross, P. N.; Mathies, R. A.; Bell, A. T. *Chemphyschem* **2010**, *11*, 1854.
- (56) Bockris, J. O. *J. Chem. Phys.* **1956**, *24*, 817.
- (57) Rossmeisl, J.; Qu, Z. W.; Zhu, H.; Kroes, G. J.; Norskov, J. K. *J. Electroanal. Chem.* **2007**, *607*, 83.
- (58) Man, I. C.; Su, H. Y.; Calle-Vallejo, F.; Hansen, H. A.; Martinez, J. I.; Inoglu, N. G.; Kitchin, J.; Jaramillo, T. F.; Norskov, J. K.; Rossmeisl, J. *ChemCatChem* **2011**, *3*, 1159.
- (59) Scheuermann, A. G.; Prange, J. D.; Gunji, M.; Chidsey, C. E. D.; McIntyre, P. C. *Energy Environ. Sci.* **2013**, *6*, 2487.
- (60) Casalongue, H. G. S.; Ng, M. L.; Kaya, S.; Friebel, D.; Ogasawara, H.; Nilsson, A. *Angew. Chem. Int. Ed.* **2014**, *53*, 7169.
- (61) Fierro, S.; Nagel, T.; Baltruschat, H.; Comninellis, C. *Electrochem. Commun.* **2007**, *9*, 1969.
- (62) Macounova, K.; Makarova, M.; Krtíl, P. *Electrochem. Commun.* **2009**, *11*, 1865.
- (63) Hamann, C. H.; Hamnett, A.; Vielstich, W. *Electrochemistry*; WILEY-VCH: Weinheim, 2007; Vol. 2.
- (64) Alvarez, L. W.; Alvarez, W.; Asaro, F.; Michel, H. V. *Science* **1980**, *208*, 1095.
- (65) Anema, J. R.; Li, J. F.; Yang, Z. L.; Ren, B.; Tian, Z. Q. *Annu. Rev. Anal. Chem.* **2011**, *4*, 129.
- (66) Denkov, N. D.; Velev, O. D.; Kralchevsky, P. A.; Ivanov, I. B.; Yoshimura, H.; Nagayama, K. *Langmuir* **1992**, *8*, 3183.
- (67) Scofield, J. H. *J. Electron. Spectrosc. Relat. Phenom.* **1976**, *8*, 129.

- (68) Tanuma, S.; Powell, C. J.; Penn, D. R. *Surf. Interface Anal.* **1994**, *21*, 165.
- (69) Knop-Gericke, A.; Kleimenov, E.; Hävecker, M.; Blume, R.; Teschner, D.; Zafeirotos, S.; Schlögl, R.; Bukhtiyarov, V. I.; Kaichev, V. V.; Prosvirin, I. P.; Nizovskii, A. I.; Bluhm, H.; Barinov, A.; Dudin, P.; Kiskinova, M. *Adv. Catal.* **2009**, *52*, 213.
- (70) Hamann, C. H.; Vielstich, W. *Elektrochemie*; WILEY-VCH: Weinheim, 2005; Vol. 4.
- (71) Atkins, P. W. *Physikalische Chemie*; WILEY-VCH: Weinheim, 2004; Vol. 3.
- (72) Ardizzone, S.; Carugati, A.; Trasatti, S. *J. Electroanal. Chem.* **1981**, *126*, 287.
- (73) Grupioni, A. A. F.; Arashiro, E.; Lassali, T. A. F. *Electrochim. Acta* **2002**, *48*, 407.
- (74) da Silva, L. A.; Alves, V. A.; da Silva, M. A. P.; Trasatti, S.; Boodts, J. F. C. *Electrochim. Acta* **1997**, *42*, 271.
- (75) Lodi, G.; de Battisti, A.; Benedetti, A.; Fagherazzi, G.; Kristof, J. *J. Electroanal. Chem.* **1988**, *256*, 441.
- (76) van Hardeveld, R. M.; Gunter, P. L. J.; van Ijzendoorn, L. J.; Wieldraaijer, W.; Kuipers, E. W.; Niemantsverdriet, J. W. *Appl. Surf. Sci.* **1995**, *84*, 339.
- (77) Forgie, R.; Bugosh, G.; Neyerlin, K. C.; Liu, Z.; Strasser, P. *Electrochem. Solid-State Lett.* **2010**, *13*, B36.
- (78) Neyerlin, K. C.; Bugosh, G.; Forgie, R.; Liu, Z.; Strasser, P. *J. Electrochem. Soc.* **2009**, *156*, B363.
- (79) Piccirillo, C.; Daolio, S.; Kristóf, J.; Mihály, J.; Facchin, B.; Fabrizio, M. *Int. J. Mass Spectrom. Ion Processes* **1997**, *161*, 141.
- (80) Hung, L. S.; Gyulai, J.; Mayer, J. W.; Lau, S. S.; Nicolet, M.-A. *J. Apply. Phys.* **1983**, *54*, 5076.
- (81) Liao, P. C.; Chen, C. S.; Ho, W. S.; Huang, Y. S.; Tiong, K. K. *Thin Solid Films* **1997**, *301*, 7.
- (82) Frank, O.; Zukalova, M.; Laskova, B.; Kurti, J.; Koltai, J.; Kavan, L. *Phys. Chem. Chem. Phys.* **2012**, *14*, 14567.
- (83) Balachandran, U.; Eror, N. G. *J. of Solid State Chem.* **1982**, *42*, 276.
- (84) Moser, M.; Mondelli, C.; Amrute, A. P.; Tazawa, A.; Teschner, D.; Schuster, M. E.; Klein-Hoffman, A.; López, N.; Schmidt, T.; Pérez-Ramírez, J. *ACS Catal.* **2013**, *3*, 2813.
- (85) Wertheim, G. K.; Guggenheim, H. J. *Phys. Rev. B: Condens. Matter* **1980**, *22*, 4680.
- (86) Johnson, B.; Girgides, F.; Weinberg, G.; Rosenthal, D.; Knop-Gericke, A.; Schlögl, R.; Reier, T.; Strasser, P. *J. Phys. Chem. C* **2013**, *117*, 25443.
- (87) Ortel, E.; Reier, T.; Strasser, P.; Kraehnert, R. *Chem. Mater.* **2011**, *23*, 3201.
- (88) Murarka, S. P.; Fraser, D. B. *J. Apply. Phys.* **1980**, *51*, 342.
- (89) Reprinted from *Electrochemistry Communications*, Vol. 48, Cherevko, S.; Reier, T.; Zeradjanin, A. R.; Pawolek, Z.; Strasser, P.; Mayrhofer, K. J. J., Stability of nanostructured iridium oxide electrocatalysts during oxygen evolution reaction in acidic environment, 81, Copyright (2014), with permission from Elsevier.
- (90) Katsounaros, I.; Cherevko, S.; Zeradjanin, A. R.; Mayrhofer, K. J. *Angew. Chem. Int. Ed.* **2014**, *53*, 102.
- (91) Cherevko, S.; Topalov, A. A.; Zeradjanin, A. R.; Keeley, G. P.; Mayrhofer, K. J. *J. Electroanalysis* **2014**, *5*, 235.
- (92) Delahaye-Vidal, A.; Beaudoin, B.; Sac-Epée, N.; Tekaia-Elhsissen, K.; Audemer, A.; Figlarz, M. *Solid State Ionics* **1996**, *84*, 239.
- (93) Oliva, P.; Leonardi, J.; Laurent, J. F.; Delmas, C.; Braconnier, J. J.; Figlarz, M.; Fievet, F.; de Guibert, A. *J. Power Sources* **1982**, *8*, 229.
- (94) Suntivich, J.; Hong, W. T.; Lee, Y. L.; Rondinelli, J. M.; Yang, W. L.; Goodenough, J. B.; Dabrowski, B.; Freeland, J. W.; Shao-Horn, Y. *J. Phys. Chem. C* **2014**, *118*, 1856.
- (95) Grosvenor, A. P.; Biesinger, M. C.; Smart, R. S. C.; Stewart McIntyre, N. *Surf. Sci.* **2006**, *600*, 1771.
- (96) Alders, D.; Voogt, F. C.; Hibma, T.; Sawatzky, G. A. *Phys. Rev. B: Condens. Matter* **1996**, *54*, 7716.
- (97) Powell, C. J. *J. Electron. Spectrosc. Relat. Phenom.* **2012**, *185*, 1.
- (98) Mansour, A. N. *Surf. Sci. Spectra* **1994**, *3*, 211.

- (99) Mansour, A. N. *Surf. Sci. Spectra* **1994**, *3*, 231.
- (100) Kahk, J. M.; Poll, C. G.; Oropeza, F. E.; Ablett, J. M.; Céolin, D.; Rueff, J.-P.; Agrestini, S.; Utsumi, Y.; Tsuei, K. D.; Liao, Y. F.; Borgatti, F.; Panaccione, G.; Regoutz, A.; Egdell, R. G.; Morgan, B. J.; Scanlon, D. O.; Payne, D. J. *Phys. Rev. Lett.* **2014**, *112*, 117601.
- (101) Grosvenor, A. P.; Kobe, B. A.; McIntyre, N. S. *Surf. Sci.* **2004**, *572*, 217.
- (102) Reier, T.; Teschner, D.; Lunkenbein, T.; Bergmann, A.; Selve, S.; Kraehnert, R.; Schlögl, R.; Strasser, P. *J. Electrochem. Soc.* **2014**, *161*, F876.
- (103) Reier, T.; Weidinger, I.; Hildebrandt, P.; Kraehnert, R.; Strasser, P. *ECS Trans.* **2013**, *58*, 39.
- (104) Cui, C. H.; Gan, L.; Neumann, M.; Heggen, M.; Cuenya, B. R.; Strasser, P. *J. Am. Chem. Soc.* **2014**, *136*, 4813.
- (105) Le Ru, E. C.; Etchegoin, P. G. *Principles of Surface-Enhanced Raman Spectroscopy*; Elsevier: New York, 2009; Vol. 1.
- (106) Wohlfahrt-Mehrens, M.; Heitbaum, J. *Journal of Electroanalytical Chemistry* **1987**, *237*, 251.
- (107) Zou, S. Z.; Weaver, M. J. *Anal. Chem.* **1998**, *70*, 2387.
- (108) Feng, J.-J.; Gernert, U.; Sezer, M.; Kuhlmann, U.; Murgida, D. H.; David, C.; Richter, M.; Knorr, A.; Hildebrandt, P.; Weidinger, I. M. *Nano Lett.* **2009**, *9*, 298.
- (109) Li, J. F.; Huang, Y. F.; Ding, Y.; Yang, Z. L.; Li, S. B.; Zhou, X. S.; Fan, F. R.; Zhang, W.; Zhou, Z. Y.; Wu, D. Y.; Ren, B.; Wang, Z. L.; Tian, Z. Q. *Nature* **2010**, *464*, 392.
- (110) Guier, A.; Reier, T.; Heidary, N.; Felkel, D.; Johnson, B.; Vainio, U.; Schlaad, H.; Aksu, Y.; Driess, M.; Strasser, P.; Thomas, A.; Polte, J.; Fischert, A. *Chem. Mater.* **2013**, *25*, 4645.
- (111) Mar, S. Y.; Chen, C. S.; Huang, Y. S.; Tiong, K. K. *Appl. Surf. Sci.* **1995**, *90*, 497.
- (112) Zeradjanin, A. R.; Menzel, N.; Strasser, P.; Schuhmann, W. *Chemosuschem* **2012**, *5*, 1897.
- (113) Yamada, H.; Hurst, J. K. *J. Am. Chem. Soc.* **2000**, *122*, 5303.
- (114) Ling, J. S.; Farooq, A.; Karlin, K. D.; Loehr, T. M.; Sandersloehr, J. *Inorg. Chem.* **1992**, *31*, 2552.
- (115) Mattes, R.; Moumen, M.; Pernoll, I. *Z. Naturforsch.* **1975**, *30b*, 210.
- (116) Wang, J. H.; Fan, C. Y.; Sun, Q.; Reuter, K.; Jacobi, K.; Scheffler, M.; Ertl, G. *Angew. Chem. Int. Ed.* **2003**, *42*, 2151.
- (117) Villalba, M. E. C.; Echeverria, G.; Aymonino, P. J.; Varetti, E. L. *J. Chem. Crystallogr.* **2011**, *41*, 508.

11 List of Figures

Figure 1:	<i>Electricity generation in Germany in 2014 itemized by energy carriers (unit: TWh). Data obtained from ¹.</i>	1
Figure 2:	<i>Time dependent electricity generation from wind and solar power in Germany during one week in August 2014. Data obtained from ¹.</i>	2
Figure 3:	<i>Gibbs free energy of each elementary reaction ($\Delta_R G_1^0$, $\Delta_R G_2^0$, $\Delta_R G_3^0$, $\Delta_R G_4^0$) plotted as function of ΔE_O for $E=0$ V and $a_{H^+}=1$ according to ⁵⁷. The Gibbs free energy of the overall reaction (OER) is provided for comparison (divided by the number of electrons transferred per water molecule, $n=2$).</i>	15
Figure 4:	<i>a: Custom made central force sample holder for grinding and polishing of Ti cylinders. b: Sample height adjustment tool for the polishing sample holder. c: Polishing sample holder mounted onto the height adjustment tool.</i>	20
Figure 5:	<i>Spin-coating sample holders. a): Standard spin coating sample holder on which the substrate is placed on top and adhered by applying vacuum from the back. b) and c): Drawing and photograph of the custom-made spin coating sample holder with 1: Ti cylinder, 2: tapered ring, 3: spin coating sample holder, 4: adapter to mount the spin-coating sample holder in the spin coater.</i>	21
Figure 6:	<i>a: Teflon coating ring used for the deposition of Au@SiO_x on Ru oxide films. b: Teflon coating ring positioned on the Ru oxide film coated surface of a Ti cylinder.</i>	24
Figure 7:	<i>Custom-made RDE sample holder and accessories. 1: screw nut, 2: RDE sample holder, 3: tapered Teflon ring, 4: contact pin</i>	29
Figure 8:	<i>Graphical representation of the sequence of electrochemical measurements performed to address the electrocatalytic OER activity and characterize the surface state of the catalysts. The whole sequence will be referred to as OER protocol in the following.</i>	30
Figure 9:	<i>TG-MS measurements of Ru (a) and Ir chloride (b) in synthetic air with a heating rate of 5 K min⁻¹.</i>	37
Figure 10:	<i>TG-MS measurements of Ru (a) and Ir acetate (b) in synthetic air with a heating rate of 5 K min⁻¹.</i>	38
Figure 11:	<i>a) Spin-coating film thickness determined by SEM cross-section microscopy as function of $\omega^{-0.5}$ for two Ir acetate concentrations. b) Ir loading in the spin-coating process determined by ICP-OES as function of $\omega^{-0.5}$ for an Ir acetate concentration of 80 g l⁻¹. A Si wafer or a Ti cylinder (with custom made holder) was used as substrate.</i>	40
Figure 12:	<i>SEM top view (a) and cross-section (b) micrographs of an Ir oxide film deposited on a Si wafer. Spin-coating conditions: $\omega=2000$ rpm, $c_{0,mass}=80$ g l⁻¹ Ir acetate.</i>	42
Figure 13:	<i>EDX line scan of an Ir acetate film on a Si wafer. The scan was performed from the sample holder towards the coated substrate whereby the boundary was set to zero (data were smoothed). Film deposition conditions: $\omega=2000$ rpm and $c_{0,mass}=80$ g l⁻¹ Ir acetate.</i>	43
Figure 14:	<i>EDX line scan for Ir acetate films on Ti cylinders. The standard spin-coating holder was used for a) while a custom made holder was used for b). The scans were performed from the sample holder towards the coated substrate whereby the</i>	

	<i>boundary was set to zero (data were smoothed). Spin-coating conditions: $\omega=2000$ rpm and $c_{0, mass}=80$ g L⁻¹ Ir acetate.</i>	44
Figure 15:	<i>Graphical representation of the different substrates applied for the study of Ir oxide films (IrOF, shown as black layer) (a: Ti cylinder, b: Si wafer, c: Ti coated Si wafer (TS)). The experimental techniques for which the respective substrate was applied are listed below the substrates.</i>	48
Figure 16:	<i>SEM images of Ir oxide films (IrOF) calcined at different temperatures. a-d: Topview images of IrOF coated Ti cylinders calcined at temperatures between 250°C and 550°C. e-h: Cross section images of IrOFs deposited on TS calcined at temperatures between 250°C and 550°C.</i>	49
Figure 17:	<i>TEM/STEM cross section investigation of the Ir oxide film on a TS wafer calcined at 550°C. a: TEM image (herein the 4 layers on top of the TS are labeled as L1-L4), b: corresponding STEM image, c-e: EDX elemental mapping over the layered system for Ir, Ti and Si, f: STEM image of the topmost layer (L4) and g: high resolution STEM image of L4.</i>	50
Figure 18:	<i>EDX spectrum of IrOF(550°C) on a Ti cylinder (a) and EDX results for all calcination temperatures (measured with 10 kV, substrate: Ti cylinder), including the as deposited uncalcined Ir acetate film (shown at 25°C) (b).</i>	51
Figure 19:	<i>XRD patterns of IrOFs on Ti cylinders (a) and with linear background correction from 24° to 32° 2 Θ (b) to magnify the (110) reflection of the rutile type oxides. Reference patterns from the powder diffraction file (PDF) are provided for comparison (reference number given in parentheses).</i>	52
Figure 20 :	<i>Grazing incidence X-ray diffraction measurement of IrOF(550°C) on a Ti cylinder together with results from Rietveld refinement. a) Measured and calculated diffraction pattern, b) contribution of the individual phases used within the refinement and c) difference between measured and calculated diffraction pattern.</i>	53
Figure 21:	<i>Raman spectra of IrOFs on Ti cylinders calcined at different temperatures together with reference Raman shifts for IrO₂⁸¹ and TiO₂⁸².</i>	54
Figure 22:	<i>Graphical representation of the E_g, B_{2g} and A_{1g} lattice vibrations in the rutile-type structure according to⁸² together with the vibration frequencies from⁸¹.</i>	55
Figure 23:	<i>XPS measurements of IrOFs on TS, (a) Ir 4f region, (b) valence band, (c) O 1s and (d) Ti 2p region. The applied photon energies were as follows. Ir4f and VB 599 eV, O1s 1080 eV and Ti2p 1010 eV.</i>	57
Figure 24:	<i>Anodic charge q* obtained by integration of anodic currents of a CV measured between 0.4 and 1.4 V (50 mV s⁻¹) for IrOFs on Ti cylinders (a). Cyclic voltammetry measured between 0.05 and 1.4 V with 50 mV s⁻¹ at room temperature in 0.1 M HClO₄ for Ir oxide films on Ti cylinders (b).</i>	58
Figure 25:	<i>Temperature programmed reduction measured with 10 K min⁻¹. Ir oxide films on silicon wafers (a) and Ir oxide films on TS (b). The detector signal is normalized to the applied geometric film area.</i>	60
Figure 26:	<i>Quasi stationary OER polarization curves for IrOFs on Ti recorded at the outset of the electrocatalytic measurements (OER scan 1) before the CVs were recorded and thereafter (OER scan 2).</i>	62
Figure 27:	<i>Quasi-stationary OER polarization curves for IrOFs on Ti (OER scan 1). Tafel plot (a) and potential at a current density of 0.5 mA cm⁻² or, respectively, 0.5 mA mC⁻¹ as measure for the OER activity (b).</i>	63

Figure 28:	<i>Potential resolved dissolution measurements of Ir (1, upper row) and Ti (2, lower row) measured for IrOFs (550°C-250°C, a-d) and metallic Ir (e). Reproduced with permission of Elsevier.</i> ⁸⁹	65
Figure 29:	<i>Integral amount of Ir and Ti dissolved during the potential resolved measurement provided in Figure 28. Ir dissolution is splitted into cathodic (low potential) and anodic (high potential) dissolution.</i>	67
Figure 30:	<i>Potential resolved online ICP-MS Ir and Ti dissolution measurements during chrono-potentiometric OER at 1 and 2 mA cm⁻². Current density and electrode potential as function of time are shown in a and c, respectively. Ir and Ti dissolution rates are depicted in b and d, respectively. Reproduced with permission of Elsevier.</i> ⁸⁹	68
Figure 31:	<i>Integral amount of Ir and Ti dissolved during the second chrono-potentiometric step (2 mA cm⁻²) depicted in Figure 30.</i>	69
Figure 32:	<i>Electrocatalytic measurements of OER activity and stability of Ir-Ni mixed oxide films with different Ir to Ni ratios, here referred to as x%Ni-MO (x atomic % Ni). a) Quasi stationary OER polarization curves (iR corrected). b) Current densities at an OER overpotential of 300 mV (1.530 V vs. RHE) normalized to the electrodes geometric surface area (j_{geo}), the anodic charge q^* (j_{spec}) and the applied Ir mass (j_{mass}). c) Anodic charge q^* measured by CV between 0.4 and 1.4 V with 50 mV s⁻¹. d) Amount of dissolved Ir during 30 min of OER with 1 mA cm⁻². The amount of dissolved Ir is provided normalized to the geometric surface area and to q^*.</i>	74
Figure 33:	<i>Topview SEM images of Ir-Ni mixed oxide films on Ti substrates with different initial Ni contents acquired on as prepared samples (MO-ap, upper row, a1-g1) and samples that underwent the OER protocol (MO-OER, bottom row, a2-g2).</i>	75
Figure 34:	<i>a) Near surface and bulk composition of Ir-Ni mixed oxides films before (MO-ap) and after (MO-OER) the electrocatalytic OER protocol. The Ni content measured by ICP-OES is provided on the x-axis. The near surface Ni content and the bulk Ni content shown on the y-axis were determined by XPS or, respectively, by averaging XPS depth profiles. b) Amount of dissolved Ni during 30 min of OER at 1 mA cm⁻² measured by potential resolved ICP-MS with MO-OER films. c) Integrated and base line corrected selected area electron diffraction measurements of MO-ap transformed into the 2θ scale (Cu K-α). Reference patterns from the powder diffraction file are provided for comparison. d) Structural model according to c). I) depicts the rutile type (IrO₂) and III) the bunsenite type (NiO) unit cell. II) depicts a structural model for 39%Ni-MO-ap. (O or OH: red, Ni: yellow, Ir: blue).</i>	77
Figure 35:	<i>XPS sputter depth profile measurements of MO-ap (a) and MO-OER (b).</i>	78
Figure 36:	<i>Quasi steady-state OER polarization curves (OER scan 2) of 67% Ni-MO with and without (standard protocol) electrolyte exchange. In case of the exchange measurement, the electrolyte was exchanged two times, once before and once after CV.</i>	79
Figure 37:	<i>O K-edge absorption spectra of Ir-Ni mixed oxide films in the a) as-prepared state (MO-ap), and b) after the OER catalysis (MO-OER).</i>	81
Figure 38:	<i>X-ray photoelectron spectra provided together with reference binding energies. Ni 2p region measured on as prepared (MO-ap, a) and electrochemically treated (MO-OER, c) Ir-Ni oxide films. Ir 4f and Ni 3p region measured on as prepared (MO-ap, b) and electrochemically treated (MO-OER, d) films. Reference binding energies: Ir⁹⁷, IrO₂⁸⁴, Ni⁹⁸ and NiO⁹⁹.</i>	82
Figure 39:	<i>X-ray photoelectron spectra of the O 1s region of MO-ap and MO-OER provided together with reference binding energies from</i> ¹⁰²	84

Figure 40:	<i>a) Hydroxyl group (OH) fraction to the total oxide related oxygen (hydroxyl groups and both lattice oxygen species) as determined by XPS. b) Cyclic voltammetry measured with 50 mV s⁻¹. The current was normalized to q* (reflecting the electrochemical active oxide surface area) c) Potential of the anodic peak observed in b). d) Model of Ni leaching from the surface of Ir-Ni mixed oxides.</i>	85
Figure 41:	<i>a) Electrochemical Ir oxide formation on a polished metallic Ir electrode by cyclic voltammetry (500 mV s⁻¹, 0.1 M HClO₄ (N₂ degassed), 0 rpm, room temperature) performed as an additional first step prior to the OER protocol. b) Cyclic voltammetry of the electrochemically formed Ir oxide and 79%Ni-MO measured within the OER protocol after OER Scan 1 with 50 mV s⁻¹ in 0.1 M HClO₄.</i>	90
Figure 42:	<i>Geometric OER current density obtained at 300 mV overpotential (1.530 V_{RHE}) from OER scan 2 for Ir oxide films calcined at different T, Ir-Ni mixed oxides and electrochemically oxidized Ir.</i>	91
Figure 43:	<i>Ir Mass based (a) and surface specific (b, based on q*) OER current densities obtained at 300 mV overpotential (1.530 V_{RHE}) from OER scan 2 for Ir oxide films calcined at different T, Ir-Ni mixed oxides and electrochemically oxidized Ir.</i>	92
Figure 44:	<i>Ir amount dissolved during 10 min OER at 1 mA cm⁻² measured by PR-ICP-MS normalized to the investigated geometric surface area (a) or, respectively, q* representing the electrochemically active surface area of Ir oxide (b). The measurements were performed for Ir oxide films calcined at different T, Ir-Ni mixed oxides and a metallic Ir electrode.</i>	93
Figure 45:	<i>Grazing incidence X-ray diffraction measurement of a RuO₂ thin-film catalyst on a Ti cylinder together with results from Rietveld refinement. a) Measured and calculated diffraction pattern, b) separate contribution of components used within the refinement and c) difference between measured and calculated diffraction pattern.</i>	97
Figure 46:	<i>Scanning electron micrographs of a RuO₂ thin-film. Figure a) and b) show top-view images with different magnifications (substrate: Ti cylinder) and Figure c) shows a cross-section micrograph (substrate: Si wafer).</i>	98
Figure 47:	<i>Average silica shell thickness and related standard deviation of Au@SiO_x nanoparticles obtained for different reaction times at 90°C as measured by TEM.</i>	99
Figure 48:	<i>Cyclic voltammetry of pristine and silica coated (30 min reaction time) gold NPs measured with 50 mV s⁻¹ in 0.05 H₂SO₄. The current was normalized according to the applied gold mass.</i>	100
Figure 49:	<i>TEM micrograph of a silica coated gold (Au@SiO_x) nanoparticle (a). SEM micrographs of Au@SiO_x NPs applied on top of the RuO₂ film with higher (b) and lower magnification at two different positions on the sample (c and d). SEM images were acquired with an acceleration voltage of 4 kV.</i>	101
Figure 50:	<i>Cyclic voltammetry of the RuO₂ catalyst film measured with and without Au@SiO_x NP coating between 0.4 V and 1.4 V (a) or 1.5 V (b), respectively. The measurements were performed in 0.1 M HClO₄ with 50 mV s⁻¹.</i>	102
Figure 51:	<i>Schematic representation of the spectro-electrochemical cell. 1: Pt mesh counter electrode, 2: porous glass drip, 3: immersion objective, 4: transparent polymer foil, 5: Ag/AgCl reference electrode, 6: cell body, 7: sample</i>	103
Figure 52:	<i>SHINER spectra acquired at electrode potentials of (a) 0.4, (b) 1.2, (c) 1.4, and (d) 1.5 V_{RHE}. The SHINER measurements were performed in 0.1 M HCl¹⁶O₄/H₂¹⁶O (black), DCl¹⁶O₄/D₂¹⁶O (red) and HCl¹⁶O₄/H₂¹⁸O (blue) electrolyte of 0.1 M concentration, respectively.</i>	104

Figure 53:	<i>a) in-situ Raman spectra of a RuO₂ catalyst without Au@SiO_x NP at different potentials measured in 0.1 M HCl¹⁶O₄/H₂¹⁶O. b) and c) Illustration of the E_g and A_{1g} lattice vibration of RuO₂ according to reference⁸² together with vibration frequencies measured for a RuO₂ single crystal¹¹¹</i>	105
Figure 54:	in-situ SHINER spectra of a) polished Ti and b) TiO _x (polished and thermally treated equivalent to RuO ₂ catalyst) reference samples covered with Au@SiO _x NPs at different potentials measured in 0.1 M HCl ¹⁶ O ₄ /H ₂ ¹⁶ O.	106
Figure 55:	in-situ SHINER spectra of the RuO ₂ catalyst covered with Au@SiO _x NPs at higher Raman shifts measured in 0.1 M HCl ¹⁶ O ₄ /H ₂ ¹⁶ O at different potential (vs. RHE).....	107
Figure 56:	<i>Grazing incidence X-ray diffraction measurement of IrOF(450°C) on a Ti cylinder together with results from Rietveld refinement. a) Measured and calculated diffraction pattern, b) contribution of the individual phases used within the refinement and c) difference between measured and calculated diffraction pattern.</i>	116
Figure 57:	Quasi stationary polarization curves for pure Ir and pure Ni oxide films (iR corrected).....	117
Figure 58:	Film thickness of MO-ap as function of the initial Ni content measured by cross section SEM. Silicon wafers were applied as substrates.....	117
Figure 59:	Grazing incidence X-ray diffraction measurements of MO-ap. References patterns from the powder diffraction file are provided for comparison.....	118
Figure 60:	Fitted X-ray photoelectron spectra of the Ir 4f and Ni 3p region of MO-ap.....	119
Figure 61:	Fitted X-ray photoelectron (XP) spectra of the Ir 4f and Ni 3p region of MO-OER.	120
Figure 62:	Fitted X-ray photoelectron spectra of the O 1s region of MO-ap.....	121
Figure 63:	Fitted X-ray photoelectron spectra of the O 1s region of MO-OER.....	122

12 List of Tables

Table 1: <i>Diffusion coefficients^{51,71} (D), Nernst Diffusion layer thicknesses (δ, according to equation (21)) and bulk-surface concentration differences (Δc, according to equation (22)) calculated for H^+ and O_2 at 25°C. The calculation was performed for a current density of 15 mA cm⁻² and a RDE rotational velocity of 1600 rpm.</i>	35
Table 2: Rietveld refinement results for IrOF(550°C)/Ti cylinder (GOF: 2.81)	115
Table 3 : Rietveld refinement results for IrOF(450°C)/Ti cylinder (GOF: 2.15)	115
Table 4: Rietveld refinement results for the RuO ₂ thin-film on a Ti cylinder (GOF: 2.67).....	115

13 List of Publications

The following list contains the articles that have been published during the time of the doctoral studies.

1. Reier, T.; Oezaslan, M.; Strasser, P., "Electrocatalytic Oxygen Evolution Reaction (OER) on Ru, Ir, and Pt Catalysts: A Comparative Study of Nanoparticles and Bulk Materials", *ACS Catal.* **2012**, *2*, 1765.
2. Reier, T.; Weidinger, I.; Hildebrandt, P.; Kraehnert, R.; Strasser, S., "Electrocatalytic Oxygen Evolution Reaction on Iridium Oxide Model Film Catalysts: Influence of Oxide Type and Catalyst Substrate Interactions", *ECS Trans.*, **2013**, *58*, 39
3. Guet, A.; Reier, T.; Heidary, N.; Felkel, D.; Johnson, B.; Vainio, U.; Schlaad, H.; Aksu, Y.; Driess, M.; Strasser, P.; Thomas, A.; Polte, J.; Fischert, A., "A One-Pot Approach to Mesoporous Metal Oxide Ultrathin Film Electrodes Bearing One Metal Nanoparticle per Pore with Enhanced Electrocatalytic Properties", *Chem. Mater.* **2013**, *25*, 4645.
4. Johnson, B.*; Girgsdies, F.; Weinberg, G.; Rosenthal, D.; Knop-Gericke, A.; Schlogl, R.; Reier, T.*; Strasser, P., "Suitability of Simplified (Ir,Ti)O-x Films for Characterization during Electrocatalytic Oxygen Evolution Reaction", *J. Phys. Chem. C* **2013**, *117*, 25443.
5. Reier, T.; Teschner, D.; Lunkenbein, T.; Bergmann, A.; Selve, S.; Kraehnert, R.; Schlogl, R.; Strasser, P., "Electrocatalytic Oxygen Evolution on Iridium Oxide: Uncovering Catalyst-Substrate Interactions and Active Iridium Oxide Species", *J. Electrochem. Soc.* **2014**, *161*, F876.
6. Cherevko, S.*; Reier, T.*; Zeradjanin, A. R.; Pawolek, Z.; Strasser, P.; Mayrhofer, K. J. J., "Stability of nanostructured iridium oxide electrocatalysts during oxygen evolution reaction in acidic environment", *Electrochem. Commun.* **2014**, *48*, 81.
7. Nong, H. N.; Oh, H. S.; Reier, T.; Willinger, E.; Willinger, M. G.; Petkov, V.; Teschner, D.; Strasser, P., "Oxide-Supported IrNiOx Core-Shell Particles as Efficient, Cost-Effective, and Stable Catalysts for Electrochemical Water Splitting", *Angew. Chem. Int. Edit.* **2015**, *54*, 2975.
8. Oh, H. S.; Nong, H. N.; Reier, T.; Gliech, M.; Strasser, P., "Oxide-supported Ir nanodendrites with high activity and durability for the oxygen evolution reaction in acid PEM water electrolyzers", *Chem. Sci.* **2015**, *6*, 3321.

9. Bernicke, M.; Ortel, E.; Reier, T.; Bergmann, A.; de Araujo, J. F.; Strasser, P.; Kraehnert, R., "Iridium Oxide Coatings with Templated Porosity as Highly Active Oxygen Evolution Catalysts: Structure-Activity Relationships", *ChemSusChem* **2015**, *8*, 1908.
10. Guet, A.; Göbel, C.; Klingan, K.; Lublow, M.; Reier, T.; Vainio, U.; Kraehnert, R.; Schlaad, H.; Strasser, S.; Zaharieva, I.; Dau, H.; Driess, M.; Polte, J.; and Fischer, A., "Hydrophobic Nanoreactor Soft-Templating: A Supramolecular Approach to Yolk@Shell Materials", *Adv. Funct. Mater.*, **2015**, DOI: 10.1002/adfm.201502388
11. Varela, A. S.; Kroschel, M.; Reier, T.; Strasser, P., "Controlling the selectivity of CO₂ electroreduction on copper: The effect of the electrolyte concentration and the importance of the local pH", *Catal. Today*, **2015**, DOI: 10.1016/j.cattod.2015.06.009
12. Reier, T.; Pawolek, Z.; Cherevko, S.; Bruns, M.; Jones, T.; Teschner, D.; Selve, S.; Bergmann, A.; Nong, H. N.; Schlögl, R.; Mayrhofer, K. J. J.; Strasser, P., "Molecular insight in structure and activity of highly efficient, low-Ir Ir-Ni oxide catalysts for electrochemical water splitting (OER)", *J. Am. Chem. Soc.*, **2015**, DOI: 10.1021/jacs.5b07788

*equal contribution

14 List of Abbreviations

Au@SiO _x	Silica coated gold nanoparticles
AuNP	gold nanoparticles
EAL	effective attenuation lengths
EDX	Energy dispersive X-ray
Hupd	hydrogen underpotential deposition
ICP-OES	by inductively coupled plasma atomic emission spectroscopy
MO	Ir-Ni mixed oxide
MO-ap	as prepared Ir-Ni mixed oxide
MO-OER	Ir-Ni mixed oxide that underwent the OER protocol
OCP	open circuit potential
OER	Oxygen Evolution Reaction
PDF	powder diffraction file
PEEK	polyether ether ketone
POM	polyoxymethylene
PR-ICP-MS	Potential resolved inductively coupled plasma mass spectrometry
RDE	rotating disk electrode
rpm	revolutions per minute
SAED	Selected area electron diffraction
SEM	Scanning electron microscopy
SFC	scanning flow cell
SPCE	screen printed carbon electrode
STEM	Scanning transmission electron microscopy
STP	Standard temperature and pressure
TEM	Transmission electron microscopy
TPR	Temperature programmed reduction
x%Ni-MO	Ir-Ni mixed oxide with x at% Ir substituted by Ni
XAS	X-ray absorption spectroscopy
XRD	X-ray diffraction